Faculté des Sciences

Groupe de Recherche en Energie et Environnement par les MATériaux-Laboratoire de Chimie Inorganique Structurale (GREEnMat – LCIS)

Université de Liège

Influence of porosity on the electrochromic properties of tungsten oxide films

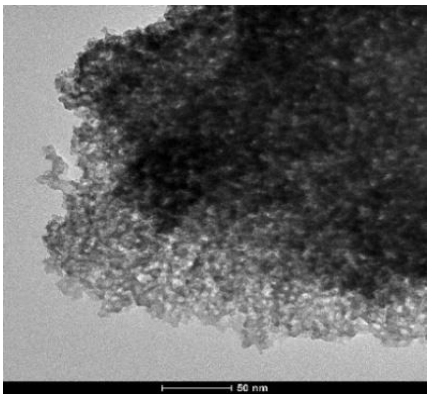

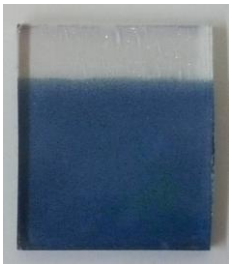

Dissertation presented by
Dafni Chatzikyriakou
to obtain the title of
Doctor of Sciences
2015-2016

Table of Contents

Summary/Sommaire

The objective of this PhD was to synthesize mesoporous tungsten oxide thin films via the soft-templating technique and investigate the impact of porosity on their electrochemical/optical properties.

Electrochromic films have intrigued many researchers in the last years for their ability to reversibly modulate the visible/NIR light when a small voltage is applied. This property can contribute in energy efficient applications like smart windows. For this purpose, the electrochromic films should exhibit high optical contrast (ΔT%), high coloration efficiency (η, cm^2/C), full reversibility and long-term stability. Moreover they should present fast switching kinetics compatible with the human's eye capability to adjust to an optical change.

One way to optimize these properties is to increase the surface area of the electrochromic layers by introducing porosity in their bulk. It is already documented in the literature that the presence of porosity in a system can potentially enhance its electrochemical properties by facilitating the transfer of cations in the interior of the host, enabling higher flux and shorter diffusion paths for the cations by allowing the penetration of the electrolyte inside the film.

In our studies we prepared mesoporous films with three different processing routes: dip-coating, electrodeposition and ultrasonic spray pyrolysis.

The dip-coating technique is typically utilized for the formation of mesostructured films as it is efficiently combined with the EISA (Evaporation Induced Self Assembly) method. The synthesis of well-organized mesostructures allowed us to investigate the electrochemical properties of tungsten oxide films with and without porosity. Based on our studies, we explored the impact of atmospheric water and the abundance of hydroxyls and water molecules in porous films on the electrochromic reaction. The dip-coated films were also studied by Raman spectroscopy before and after Li^+ intercalation and de-intercalation. Even though porous films exhibit a more active surface for lithium intercalation compared to their dense counterparts their hydrated and more active surface renders them more prone to network disruption and degradation with cycling. On the other hand, dense films exhibit inferior lithium capacity and they irreversibly trap cations in the first cycles which gives them a permanent blue color even after the electrochemical measurement.

Next, we studied the possibility of synthesizing mesoporous films with electrodeposition. Two different surfactants have been used in order to prepare electrodeposited mesoporous tungsten oxide films, a non-ionic surfactant (Brij-56 or Brij-C10) and an anionic polymer (Poly(sodium 4-styrene sulfonate)). The synthesis of mesoporous films via this method appeared to be a challenging task since only random evidences of templating have been collected. Low coverage, no strong evidences of porosity, lack of reproducibility and low electrochemical properties are some of the problems encountered in electrodeposition experiments.

The last part of this thesis was constituted by the preparation of surfactant-assisted porous films with a less conventional pores-generating method, the ultrasonic spray pyrolysis. The interest in the spraying methods is progressively expanding in an industrial level in the last years, due to their cost-effectiveness, their fast and continuous production rates, without requiring vacuum conditions. Therefore, the goal in this last part was to combine the advantages of porous films with the unquestionable privileges that this processing method has to offer. Structural and microstructural characteristics, crystallinity, porosity, thickness, the amount of deposited material and electrochemical/electrochromic properties were investigated in a certain deposition temperature range. Once more all the above characteristics were compared to the surfactant-free films. In this case, the presence of surfactant not only affects the electrochromic properties of the films but it tremendously improves solution wettability in the investigating temperature and reduces droplets size which eventually determines film deposition.

L'objectif de cette thèse était de synthétiser des films minces mésoporeux d'oxyde de tungstène par la technique ‘’templating’’ et d'examiner l'effet de la porosité sur leurs propriétés optiques et électrochimiques.

Au cours des dernières années, films électrochromes est un sujet qui intrigue de nombreux chercheurs pour leur capacité à moduler de façon réversible la lumière visible / NIR quand un petit potentiel électrique est appliqué. Cette propriété peut contribuer à la réduction de la consommation énergétique, avec de nouvelles applications comme les fenêtres intelligentes. A cet effet, les films électrochromes doivent présenter de contraste optique élevé (ΔT%), de l’efficacité de coloration élevé (η, cm^2 /C), une réversibilité complète et une stabilité de long durée. En outre, ils doivent présenter des cinétiques rapides, compatibles avec la capacité de l'œil humain de s'ajuster à la lumière.

Une façon d'optimiser ces propriétés consiste à augmenter la surface spécifique des couches électrochromes en introduisant dans leur porosité apparente. Il est déjà documenté dans la littérature que la présence de porosité dans un système peut potentiellement améliorer ses propriétés électrochimiques, en facilitant le transfert de cations à l'intérieur de l'hôte inorganique, permettant à flux élevé et plus courts chemins de diffusion des cations, en permettant la pénétration de l’électrolyte à l'intérieur du film.

Dans nos études, nous avons préparé des films mésoporeux avec trois voies de traitement différents : dip-coating, électrodéposition et spray pyrolyse ultrasonique (USP).

La technique dip-coating est typiquement utilisé pour la formation de films mésostructurés comme il est efficacement combinée avec la méthode EISA (Evaporation Induced Self Assembly). La synthèse de mésostructures bien organisés nous a permis d'étudier les propriétés électrochimiques des films d'oxyde de tungstène avec et sans porosité. Sur la base de nos études, nous avons exploré l'impact de l'eau atmosphérique et l'abondance des groupes hydroxyle des molécules d'eau dans des films poreux sur la réaction électrochimique. Les films ont également été étudiés par spectroscopie Raman avant et après l’intercalation et la de-intercalation des cations Li^+. Même si des films poreux présentent une surface plus actif de l'intercalation du lithium par rapport à leurs homologues denses leur surface hydratée les rend plus sensitifs à la dégradation. D'autre part, les films denses présentent une capacité inférieure et ils intercalent cations irréversiblement dans les premiers cycles qui leur donne une couleur bleue permanente, même après la mesure électrochimique.

Ensuite, nous avons étudié la possibilité de synthétiser films mésoporeux avec électrodéposition. Deux surfactants différents ont été utilisés pour préparer des films mésoporeux d'oxyde de tungstène, un agent non-ionique (Brij-56 ou Brij-C10) et un polymère anionique (poly (sodium 4-styrène sulfonate)). La synthèse de films mésoporeux via cette méthode etait une tâche difficile étant donné que seules preuves de l’obtention du mécanisme ‘’templating’’. Faible taux de couverture, pas de solides preuves de porosité, manque de reproductibilité et de faibles propriétés électrochimiques sont quelques-uns des problèmes rencontrés dans les expériences d'électrodéposition.

La dernière partie de cette thèse a été constitué par la préparation de films poreux avec une méthode de génération de pores moins conventionnelle, la spray pyrolyse ultrasonique (USP). L'intérêt pour les méthodes de pulvérisation étend progressivement au niveau industriel dans les dernières années, en raison de leur rapport rentabilité, leur taux de production rapides et continues, sans nécessiter des conditions de vide. Par conséquent, l'objectif de cette dernière partie était de combiner les avantages des films poreux avec les privilèges incontestables que cette méthode de traitement a à offrir. Caractéristiques structurelles et des microstructures, cristallinité, la porosité, l'épaisseur, la quantité de matière déposée et propriétés électrochimiques / électrochrome ont été étudiés dans une certaine gamme de température de dépôt. Une fois de plus l'ensemble des caractéristiques ci-dessus ont été comparés à des films sans tensioactif. Dans ce cas, la présence de l'agent tensioactif non seulement affecte les propriétés électrochromes des films mais il améliore énormément la mouillabilité de la solution, la température dépôt et réduit la taille des gouttelettes qui détermine finalement le dépôt du film.

Acknowledgements

These following lines are dedicated to all the people who have supported me through these four years of my PhD, either with their scientific guidance or with their friendship and kindness.

First of all, I would like to thank my supervisor Dr. Catherine Henrist and my co-supervisor prof. Rudi Cloots for giving me the opportunity to pursue my studies in the LCIS-GreenMat laboratory. Throughout these years, Dr. Henrist has encouraged me, trusted my work and always advised me to have more self-confidence and believe in myself. For this I am truly grateful. She was also persistently encouraging me to learn French for my own benefit, however I failed to meet her expectations (still infant level after 5 years of living in Belgium).

I wish to express my gratitude to each member of the examining committee for devoting their time to read this dissertation.

During the whole period of my studies, prof. Bernard Gilbert from the laboratory of Analytical Chemistry welcomed me in his laboratory, gave me access to the UV-Vis and IR devices and he spent valuable time to optimize the Raman conditions for my films. Moreover, he was always pleased to answer my questions and willing to help with any rising difficulty. For his valuable support all these years, I am truly thankful. I would also like to express my deep gratitude to Natacha Krins, a joyful person with great kindness, scientific knowledge and expertise. I wish her good luck and prosperity in every part of her life.

Many thanks to my colleague Jennifer Dewalque for her guidance and for sharing her knowledge and expertise with me. My short interaction with her made me realize that she is a creative scientist with enthusiasm for research and a valuable member of the LCIS-GreenMat laboratory. I would also like to acknowledge Pierre Colson for his guidance in a scientific and administrative level. Special thanks to Anthony Maho a colleague who has been supportive and kind to me since the first moment of his arrival in the laboratory. His pleasant personality, his motivating words and his guidance this last year have helped me in a scientific and personal level. Many thanks to Magali Brisbois and Sebastien Caes for their help, their support and for sharing technical and scientific knowledge with me. I am especially grateful to Gilles Spronck for all the time he spent to explain me the technical information I needed to conduct my experiments. He was always there to fix the technical

problems which occasionally appeared and for which very often I was the cause. His patience and pleasant character were many times a touch of relief in hard to cope days.

I am also grateful to the “Alexander S. Onassis” public benefit foundation (2011-2012) and the “Service des bourses d’excellence Wallonie-Bruxelles International” (2012-today) for their financial support all these years.

The transition from my home country Cyprus to Belgium was not an easy venture for me. Luckily, many new friends made this period more joyful and helped me realize that difficulties can be surpassed with nice people and true friends surround you. Many thanks to Davide Fabozzi, Gustavo Valverde and Rebeca Mora for the great moments we spent together and their invaluable friendship. These joyful last two years would not have been the same without Lampros Papangelis, Eleftheria Sitara and Theodoris Kyriakides. Many thanks to Frederic Plumier for his support and for considering my husband and me as a family for him and his son Antoine. I would also like to thank Catherine Brasseur for all her support. With our cheerful discussions during lunchtimes she brightened my days at the university and she has proven to be an invaluable friend.

The words are short to describe how grateful I am to my husband Petros for his patience and his unconditional love all these years. Many thanks to my sister Milto for her support and for bringing to life my beautiful niece Evelina, and to my younger sister Achillina who supported me when I needed her the most. Last but not least, I would like to express my gratitude to the pillars of my life, my parents Giorgos and Demetra who all these years created a warm, safe and happy environment for me so I can freely pursue my goals.

Chapter 1
Introduction

1.1 Electrochromism

The electrochromic materials can change their optical properties (e.g. from a transparent to a dark, tinted state and vice versa) by the application of a small reversible dc voltage (Figure 1.1) [1]. This property stems from the electrochemical double insertion and extraction of ions and electrons in the host lattice [1, 2].

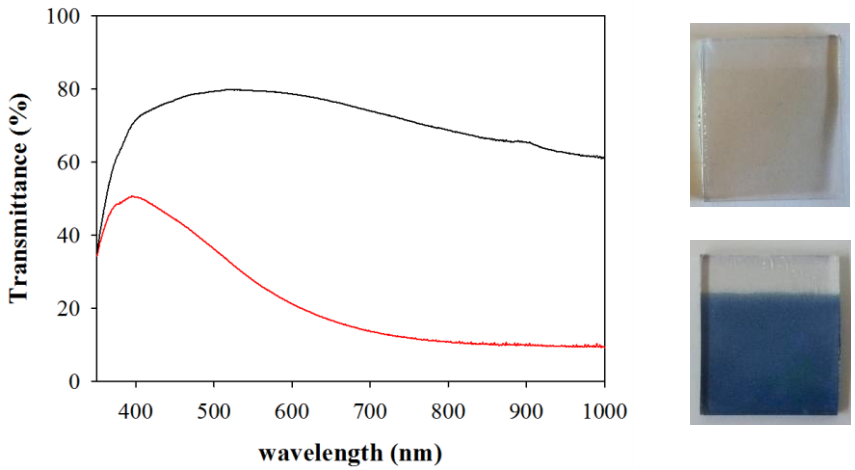

Figure 1.1: UV-Vis spectra depicting the transmittance state of a bleached (black line) and a colored (red line) WO_3 film

Electrochromism finds applications in anti-glare automobile rearview mirrors, sunroofs, opto-electronic shutters, hydrogen sensors, displays and energy efficient "smart" windows [1, 3]. A lot of attention has been devoted in the latter application due to the potential for significant energy savings by reducing cooling and heating loads and a better management of the natural light and glare in buildings [2, 4-6]. This impact stems from the ability of these materials to absorb or reflect the visible and near-infrared solar irradiation according to the occupant's needs [3]. Subsequently, a control over the daylight and solar heat gain from windows can be achieved with the application of small applied voltages [5].

In industrial applications, the electrochromic device is comparable to a thin-film electrical ‘’battery-type’’ design and characterized by superimposed layers positioned between two substrates (Figure 1.2) [3]. Glass is usually used as a substrate especially for building related applications but polymers such as polyethylene terephthalate (PET) or polycarbonate (PC) can be used as well [3, 5].

Onto the two substrates, a second layer is deposited which consists of the transparent electron conductive films. Numerous transparent films can serve as electrical conductors such as oxide films (doped In_2O_3, SnO_2, ZnO compounds, where dopants could be Sn, Zn, Nb, Si, B, F, In etc), metal based conductors (such as Cu, Ag, Au) or a combination thereof, carbon-based conductors etc [5, 7].

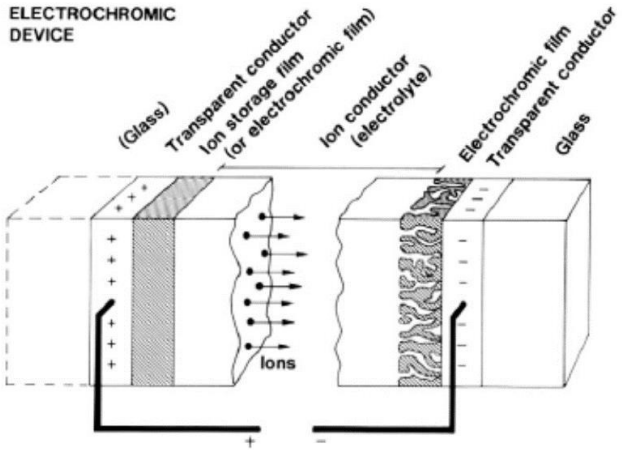

Figure 1.2 [3]: The five- layers electrochromic device

The electrochromic layers which are deposited on the electron conductive films are divided into cathodic and anodic. The former are the main electrochromic electrodes which exhibit color upon electron and cation injection while the latter behave complementary and color upon their removal. In an electrochromic device, both types of films can be employed as working and counter electrodes respectively [5]. Many cathodic electrochromic materials have been well documented in the literature, including WO_3, MoO_3, TiO_2, Ta_2O_5, doped or mixed tungsten oxides (where dopant or the other compound is Ti, Li, Mo, ITO, carbon nanotubes etc.), organic polymers (polyaniline PANI, Poly(3,4-ethylene-dioxythiophene PEDOT, viologens) etc. From these compounds, the most efficient and subsequently the most commercially implemented material is tungsten oxide [2, 3, 5]. This material (which will be discussed in more detail in a separate paragraph) combines good electrochromic properties and long-term stability [2]. Among the anodic candidates, nickel oxide is the conventional choice since it exhibits good electrochromic properties and it is less expensive compared to other materials (e.g. IrO_2) [2, 5]. Moreover, it functions well with tungsten oxide giving to the device a more neutral dark state [5]. It was found that doped nickel oxide (where dopant is W, Ta, Al and Mg) could improve the optical response and durability of the material [2, 5].

The ion conductor (electrolyte) in Figure 1.2 which separates the two electrochromic layers serves as a cation source (H^+, Li^+, Na^+, K^+), where cations move from or towards the working electrode depending on the voltage's direction [3, 5]. C. G Granqvist et al. [8] in 1992 published an extensive study on the different types of electrolytes which were reported in electrochromic devices until that moment. The three limitations which should be taken into consideration in the electrolytes choice is 1) the stability of the electrochromic layers which are in contact with the electrolyte 2) the resistance of the latter which might limit the switching kinetics especially in large surfaces and 3) a leakage possibility associated with liquid electrolytes. For this reason different electrolytes have been tested such as H_2SO_4 (durability $<10^4$ cycles, dissolution of tungsten oxide in the acid), $LiClO_4$ in propylene carbonate, solid bulk-type and thin-film ion conductors ($H_3PO_4(WO_3)_{12}.29H_2O$, hydrated Sb oxides, $Na_2O.11Al_2O_3$, MgF_2, Cr_2O_3, LiF, $LiAlF_4$, $LiNbO_3$, Ta oxides and polymer electrolytes). In a more recent publication [3] of 2014, ionic liquids and electrolytes functionalized by nanoparticles (such as ITO) were added in the list of possible device electrolytes. The latter can obtain a near-infrared plasmon-based absorption and diminish the transmittance in that wavelength region. This property can be beneficial in smart windows devices especially for warm climates.

1.1.1 Prerequisites for electrochromic applications

The electrochromic devices should combine a number of properties in order to be considered ideal candidates for commercial smart windows. For example, they should exhibit an open circuit memory and the optical absorption should be tuned and adjusted to any level between states of minimum and maximum absorption according to the occupant's needs [3]. Importantly, the device should be characterized by high optical contrast ($T_{bleached}$-$T_{colored}$ %) and high coloration efficiency (CE) in the desired wavelength range. The latter is determined by:

$$CE\ (\lambda) = \frac{\log[T_{bl}(\lambda)/T_{col}(\lambda)]}{Q}$$

where Q is the electronic charge injected per unit area, T_{bl} is the transmittance in the bleached state and T_{col} is the transmittance in the colored state. Coloration efficiencies as high as 80 $cm^2.C^{-1}$ were reported for amorphous WO_3 [4].

Ideally the selection of the electrochromic materials should be carried out in order to obtain individual control over the visible and near-infrared region and thus an independent control over the visible sunlight and solar heat into a building. This need arises from the fact that the human demands vary during the day and season and from person to person [4, 9]. In Figure 1.3 the interesting wavelength range for smart windows and the solar energy distribution is presented. However, the conventional electrochromic materials described above are not able to perform individually and selectively in the whole solar range but they are rather exhibiting a broad band which cannot be tuned. For this reason, a new class of electrochromic materials has been lately engineered where the plasmonic properties of nanocrystallites are exploit (plasmonic electrochromism) [4]. Such materials are ITO

(Indium Tin Oxide) nanocrystals embedded in amorphous NbO_x (nanocrystal-in-glass) [10] or amorphous NbO_x infiltrated in nanocrystallites WO_{3-x} pores [11]. Firstly, the absorption/reflection band in these materials can be tuned according to the free carriers concentration (from visible to the near infrared region [4]), secondly the combination of two different materials with complementary optical responses (one in the NIR and the other one in the visible range) could enable a dual band or a tailored response according to the applied potential and thirdly these materials exhibit enhanced optical properties and electrochemical stability [11].

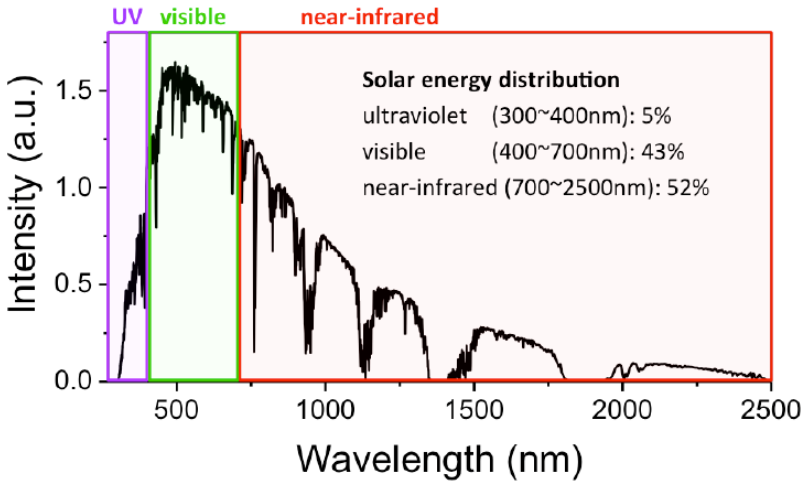

Figure 1.3 [11]: Solar energy distribution

Moreover, the optical changes should take place on a time scale that is comparable with the eyes ability to adapt to light. Therefore the switching kinetics vary from a few seconds to tens of minutes and they depend on the size of the device and the distance from the contacts of the device [3]. For example, if a 240 cm^{-2} device colors/bleaches in a few seconds, it will take more than 10 min to color/bleach in a larger device which is square meters in size [3]. Many researchers have attempted to determine the limiting mechanisms of the coloring and bleaching currents. Typically, the electron motion is very fast and the determining step is mostly associated with cations transport. However, coloration and bleaching are not symmetric phenomena [12]. Coloration is governed mainly by the properties of the interface between the electrochromic layer and the cation injecting contact (due to the development of an electromotive force which opposes the applied potential), while bleaching is determined by cation transport in the film (space charge limited current) [12]. Under certain conditions, diffusion becomes significant as well and the chemical diffusion coefficient of cations can be calculated [13]. Nevertheless other parameters could be also involved in the limitation of current (e.g. substrate or film resistance) and thereby the dependence of current with time is not always straightforward [14].

The durability of the electrochromic devices is another critical parameter for their large-scale implementation. According to E. L. Runnerstrom et al. [4] an ideal smart window should be stable beyond 50 000 cycles. In Table 1.1 different tungsten oxide-based devices are presented with some of their electrochromic characteristics. More devices can be found

in the same reference and in references [8, 15-18]. From the systems presented below, it is manifested that the most stable device (100000 cycles) is a 2400 cm^{-2} WO_3/NiO system with Ta_2O_5 as an electrolyte.

Table 1.1: Data for tungsten oxide-based electrochromic devices (table retrieved from the work of R. Baetens et al. in 2010 [2]). G denotes glass, P denotes polymer and the subscript for T denotes the wavelength in nm for which the values have been obtained

	Size (cm^2)	T (–)	cycles	$\tau_{c/b}$ (s)	Reference
WO_3-based construction					
G|ITO|WO_3|PVB:$LiClO_4$|$CeTiO_x$|ITO|G	100	T_{sol} 0.73–0.045 T_{vis} 0.81–0.07	16×10^3	60	Schlotter et al. [120]
WO_3|NiO-based construction					
G|ITO|WO_3|PMMA-PC-Li^+|NiO|ITO|G	–	T_{600} 0.78–0.31	10^4	–	Lechner and Thomas [80]
G|ITO|WO_3|ZrP · xH_2O|ZrO_2|NiO|ITO|G	25	T_{vis} 0.74–0.38 T_{sol} 0.53–0.25	–	60	Azens et al. [7] Karlsson and Roos [70]
G|SnO_2|WO_3|PVDF-Li^+|NiO:Li|SnO_2|G	7	T_{vis} 0.75–0.02	–	–	Michalak et al. [95]
G|ITO|WO_3|Ta_2O_5|NiO|ITO|G	2400	T_{vis} 0.73–0.18 T_{sol} 0.55–0.11	10^5	–	Nagai et al. [152]
G|SnO_2|WO_3|PEO/PEGMA:Li^+|NiO:Li|SnO_2|G	144	T_{vis} 0.70–0.27	–	120	Penissi et al. [112]
G/P|ITO|WO_3|ZrP|ZrO_2|NiO|ITO|G/P	20	T_{vis} 0.75–0.14	10^3	180/60	Kullman et al. [73]
P|ITO|WO_3|PMMA-PPG-Li^+|NiO|ITO|P	220	T_{550} 0.70–0.35	5×10^3	200	Granqvist et al. [51]
G|FTO|WO_3|P-3|NiO|FTO|G	12.5	T_{vis} 0.58–0.06	10^3	2	Zelazowska [150]
WO_3|IrO_2-based construction					
G/P|ITO|WO_3|Ta_2O_5|IrO_2|ITO	30	T_{550} 0.70–0.18	3.5×10^4	–	O'Brien et al. [101]
WO_3|Polymer-based construction					
G|ITO|WO_3|PAMPS|PANI|ITO|G	2	T_{sol} 0.74–0.35	–	11/11	Jelle and Hagen [64]
G|ITO|WO_3|PAMPS|PB|PANI|ITO|G	2	T_{sol} 0.73–0.23	4×10^3	34/23	Jelle and Hagen [64]
G|ITO|WO_3|PAMPS|PB|PANI|ITO|G (another version)	2.8	T_{sol} 0.64–0.08	–	300/100	Jelle and Hagen [65]
G|SnO_2|WO_3|PVSA:PVP:H^+|PB|SnO_2|G	155	T_{550} 0.72–0.06	2×10^4	30	Ho [59]
G|ITO|WO_3|PAMPS:Li|PANI-CSA|AR|ZnSe|AR	–	R_{1200} 0.65–0.22	900	9	Topart and Hourquebie [134]
P|ITO|WO_3:H_2O|PVDF-HFP-Li^+|PANI|ITO|P	–	T_{800} 0.12–0.02	–	–	Marcel and Tarascon [94]

The degradation of the electrochromic devices is usually stemming from the excess of water (especially in amorphous films) [8], the inability of materials to release all the inserted charge (irreversibility) and the continuous movement of cations in and out of the material. As it will be discussed in the following paragraph in more detail, the main mechanism for cations insertion and ejection is intercalation and de-intercalation through the structural voids of the metal-oxide which results in a long-term degradation [1]. Alternatively, it was found that the use of nanocrystalline/nanostructured films with high surface areas improves their sustainability (and optical properties) by evoking a pseudocapacitive behavior [1, 4, 19]. In that way, the coloration is confined on the surface of the nanograins and their interfaces, avoiding the possibly detrimental ion intercalation [4].

Finally, the electrochromic devices should exhibit high optical transparency without any visible defects and cracks and they should be cost-friendly for large-scale productions [3]. In fact, the latter is the main reason for the slow acceptance of smart windows in a large market [5]. In a study published in 2010 it was estimated that an electrochromic window costs 50-100 $ per ft^2 (500-1000 € per m^2) and the target price in order to render these windows cost-effective and sustainable was 20 $ per ft^2 (200 € per m^2) [5]. Two approaches are recommended by the researchers in order to render the electrochromic devices cost-effective: 1) development of atmospheric pressure solution-based deposition methods to eliminate the expense associated with vacuum processing (sputtering process is the most popular large-scale manufacturing technique) 2) manufacture on flexible polymeric substrates for a post-implementation (retrofit) on already existing windows (roll to roll). For the former, the spray pyrolysis method is highly recommended as a solution processing

technique for large scale productions [5]. This method which will be discussed extensively in chapter 5 satisfies many of the industrial characteristics, such as fast and continuous production rates [20-22], without requiring vacuum conditions [22, 23]. In this phD, we explored the synthesis of templated tungsten oxide films via the ultrasonic spray pyrolysis technique and the results are presented in chapter 5.

For the electrochemical investigation, we used a simple laboratory electrochemical cell for our studies as illustrated in chapter 3 (Figure 3.3), where tungsten oxide films constituted the working electrode and $LiClO_4$/propylene carbonate was the Li^+ conductor. In most experiments, lithium foil was used as a reference and a counter electrode respectively. In the next paragraph, a more detailed discussion on electrochromic tungsten oxide films will be presented.

1.1.2 Tungsten oxide

Electrochromic tungsten oxide films were the firsts to be studied for electrochromic applications in 1969 [24] and since then are the most elaborately discussed materials due to their prominent optical properties. This material consists of corner-sharing octahedra where their phase classification is based on the tilting angles and rotation direction of WO_6 in respect to the ideal perovskite cubic structure (ReO_3) (Figure 1.4) [25]. These perovskite polymorphs can be found as layered crystalline hydrated structures ($WO_3.nH_2O$) [26-30], pure crystalline WO_3, sub-stoichiometric WO_{3-x} or amorphous films. In the latter case, the network consists of distorted corner-sharing octahedra with no long-range periodicity. Contrarily, J. V. Gabrusenoks et al. [31] supported that the amorphous films do not possess a continuous network but rather different types of clusters comprised by octahedra.

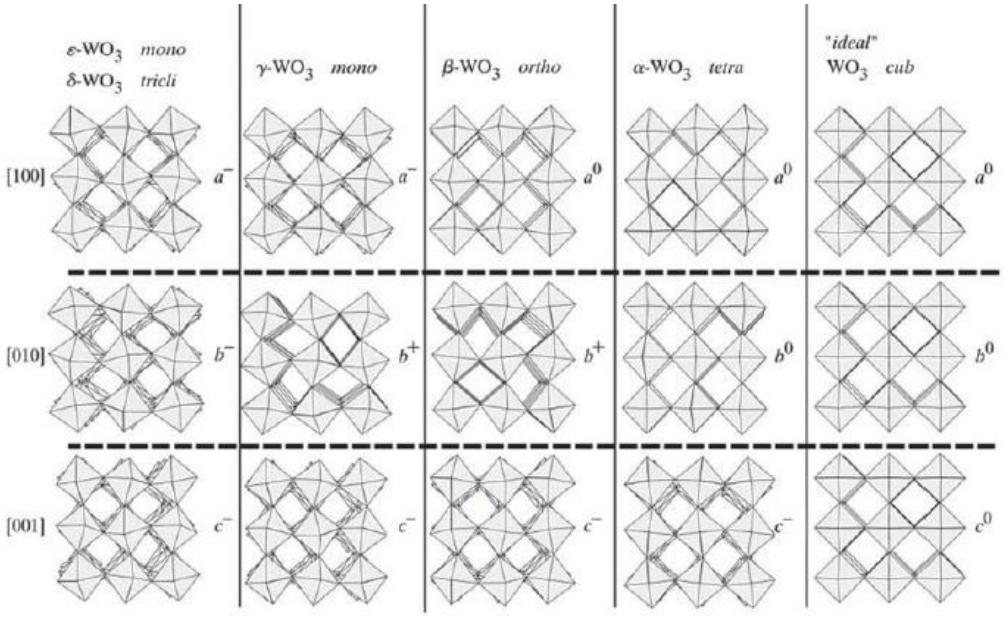

Figure 1.4[25]: Different polymorphs of WO_3 where ε refers to monoclinic II, δ to the triclinic structure, γ to monoclinic I, β to orthormbic and α to the tetragonal WO_3 structure

There are different hydrated tungsten oxide forms ($WO_3.nH_2O$) amorphous and crystallines such as $WO_3.2H_2O$, $WO_3.H_2O$, $WO_3.0.5H_2O$, $WO_3.0.33H_2O$ etc. [26-29]. All these hydrates are comprised by layers of corner sharing octahedra, with water molecules between these layers [26, 30]. For example, $WO_3.2H_2O$ is comprised by $WO_5(OH_2)$ octahedra where one water molecule is intercalated between the layers [25, 30]. Depending on the initial polyanions in the starting solution the progression of species in different stages and the final solid form varies [26, 27, 32].

Annealing $WO_3.nH_2O$, give rise to different crystal structures of non-hydrated WO_3 (Figure 1.4). Many of these structures are stable at high or at very low temperatures and usually only triclinic and monoclinic I structures are observed at room temperature, unless special conditions are employed. For example, cubic WO_3 was detected by XRD when a chelating agent was used in the starting solution [33]. A hexagonal and a pyrochlore metastable non-compact WO_3 phases have also been isolated [30, 34-36]. It has been cited in a few reports that the open structure of the hexagonal phase could be beneficial for the electrochromic properties of these materials for the facile inter- and de-intercalation of cations [37, 38].

The non-stoichiometry is usually characterized by lack of oxygen (oxygen deficiency (WO_{3-x})). This is structurally interpreted as a conversion of corner sharing octahedra into edge sharing. This property, has an impact on the conductive, optical and chemical properties of the films as it will be discussed in the next paragraph [25].

Overall, many studies have investigated and manifested the presence of different tungsten oxides (hydrated or not) via Raman, IR and/or XRD studies and their structural differences have been pointed out [27, 28, 30, 32, 34].

1.1.3 Electrochromism in tungsten oxide

The phenomenon of electrochromism is generally expressed with the following equation [39]:

$$WO_3\ (transparent) + xe^- + xM^+ \rightleftharpoons M_xWO_3\ (Blue)$$

The above equation involves the simultaneous insertion (or extraction) of electrons (e^-) and cations (M^+) and the emerging W^{5+} (during insertion) centers induce coloration. The direction of the reaction depends on the sign of the voltage. Generally, the x value from the above equation can be calculated from the formula:

$$x = \frac{QM}{eAdpN_A}$$

where Q the total charge, M depicts the molar mass of tungsten oxide, d is the thickness, p is the density of the film (g/cm^3), e is the elementary charge and N_A is Avogadro's constant [40]. For proton insertion an upper limit of x =0.5 was found [39]. In our case, the exact molecular weight and density are unknown and therefore only vague approximations can be realized.

The way that electrons interact with the material in tungsten oxide during coloration differs from amorphous and crystalline networks [39].

More specifically, in amorphous films, it is proposed that coloration emerges from the electrons exchange between W^5 and adjacent W^{6+} ions (intervalence charge-transfer transition) [31, 39]. According to J.V. Gabrusenoks et al. [31] the highly distorted octahedra in amorphous materials give rice to broad localized state bands at the bottom of the conduction band and on top of the valence band. Upon electrons insertion an overlap with empty 5d states of neighbouring W^{6+} occurs and an optical transfer is obtained. In other cases it was alternatively proposed that the electrons insertion induces a lattice distortion around the tungsten ion and a bound polaron (a combined lattice polarization charge induced by an excess charge carrier) is obtained which then absorbs photons and moves from one site (W^{5+}) to the other (W^{6+}) [40, 41].

On the other hand, the inserted cations do not play an essential role in the color-center formation but they are rather compensating the excess of the electron charge by residing in the cavities of the perovskite-like structure as depicted in Figure 1.5 [40, 41].

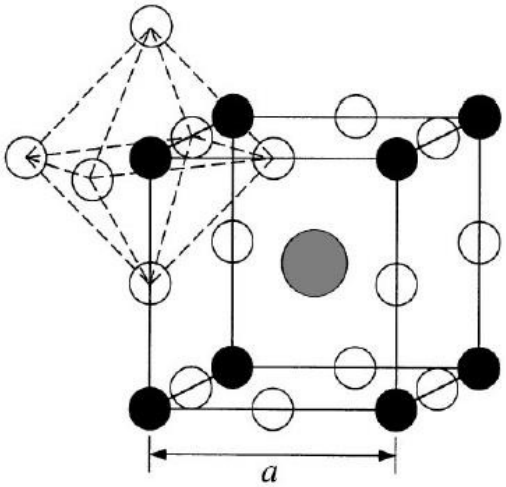

Figure 1.5 [42]: Lithium (or sodium) intercalation in a cubic perovskite structure. Solid and open circles depict the tungsten and oxygen atoms respectively. In the center an intercalated cation is depicted.

Contrarily, in other publications it was suggested that cations not only reside in the structural cavities of the material but they also interact with the inorganic network either by disrupting the W-O-W bonds and creating new W=O bonds [43-48] or by condensing two W=O terminal groups and forming M_2O (where M is the inserted cation) [40, 48]. In any case W^{5+} colored centers (and probably polarons [40]) are formed. Lee et al. [49] presented another possibility for cations insertion. They claimed that it is possible that the inserted electrons result in sub-stoichiometric WO_2 (W^{4+} states) and free Li_2O. This reaction did not lead to any coloration since no W^{5+} was produced. Sub-stoichiometry (WO_x) in perovskite-like structures such as in tungsten oxide, is a common structural defect which is thought to contribute in the coloration of the films [25, 50, 51]. For example, E. Avendano et al. [50] suggested that in sub-stoichiometric films not only transitions between

W^{6+} and W^{5+} are taking place but also W^{5+} to W^{4+} and W^{6+} to W^{4+}. Lee et al. [41] further supported that in the as-deposited sub-stoichiometric films only W^{6+} and W^{4+} states exists which explains the absence of coloration in the as-prepared materials (no W^{5+} optical centers). Upon insertion, polaron transitions between W^{4+} to W^{5+} and W^{5+} to W^{6+} are taking place. According to S.K Deb et al. [51] the presence of oxygen deficiency creates extra in-gap states which may be responsible for coloration. All these explain the better electrochromic properties of the sub-stoichiometric films [49]. Contrarily it was found that excess of oxygen in sputtered films resulted in irreversible lithium trapping in defect positions which do not contribute to the coloration process [52].

In crystalline films, none of the above theories apply. Alternatively, a Drude-like model is proposed where electrons are entering in extended states rather than localized. The electrons in crystalline films undergo scattering and this leads to high reflectance in the near-infrared region rather than absorption in the visible range [42, 53]. In addition, the insertion of cations in crystalline films induces some structural modifications which result in the conversion of one crystalline phase to more symmetric phases (e.g. from monoclinic to tetragonal and tetragonal to cubic) [38, 54, 55]. C. Guéry et al. [28] based on infrared spectroscopy observed that the structural distortions which occur upon cation intercalation vary according to the initial crystalline phase of the material.

In this phD we selected to work with amorphous rather than crystalline films. It has already been documented in the literature that amorphous films exhibit better electrochromic performance than the crystalline films [4, 39]. S. Sallard et al. [54] studied the electrochromic properties of WO_3 films with varying degrees of crystallinity and they found that crystalline films increase the energy barrier for cations insertion and subsequently their charge capacity and coloration properties [12] are inferior compared to the amorphous films. The latter possess distorted open porous structures [31] which facilitate the insertion and de-insertion of cations and thereby their electrochromic properties.

Because of the benefits a porous structure has to offer, the goal of this PhD was to investigate the impact of porosity on the electrochromic properties of tungsten oxide films. The porosity was intentionally incorporated in these films via the soft templating method. This method entails the formation of a network around a structure-directing agent (surfactants and polymers) which acts as a pores template. Upon the removal of the template the pores are liberated preserving (ideally) the structural properties of the structure-directing agent. In the next paragraph a brief discussion on the pores properties along with more details on the templating method will be presented.

1.1.4 Benefits of porous materials

Porous materials gained great attention as host frameworks for different applications since 1992, with the publication of Kresge et al. [56]. This group (Mobil Research and Development Corporation) set the foundations for the soft templating technique by the use of supramolecular assemblies as structure directing agents. This breakthrough has led to

the production of periodically porous structures with larger pore sizes (mesopores, 2-50 nm) compared to their ancestors, zeolites (pore sizes <2 nm). Moreover, this class of porous materials possesses tunable and lower size dispersity (compared to previous mesoporous materials) and high specific surface areas (>1000 m^2g^{-1} for the lower density silicates) [56-58]. The latter, is very crucial for the different applications, since the presence of accessed porosity enables the interaction of reactants not only with the external surface of the material but also with the bulk (see the scheme in Figure 1.6) [58].

Figure 1.6: Interaction of reactants (red bullets) with a dense (left) and an interconnected porous material (right)

At early years, most research was focused on silica (SiO_2) as an extended study of zeolites, because unlike the transition metal oxides the sol-gel chemistry of Si is simpler to control [59]. Moreover, other phenomena could lead to the collapse of the porous structures at elevated temperatures in metal oxides, such as redox reactions (multivalence metals), phase transformations and crystallization [59, 60]. However, with the course of time the introduction of porosity was expanded to transition metals such as TiO_2, ZrO_2, Al_2O_3, Nb_2O_5, Ta_2O_5, WO_3, HfO_2, SnO_2, mixed oxides such as $SiAlO_{3.5}$, $SiTiO_4$, $ZrTiO_4$, Al_2TiO_5, Zr W_2O_8 etc [59, 61, 62] or metal sulfides [63], metal phosphates [63, 64], doped materials and carbons [64, 65]. Furthermore, materials with different shapes such as powders, thin films, monoliths, fibers etc emerged [65].

Because of the aforementioned properties, the versatile number of inorganic frameworks, along with the possibility of functionalizing the pores'walls [66], porous materials find applications in a wide range of fields such as catalysis [58, 59, 63], ion exchange [58], adsorption [58, 63], photocatalysis (photodegradation of organic pollutants), dye-sensitized solar cells, self-cleaning, antireflective antifogging coatings [59, 67], low k dielectric materials [63, 67], low refractive index and thermal insulating films [67], electrochromic films [67], supercapacitors for energy storage [67], biosensors/biocatalysts [59, 67], gas sensors (NO_2, relative humidity, CO_2, different chemical vapours) [67], photonic crystals [67], lithium batteries [68] etc.

Compared to their dense counterparts, porous films exhibit enhanced performance based on their specific surface area, the pore accessibility, the chemical nature of the pore surface and the pore size and topology [67, 69]. For example, in intercalation applications (lithium batteries, electrochromism etc), the presence of pores facilitates the transfer of cations in the interior of the host, enables higher flux and shorter diffusion paths for the cations by

allowing the penetration of the electrolyte inside the film. In addition, according to W-T Wu et al. [70] pores are behaving as surface ''defects'' which possess high chemical potential, favoring the electrochemical action of the network at the surface. Moreover porous materials are more sustainable towards mechanical stresses during the insertion of cations [68]. In films, apart from the undoubting benefits of porosity, the presence of surfactants in the coating solution offers additional advantages as they subside the formation of surface defects like cracks and they offer better spreading of the coating solution on the substrate [71].

As a general rule, the pores are classified according to their size: micropores (<2nm), mesopores (2-50nm) and macropores (>50nm) [58]. For some applications, hierarchical pores are necessary as well (controlled co-existence of pores with different dimensions).

In this PhD, we were primarily interested in the production of ***mesoporous films*** by the ***soft-templating method***. In this method amphiphilic organic molecules (surfactants) are used as structure-directing agents (templates) for the formation of a mesoporous structure [59, 66]. More specifically, the hydrophilic part of the surfactant interacts with the inorganic precursor/network either with electrostatic, hydrogen bonding, covalent (chelating) or van der Waals forces, depending on the pH and the nature of the surfactant [59, 61, 63, 72]. This interaction is very crucial for the formation of the mesostructure and it is imperative to remain intact during the hydrolysis and condensation of the network (Figure 1.7) [59].

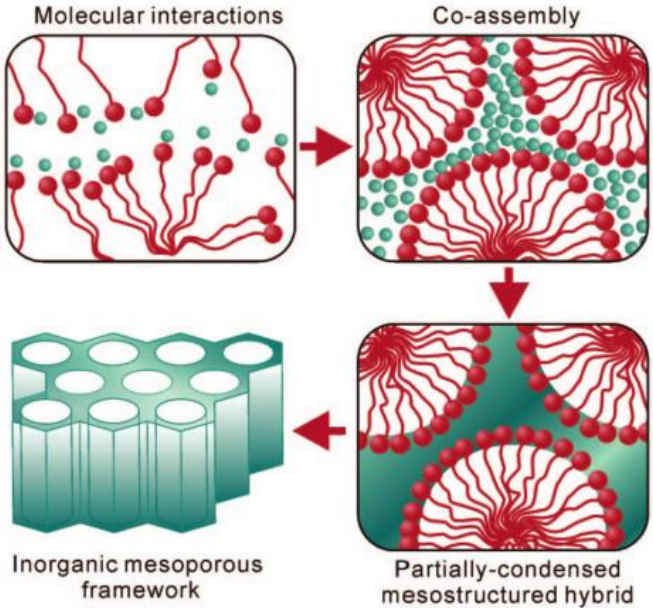

Figure 1.7 [59]: A sketch illustrating the main steps for the formation of mesoporous materials via the soft-templating method

Depending on the experimental conditions (pH, ionic strength, reaction time, solution composition, concentrations etc.), these molecules adopt different micellar architectures (Figure 1.8) in the presence of an inorganic precursor, which lead to the corresponding

uniform porous structures upon their removal (usually by calcination, solvent extraction, UV-O_3 [73]) [59, 64, 66, 73].

The surfactants could be ionic (such as Cetyl Trimethyl Ammonium Bromide, CTAB) or non-ionic (such as triblock co-polymers, e.g. P123, $EO_{20}PO_{70}EO_{20}$, oligomers) [59, 64]. Table 1.2 lists some of the surfactants that have been used in the literature to synthesize mesoporous tungsten oxide films. In this PhD, Brij-56 (or Brij-C10) was used as a structure directing agent ($C_{16}EO_{10}$). This surfactant is an oligomer and produces pores with a small size (2-3 nm). The privilege of oligomers, is that they possess small hydrophilic segments, rendering the pores more sustainable towards thermal treatment. It is more difficult to decompose surfactants with higher hydrophilic chains (such as P123) and preserve an organized mesostructure due to stronger interactions with the inorganic framework [74].

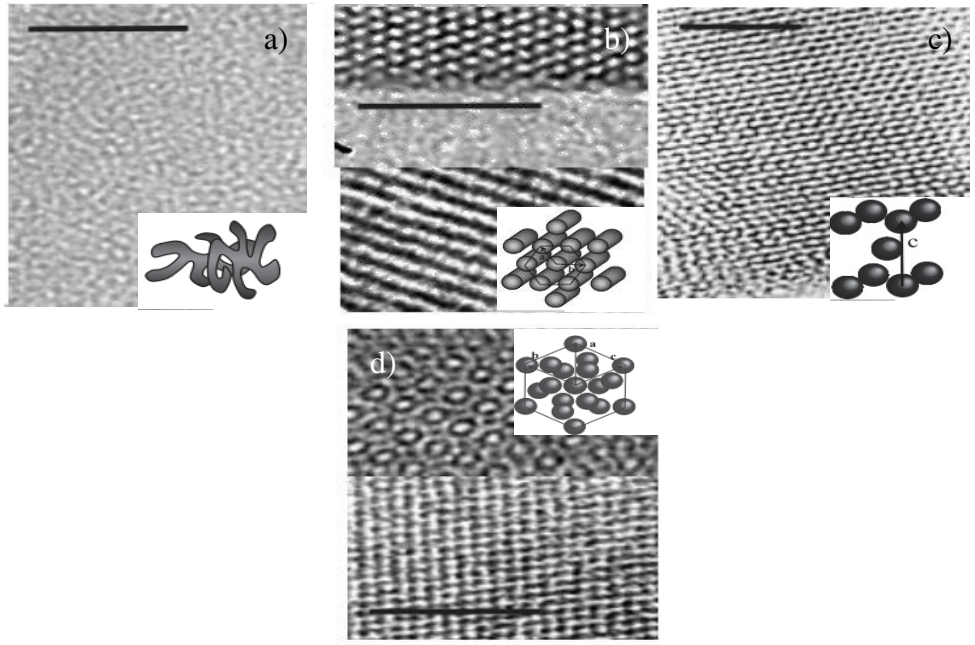

Figure 1.8 [73]: TEM micrographs of porous architectures of CTAB/Si system and their corresponding models a) worm-like structure b) p6m two-dimensional hexagonal arrangement c) $P6_3/mmc$ three-dimensional hexagonal arrangements d) cubic Pm3n organization

As shown in Table 1.2 the soft-templating method is compatible with many different deposition techniques [65]. In this study, we prepared mesoporous films with a conventional technique (dip-coating) at first, in order to exploit their electrochemical properties in the presence and absence of porosity. Next, we investigated the possibility of preparing porous templated films with the electrodeposition method. Finally we used spray pyrolysis (a technique not so commonly combined with templating) to prepare porous films in order to primarily proof the combatibility of these two methods and then to study the electrochemical/optical properties of the emerging films.

Table 1.2: Porous tungsten oxide films synthesized with the soft-templating method and combined with different processing routes

Processing route	Surfactants	Emerging mesostructures	References
dip-coating	P123 $(PEO)_{20}(PPO)_{70}(PEO)_{20}$	2D hexagonal	[75]
	$C_{14}H_{24}EO_{20}$ (TMDD)	worm-like	[76]
	$PIB_{89}EO_{79}$ (KLE)[1]	cubic	[54]
	$EO_{100}PO_{64}EO_{100}$ (F127)	random porosity	[77]
	$C_{16}EO_{10}$ (Brij-56)	hexagonal	[74, 78, 79]
spin-coating	Polystyrene-b-polyacrylic acid (PS-b-PAA)	interstitial porosity	[80]
	P123	random porosity	[81]
	Poly(styrene-co-allyl-alcohol)	random porosity	[82]
	PEG 20000	random porosity	[70]
anodic growth	PEG	interstitial porosity	[83]
cathodic growth	SDS		[84]
	PEG 400		[85]
spraying	HTAB-PEG	random porosity	[86]
	P123	interstitial porosity	[87, 88]

[1] $H(CH_2CH_2CH_2(CH)CH_2CH_3)_{89}(OCH_2CH_2)_{79}OH$

In every case, the sol-gel method was employed for the formation of the inorganic network around the organic template. This technique entails the formation of a solid inorganic (or hybrid) network from a solution which contains the inorganic precursors [89]. The inorganic precursors could be metal-organic compounds (alkoxides) or inorganic salts in aqueous solutions [90, 91]. Either way, the chemistry is based in two types of reactions: i) hydrolysis and ii) condensation [90, 92]. At the beginning, ***a sol*** is formed (a colloidal suspension where the dispersed phase is solid). At this stage, pH, salts or polymers can determine the evolution of the particles by rendering their surface electrically charged or neutral (pzc point, point of zero charge) [91]. As the reactions are progressing ***a gel*** might form, a three–dimensional network where sol particles, agglomerates and solvent is trapped in its pores. Ageing and drying lead to the desired material form, such as powders, monoliths, films etc.

In this study, the sol-gel technique was combined with the soft-templating method in order to prepare mesoporous tungsten oxide films. A challenging goal when working with these methods is to preserve the mesophase architecture in every step of the experimental process. In the initial solution a control over the hydrolysis and condensation reactions is very essential for the preservation of the mesostructure. In fact, the polycondensation should be the slowest process during templating. Template-inorganic precursor interface and template's self-assembly should occur first [66]. In order to achieve that, the pH can be fixed close to the isoelectric point of the $M(OH)_x$ precursor [73].In that way, hydrolysis is fast enough in order to obtain the more stable precursor oligomers and prevent the uncontrolled condensation and precipitation of unwanted non-porous products [73]. For example, stable tungstic acid sols are produced (at least for a short period of time) through

the acidification of sodium tungstate solutions with a proton exchange resin at around its PZC [93]. Others [94, 95], dilute their precursor in ethanol instead of water in order to control the excessive condensation. In this phD we were primarily interested in more benign experimental procedures where no or minimum amounts of ethanol are needed. For this reason, we used peroxide and acetate groups as chelating agents to prepare a tungsten complex (APTA, acetylated peroxotungstic acid) protected from excess hydrolysis and condensation. The emerging precursor was stable in aqueous and alcoholic solutions and subsequently the templating process was favored. The protection with chelating agents is well known in the literature especially when working with transition metals. Due to their higher electronegativity and multiple coordination states, transition metals are more susceptible to water compared to the classic silicon chemistry [90]. 2,4 pentanedione [33, 96], H_2O_2 [29], oxalic acid [35], acetic acid [97], citric acid [98] poly(ethylene glycol) [95] are some of the chelating agents that have been used in order to stabilize tungsten precursors.

1.1.5 Scope and objective

The objective of this PhD was to synthesize mesoporous tungsten oxide thin films via the soft-templating technique and investigate the impact of porosity on their electrochemical/optical properties.

Electrochromic films have intrigued many researchers in the last years for their ability to reversibly modulate the visible/NIR light when a small voltage is applied. This property can contribute in energy efficient applications like smart windows. For this purpose, the electrochromic films should exhibit high optical contrast ($\Delta T\%$), high coloration efficiency (η, cm^2/C), full reversibility and long-term stability. Moreover they should present fast switching kinetics compatible with the human's eye capability to adjust to an optical change.

One way to optimize these properties is to increase the surface area of the electrochromic layers by introducing porosity in their bulk. It is already documented in the literature that the presence of porosity in a system can potentially enhance its electrochemical properties by facilitating the transfer of cations in the interior of the host, enabling higher flux and shorter diffusion paths for the cations by allowing the penetration of the electrolyte inside the film.

In our studies we prepared mesoporous films with three different processing routes: dip-coating, electrodeposition and ultrasonic spray pyrolysis.

The dip-coating technique is typically utilized for the formation of mesostructured films as it is efficiently combined with the EISA (Evaporation Induced Self Assembly) method. The synthesis of well-organized mesostructures allowed us to investigate the electrochemical properties of tungsten oxide films with and without porosity. Based on our studies, we explored the impact of atmospheric water and the abundance of hydroxyls and water molecules in porous films on the electrochromic reaction. The dip-coated films were also studied by Raman spectroscopy before and after Li^+ intercalation and de-intercalation.

Even though porous films exhibit a more active surface for lithium intercalation compared to their dense counterparts their hydrated and more active surface renders them more prone to network disruption and degradation with cycling. On the other hand, dense films exhibit inferior lithium capacity and they irreversibly trap cations in the first cycles which gives them a permanent blue color even after the electrochemical measurement.

Next, we studied the possibility of synthesizing mesoporous films with electrodeposition. Two different surfactants have been used in order to prepare electrodeposited mesoporous tungsten oxide films, a non-ionic surfactant (Brij-56 or Brij-C10) and an anionic polymer (Poly(sodium 4-styrene sulfonate)). The synthesis of mesoporous films via this method appeared to be a challenging task since only random evidences of templating have been collected. Low coverage, no strong evidences of porosity, lack of reproducibility and low electrochemical properties are some of the problems encountered in electrodeposition experiments.

The last part of this thesis was constituted by the preparation of surfactant-assisted porous films with a less conventional pores-generating method, the ultrasonic spray pyrolysis. The interest in the spraying methods is progressively expanding in an industrial level in the last years, due to their cost-effectiveness, their fast and continuous production rates, without requiring vacuum conditions. Therefore, the goal in this last part was to combine the advantages of porous films with the unquestionable privileges that this processing method has to offer. Structural and microstructural characteristics, crystallinity, porosity, thickness, the amount of deposited material and electrochemical/electrochromic properties were investigated in a certain deposition temperature range. Once more all the above characteristics were compared to the surfactant-free films. In this case, the presence of surfactant not only affects the electrochromic properties of the films but it tremendously improves solution's wettability in the investigating temperature and reduces droplets size which eventually determines film deposition.

1.1.6 Outline of the thesis

This chapter presents an overview on the main principles of electrochromism with emphasis on the structural characteristics and electrochemical properties of tungsten oxide films. Additionally, we explain the advantages of introducing porosity onto an inorganic material and display the underlying fundamentals of the sol-gel and the soft-templating technique.

In ***Chapter 2*** we provide some insights on the chemistry of peroxo-tungsten precursors and their derivatives along with our efforts to produce peroxo-tungsten complexes suitable for coating applications.

Chapter 3 discusses the emerging results from the synthesis of mesoporous tungsten oxide films with the *dip-coating* method. A comparison between porous and dense films has been conducted. The films were studied by Transmission Electron Microscopy (TEM), Scanning Electron Microscopy (SEM), Raman and Infrared Spectroscopy (IR), ellipsometry, cyclic voltammetry and chronoamperometry.

Chapter 4 deals with the electrodeposition method and presents all the efforts that have been realized to produce electrodeposited tungsten oxide films in the presence of two surfactants, one non-ionic and one anionic surfactant.

Chapter 5 is dedicated to the study of porous films prepared with the *ultrasonic spray pyrolysis technique*. The structural and electrochromic properties of the films were investigated in the presence and in the absence of surfactant in a certain temperature range. Based on the successful preparation of porous-structured film we proof that templating can be effectively combined with this technique as well.

This manuscript ends with the conclusions and future work ***(chapter 6)***.

1.2 References for Chapter 1

[1] S.-H. Lee, C.E. Tracy, Y. Yan, J.R. Pitts, S.K. Deb, Solid-State Nanocomposite Electrochromic Pseudocapacitors, Electrochemical and Solid-State Letters, 8 (2005) A188-A190.

[2] R. Baetens, B.P. Jelle, A. Gustavsen, Properties, requirements and possibilities of smart windows for dynamic daylight and solar energy control in buildings: A state-of-the-art review, Solar Energy Materials and Solar Cells, 94 (2010) 87-105.

[3] C.G. Granqvist, Electrochromics for smart windows: Oxide-based thin films and devices, Thin Solid Films, 564 (2014) 1-38.

[4] E.L. Runnerstrom, A. Llordes, S.D. Lounis, D.J. Milliron, Nanostructured electrochromic smart windows: traditional materials and NIR-selective plasmonic nanocrystals, Chemical Communications, 50 (2014) 10555-10572.

[5] D.T. Gillaspie, R.C. Tenent, A.C. Dillon, Metal-oxide films for electrochromic applications: present technology and future directions, Journal of Materials Chemistry, 20 (2010) 9585-9592.

[6] N. DeForest, A. Shehabi, J. O'Donnell, G. Garcia, J. Greenblatt, E.S. Lee, S. Selkowitz, D.J. Milliron, United States energy and CO_2 savings potential from deployment of near-infrared electrochromic window glazings, Building and Environment, 89 (2015) 107-117.

[7] R. Ostermann, B. Smarsly, Does mesoporosity enhance thin film properties? A question of electrode material for electrochromism of WO_3, Nanoscale, 1 (2009) 266-270.

[8] C.G. Granqvist, Electrochromism and smart window design, Solid State Ionics, 53–56, Part 1 (1992) 479-489.

[9] C.G. Granqvist, Transparent conductors as solar energy materials: A panoramic review, Solar Energy Materials and Solar Cells, 91 (2007) 1529-1598.

[10] A. Llordes, G. Garcia, J. Gazquez, D.J. Milliron, Tunable near-infrared and visible-light transmittance in nanocrystal-in-glass composites, Nature, 500 (2013) 323-326.

[11] J. Kim, G.K. Ong, Y. Wang, G. LeBlanc, T.E. Williams, T.M. Mattox, B.A. Helms, D.J. Milliron, Nanocomposite Architecture for Rapid, Spectrally-Selective Electrochromic Modulation of Solar Transmittance, Nano letters, 15 (2015) 5574-5579.

[12] B.W. Faughnan, R.S. Crandall, Electrochromic displays based on WO_3, in: J.I. Pankove (Ed.) Display Devices, Springer Berlin Heidelberg1980, pp. 181-211.

[13] J.G. Zhang, C.E. Tracy, D.K. Benson, S.K. Deb, The influence of microstructure on the electrochromic properties of lithium tungsten oxide (Li_xWO_3) thin films. Part I. Ion diffusion and electrochromic properties, J. Mater. Res., 8 (1993) 2649-2656.

[14] J.G. Zhang, D.K. Benson, C.E. Tracy, S.K. Deb, The influence of microstructure on the electrochromic properties of lithium tungsten oxide (Li_xWO_3) films. II. Limiting mechanisms in coloring and bleaching processes, J. Mater. Res., 8 (1993) 2657-2667.

[15] X. Zhang, H. Zhang, Q. Li, H. Luo, An all-solid-state inorganic electrochromic display of WO_3 and NiO films with $LiNbO_3$ ion conductor, Electron Device Letters, IEEE, 21 (2000) 215-217.

[16] A. Azens, G. Vaivars, M. Veszelei, L. Kullman, C.G. Granqvist, Electrochromic devices embodying W oxide/Ni oxide tandem films, Journal of Applied Physics, 89 (2001) 7885-7887.

[17] B.P. Jelle, G. Hagen, Performance of an electrochromic window based on polyaniline, prussian blue and tungsten oxide, Solar Energy Materials and Solar Cells, 58 (1999) 277-286.

[18] Y. Djaoued, S. Balaji, Bruning, R. ning, Electrochromic Devices Based on Porous Tungsten Oxide Thin Films, Journal of Nanomaterials, 2012 (2012) 9.

[19] M.R.J. Scherer, U. Steiner, Efficient Electrochromic Devices Made from 3D Nanotubular Gyroid Networks, Nano letters, 13 (2013) 3005-3010.

[20] Sonotek corporation, investor presentation, (February 2013).

[21] W.-N. Wang, A. Purwanto, I.W. Lenggoro, K. Okuyama, H. Chang, H.D. Jang, Investigation on the Correlations between Droplet and Particle Size Distribution in Ultrasonic Spray Pyrolysis, Industrial & Engineering Chemistry Research, 47 (2008) 1650-1659.

[22] A. Nakaruk, C.C. Sorrell, Conceptual model for spray pyrolysis mechanism: fabrication and annealing of titania thin films, J Coat Technol Res, 7 (2010) 665-676.

[23] C. Guild, S. Biswas, Y. Meng, T. Jafari, A.M. Gaffney, S.L. Suib, Perspectives of spray pyrolysis for facile synthesis of catalysts and thin films: An introduction and summary of recent directions, Catalysis Today, 238 (2014) 87-94.

[24] S.K. Deb, A Novel Electrophotographic System, Appl. Opt., 8 (1969) 192-195.

[25] H. Zheng, J.Z. Ou, M.S. Strano, R.B. Kaner, A. Mitchell, K. Kalantar-zadeh, Nanostructured Tungsten Oxide – Properties, Synthesis, and Applications, Advanced Functional Materials, 21 (2011) 2175-2196.

[26] J. Livage, G. Guzman, Aqueous precursors for electrochromic tungsten oxide hydrates, Solid State Ionics, 84 (1996) 205-211.

[27] L.M. Plyasova, I.Y. Molina, G.N. Kustova, N.A. Rudina, M.I. Borzenko, G.A. Tsirlina, O.A. Petrii, Solid state features of electrocrystallized tungstate films, J. Solid State Electrochem., 9 (2005) 371-379.

[28] C. Guéry, C. Choquet, F. Dujeancourt, J.M. Tarascon, J.C. Lassègues, Infrared and X-ray studies of hydrogen intercalation in different tungsten trioxides and tungsten trioxide hydrates, Journal of Solid State Electrochemistry, 1 (1997) 199-207.

[29] B. Pecquenard, H. Lecacheux, S. Castro-Garcia, J. Livage, Electrochromic Properties of Peroxopolytungstic Acid Thin Films, Journal of Sol-Gel Science and Technology, 13 (1998) 923-927.

[30] M.F. Daniel, B. Desbat, J.C. Lassegues, B. Gerand, M. Figlarz, Infrared and Raman study of WO_3 tungsten trioxides and $WO_3.xH_2O$ tungsten trioxide tydrates, Journal of Solid State Chemistry, 67 (1987) 235-247.

[31] J.V. Gabrusenoks, P.D. Cikmach, A.R. Lusis, J.J. Kleperis, G.M. Ramans, Electrochromic colour centres in amorphous tungsten trioxide thin films, Solid State Ionics, 14 (1984) 25-30.

[32] M. Breedon, P. Spizzirri, M. Taylor, J. du Plessis, D. McCulloch, J. Zhu, L. Yu, Z. Hu, C. Rix, W. Wlodarski, K. Kalantar-zadeh, Synthesis of Nanostructured Tungsten Oxide Thin Films: A Simple, Controllable, Inexpensive, Aqueous Sol−Gel Method, Crystal Growth & Design, 10 (2010) 430-439.

[33] T. Nishide, F. Mizukami, Crystal structures and optical properties of tungsten oxide films prepared by a complexing-agent-assisted sol-gel process, Thin Solid Films, 259 (1995) 212-217.

[34] R. Solarska, B. Alexander, J. Augustynski, Electrochromic and structural characteristics of mesoporous WO_3 films prepared by a sol-gel method, Journal of Solid State Electrochemistry, 8 (2004).

[35] H.M.A. Soliman, A.B. Kashyout, M.S. El Nouby, A.M. Abosehly, Effect of hydrogen peroxide and oxalic acid on electrochromic nanostructured tungsten oxide thin films, International Journal of Electrochemical Science, 7 (2012) 258-271.

[36] L.M. Kuti, S.S. Bhella, V. Thangadurai, Revisiting Tungsten Trioxide Hydrates (TTHs) Synthesis - Is There Anything New?, Inorganic Chemistry (Washington, DC, United States), 48 (2009) 6804-6811.

[37] A.K. Srivastava, M. Deepa, S. Singh, R. Kishore, S.A. Agnihotry, Microstructural and electrochromic characteristics of electrodeposited and annealed WO3 films, Solid State Ionics, 176 (2005) 1161-1168.

[38] B. Yebka, B. Pecquenard, C. Julien, J. Livage, Electrochemical Li^+ insertion in WO_3–$xTiO_2$ mixed oxides, Solid State Ionics, 104 (1997) 169-175.

[39] B.W. Faughnan, R.S. Crandall, Electrochromic displays based on tungsten oxide, Topics in Applied Physics, 40 (1980) 181-211.

[40] M.F. Saenger, T. Höing, B.W. Robertson, R.B. Billa, T. Hofmann, E. Schubert, M. Schubert, Polaron and phonon properties in proton intercalated amorphous tungsten oxide thin films, Physical Review B, 78 (2008) 245205.

[41] S.-H. Lee, H.M. Cheong, J.-G. Zhang, A. Mascarenhas, D.K. Benson, S.K. Deb, Electrochromic mechanism in a-WO_{3-y} thin films, Applied Physics Letters, 74 (1999) 242-244.

[42] C.G. Granqvist, Electrochromic tungsten oxide films: Review of progress 1993–1998, Solar Energy Materials and Solar Cells, 60 (2000) 201-262.

[43] B. Orel, U.O. Krasovec, N. Groselj, M. Kosec, G. Drazic, R. Reisfeld, Gasochromic behavior of sol-gel derived Pd doped peroxopolytungstic acid (W-PTA) nano-composite films, J. Sol-Gel Sci. Technol., 14 (1999) 291-308.

[44] P. Delichere, P. Falaras, M. Froment, A. Hugot-Le Goff, B. Agius, Electrochromism in anodic WO_3 films I: Preparation and physicochemical properties of films in the virgin and coloured states, Thin Solid Films, 161 (1988) 35-46.

[45] J.L. Paul, J.C. Lassègues, Infrared Spectroscopic Study of Sputtered Tungsten Oxide Films, Journal of Solid State Chemistry, 106 (1993) 357-371.

[46] B. Orel, N. Grošelj, U.O. Krašovec, R. Ješe, A. Georg, IR Spectroscopic Investigations of Gasochromic and Electrochromic Sol-Gel—Derived Peroxotungstic Acid/Ormosil Composite and Crystalline WO_3 Films, Journal of Sol-Gel Science and Technology, 24 (2002) 5-22.

[47] G. Leftheriotis, S. Papaefthimiou, P. Yianoulis, The effect of water on the electrochromic properties of WO_3 films prepared by vacuum and chemical methods, Solar Energy Materials & Solar Cells, 83 (2004) 115-124.

[48] J.G. Zhang, D.K. Benson, C.E. Tracy, S.K. Deb, A.W. Czanderna, C. Bechinger, Chromic Mechanism in Amorphous WO_3 Films, Journal of the Electrochemical Society, 144 (1997) 2022-2026.

[49] S.-H. Lee, H.M. Cheong, C.E. Tracy, A. Mascarenhas, A.W. Czanderna, S.K. Deb, Electrochromic coloration efficiency of a-WO_{3-y} thin films as a function of oxygen deficiency, Applied Physics Letters, 75 (1999) 1541-1543.

[50] E. Avendano, L. Berggren, G. Niklasson, C. Granqvist, A. Azens, Electrochromic materials and devices: Brief survey and new data on optical absorption in tungsten oxide and nickel oxide films, Thin Solid Films, 496 (2006) 30-36.

[51] S.K. Deb, Opportunities and challenges in science and technology of WO_3 for electrochromic and related applications, Solar Energy Materials and Solar Cells, 92 (2008) 245-258.

[52] T.J. Vink, E.P. Boonekamp, R.G.F.A. Verbeek, Y. Tamminga, Lithium trapping at excess oxygen in sputter-deposited a-WO_3 films, J. Appl. Phys., 85 (1999) 1540-1544.

[53] C.G. Granqvist, Chapter 10 - Tungsten Oxide Films: Theoretical Models for the Optical Properties, in: C.G. Granqvist (Ed.) Handbook of Inorganic Electrochromic Materials, Elsevier Science B.V., Amsterdam, 1995, pp. 175-192.

[54] S. Sallard, T. Brezesinski, B.M. Smarsly, Electrochromic Stability of WO_3 Thin Films with Nanometer-Scale Periodicity and Varying Degrees of Crystallinity, The Journal of Physical Chemistry C, 111 (2007) 7200-7206.

[55] S.-H. Lee, M.J. Seong, H.M. Cheong, E. Ozkan, E.C. Tracy, S.K. Deb, Effect of crystallinity on electrochromic mechanism of Li_xWO_3 thin films, Solid State Ionics, 156 (2003) 447-452.

[56] C.T. Kresge, M.E. Leonowicz, W.J. Roth, J.C. Vartuli, J.S. Beck, Ordered mesoporous molecular sieves synthesized by a liquid-crystal template mechanism, Nature, 359 (1992) 710-712.

[57] J.Y. Ying, C.P. Mehnert, M.S. Wong, Synthesis and applications of supramolecular-templated mesoporous materials, Angewandte Chemie, International Edition, 38 (1999) 56-77.

[58] M.E. Davis, Ordered porous materials for emerging applications, Nature, 417 (2002) 813-821.

[59] S.W. Boettcher, J. Fan, C.-K. Tsung, Q. Shi, G.D. Stucky, Harnessing the Sol–Gel Process for the Assembly of Non-Silicate Mesostructured Oxide Materials, Accounts of Chemical Research, 40 (2007) 784-792.

[60] J.N. Kondo, K. Domen, Crystallization of Mesoporous Metal Oxides†, Chemistry of Materials, 20 (2008) 835-847.

[61] P. Yang, D. Zhao, D.I. Margolese, B.F. Chmelka, G.D. Stucky, Generalized syntheses of large-pore mesoporous metal oxides with semicrystalline frameworks, Nature, 396 (1998) 152-155.

[62] C. Yu, B. Tian, D. Zhao, Recent advances in the synthesis of non-siliceous mesoporous materials, Current Opinion in Solid State and Materials Science, 7 (2003) 191-197.

[63] F. Hoffmann, M. Cornelius, J. Morell, M. Fröba, Silica-Based Mesoporous Organic–Inorganic Hybrid Materials, Angewandte Chemie International Edition, 45 (2006) 3216-3251.

[64] Y. Wan, Y. Shi, D. Zhao, Designed synthesis of mesoporous solids via nonionic-surfactant-templating approach, Chemical Communications (Cambridge, United Kingdom), (2007) 897-926.

[65] C. Sanchez, C. Boissière, D. Grosso, C. Laberty, L. Nicole, Design, Synthesis, and Properties of Inorganic and Hybrid Thin Films Having Periodically Organized Nanoporosity†, Chemistry of Materials, 20 (2008) 682-737.

[66] G.J.A.A. Soler-Illia, P. Innocenzi, Mesoporous Hybrid Thin Films: The Physics and Chemistry Beneath, Chemistry – A European Journal, 12 (2006) 4478-4494.

[67] P. Innocenzi, L. Malfatti, Mesoporous thin films: properties and applications, Chemical Society Reviews, 42 (2013) 4198-4216.

[68] N. Krins, J.D. Bass, D. Grosso, C. Henrist, R. Delaigle, E.M. Gaigneaux, R. Cloots, B. Vertruyen, C. Sanchez, $NbVO_5$ Mesoporous Thin Films by Evaporation Induced Micelles Packing: Pore Size Dependence of the Mechanical Stability upon Thermal Treatment and Li Insertion/Extraction, Chemistry of Materials, 23 (2011) 4124-4131.

[69] P. Innocenzi, L. Malfatti, G.J.A.A. Soler-Illia, Hierarchical Mesoporous Films: From Self-Assembly to Porosity with Different Length Scales, Chemistry of Materials, 23 (2011) 2501-2509.

[70] W.-T. Wu, W.-P. Liao, L.-Y. Chen, J.-S. Chen, J.-J. Wu, Outperformed electrochromic behavior of poly(ethylene glycol)-template nanostructured tungsten oxide films with enhanced charge transfer/transport characteristics, Physical Chemistry Chemical Physics, 11 (2009) 9751-9758.

[71] T. Brezesinski, D.F. Rohlfing, S. Sallard, M. Antonietti, B.M. Smarsly, Highly crystalline WO3 thin films with ordered 3D mesoporosity and improved electrochromic performance, Small, 2 (2006) 1203-1211.

[72] G.J.d.A.A. Soler-Illia, C. Sanchez, Interactions between poly(ethylene oxide)-based surfactants and transition metal alkoxides: their role in the templated construction of mesostructured hybrid organic-inorganic composites, New Journal of Chemistry, 24 (2000) 493-499.

[73] D. Grosso, F. Cagnol, G.J.d.A.A. Soler-Illia, E.L. Crepaldi, H. Amenitsch, A. Brunet-Bruneau, A. Bourgeois, C. Sanchez, Fundamentals of Mesostructuring Through Evaporation-Induced Self-Assembly, Advanced Functional Materials, 14 (2004) 309-322.

[74] W. Wang, Y. Pang, S.N.B. Hodgson, XRD studies of thermally stable mesoporous tungsten oxide synthesised by a templated sol–gel process from tungstic acid precursor, Microporous and Mesoporous Materials, 121 (2009) 121-128.

[75] Z.-M. Qi, H.-S. Zhou, T. Watanabe, I. Honma, Synthesis, characterization and optical gas-sensing application of block copolymer templated mesostructured peroxopolytungstic acid films, Journal of Materials Chemistry, 14 (2004) 3540-3547.

[76] Y. Zhang, J. Yuan, J. Le, L. Song, X. Hu, Structural and electrochromic properties of tungsten oxide prepared by surfactant-assisted process, Solar Energy Materials & Solar Cells, 93 (2009) 1338-1344.

[77] L.G. Teoh, Y.M. Hon, J. Shieh, W.H. Lai, M.H. Hon, Sensitivity properties of a novel NO2 gas sensor based on mesoporous WO3 thin film, Sensors and Actuators B: Chemical, 96 (2003) 219-225.

[78] W. Wang, Y. Pang, S.N.B. Hodgson, Preparation, characterisation and electrochromic property of mesostructured tungsten oxide films via a surfactant templated sol–gel process from tungstic acid, Journal of Sol-Gel Science and Technology, 54 (2010) 19-28.

[79] W. Wang, Y. Pang, S.N.B. Hodgson, Design and fabrication of bimodal meso-mesoporous WO_3 thin films and their electrochromic properties, Journal of Materials Chemistry, 20 (2010) 8591.

[80] J. Li, Q.-L. Zhao, G.-Y. Zhang, J.-Z. Chen, L. Zhong, L. Li, J. Huang, Z. Ma, Synthesis of monoclinic WO_3 nanosphere hydrogen gasochromic film via a sol–gel approach using PS-b-PAA diblock copolymer as template, Solid State Sciences, 12 (2010) 1393-1398.

[81] E. Ozkan, S.-H. Lee, P. Liu, C.E. Tracy, F.Z. Tepehan, J.R. Pitts, S.K. Deb, Electrochromic and optical properties of mesoporous tungsten oxide films, Solid State Ionics, 149 (2002) 139-146.

[82] E. Ozkan Zayim, Mesoporous sol–gel WO_3 thin films via poly(styrene-co-allyl-alcohol) copolymer templates, Solid State Ionics, 165 (2003) 65-72.

[83] A. Watcharenwong, W. Chanmanee, N.R. de Tacconi, C.R. Chenthamarakshan, P. Kajitvichyanukul, K. Rajeshwar, Anodic growth of nanoporous WO_3 films: Morphology, photoelectrochemical response and photocatalytic activity for methylene blue and hexavalent chrome conversion, Journal of Electroanalytical Chemistry, 612 (2008) 112-120.

[84] M. Deepa, A.K. Srivastava, S.A. Agnihotry, Influence of annealing on electrochromic performance of template assisted, electrochemically grown, nanostructured assembly of tungsten oxide, Acta Materialia, 54 (2006) 4583-4595.

[85] M. Deepa, M. Kar, D.P. Singh, A.K. Srivastava, S. Ahmad, Influence of polyethylene glycol template on microstructure and electrochromic properties of tungsten oxide, Solar Energy Materials and Solar Cells, 92 (2008) 170-178.

[86] L.M. Bertus, C. Faure, A. Danine, C. Labrugere, G. Campet, A. Rougier, A. Duta, Synthesis and characterization of WO_3 thin films by surfactant assisted spray pyrolysis for electrochromic applications, Materials Chemistry and Physics, 140 (2013) 49-59.

[87] C.-P. Li, F. Lin, R.M. Richards, C. Engtrakul, A.C. Dillon, R.C. Tenent, C.A. Wolden, Ultrasonic spray deposition of high performance WO_3 films using template-assisted sol–gel chemistry, Electrochemistry Communications, 25 (2012) 62-65.

[88] C.-P. Li, F. Lin, R.M. Richards, C. Engtrakul, R.C. Tenent, C.A. Wolden, The influence of sol–gel processing on the electrochromic properties of mesoporous WO_3 films produced by ultrasonic spray deposition, Solar Energy Materials and Solar Cells, 121 (2014) 163-170.

[89] J.W. S.M. Attia, Guangming Wu, Jun Shen and Jianhua Ma, Review on Sol-Gel Derived Coatings: Process, Techniques and Optical Applications, J. Mater. Sci. Technol, 18 (2002) 211-218.

[90] J. Livage, M. Henry, C. Sanchez, Sol-gel chemistry of transition metal oxides, Progress in Solid State Chemistry, 18 (1988) 259-341.

[91] Etienne Duguet, Sol-gel chemistry and engineering backround, www.chimica.unipd.it/gianandrea.rizzi/privata/.../sol-gel.pdf.

[92] J. Livage, C. Sanchez, Sol-gel chemistry, Journal of Non-Crystalline Solids, 145 (1992) 11-19.

[93] J. Livage, D. Ganguli, Sol-gel electrochromic coatings and devices: A review, Solar Energy Materials & Solar Cells, 68 (2001) 365-381.

[94] S. Badilescu, P.V. Ashrit, Study of sol-gel prepared nanostructured WO_3 thin films and composites for electrochromic applications, Solid State Ionics, 158 (2003) 187-197.

[95] C. Santato, M. Odziemkowski, M. Ulmann, J. Augustynski, Crystallographically Oriented Mesoporous WO_3 Films: Synthesis, Characterization, and Applications, Journal of the American Chemical Society, 123 (2001) 10639-10649.

[96] J. Shieh, H.M. Feng, M.H. Hon, H.Y. Juang, WO_3 and W-Ti-O thin-film gas sensors prepared by sol-gel dip-coating, Sensors and Actuators, B: Chemical, B86 (2002) 75-80.

[97] M. Deepa, A.G. Joshi, A.K. Srivastava, S.M. Shivaprasad, S.A. Agnihotry, Electrochromic Nanostructured Tungsten Oxide Films by Sol-gel: Structure and Intercalation Properties, Journal of the Electrochemical Society, 153 (2006) C365-C376.

[98] W. Li, J. Li, X. Wang, J. Ma, Q. Chen, Effect of citric acid on photoelectrochemical properties of tungsten trioxide films prepared by the polymeric precursor method, Appl. Surf. Sci., 256 (2010) 7077-7082

Chapter 2
Tungsten oxide precursors/peroxotungstic acid (PTA) and its acetylated derivative (APTA)

2.1 Stabilization of WO_3 precursors

Different W compounds have been used in the literature as precursors for the formation of tungsten oxide films via the sol-gel method. Tungsten alkoxides (e.g $W(OEt)_6$) [1, 2], oxoalkoxides (e.g $WO(OR)_4$) [1], $WOCl_4$ [3, 4], WCl_6 [5, 6], are some of the precursors which are commercially available and have been successfully used for the formation of WO_3 films. However, these compounds are expensive and highly reactive (see introduction) when mixed with water. Therefore, tungsten alkoxides, chlorides and oxo alkoxides are always handled in alcoholic solutions [1]. On the other hand, as it was already mentioned in the introduction, stable tungstic acid sols are produced (at least for a short period of time) through the acidification of sodium tungstate solutions with a proton exchange resin at around its PZC [1]. However, after a while layered hydrated oxides precipitate, rendering the usage of the solution unsuitable for coating purposes. In order to prevent uncontrolled precipitation chemical modification with the use of complexing agents is usually employed [1, 7].

The precursors that result from chemical modification could be cheaper, more stable in moisture and more benign compared to WCl_6 or $WOCl_4$ dissolved in an alcohol [8]. Different stabilizing agents have been used for the formation of WO_3 films, such as ***bulky alcohols*** (e.g. substituting ethanol with propanol or amyl alcohol), ***metal chloride alkoxides*** (e.g. $WCl_3(OEt)_2$) or ***bidentate ligands*** (e.g. carboxylates, β-diketonates) [7, 9].

Generally, the chelating ligands possess a negative partial charge during complexation which renders them inactive during hydrolysis (bad leaving groups) while they depart during condensation [7]. In that way, colloidal solutions remain stable and suitable for coating processes [7].

Additionally, solid chemically modified precursors could be rendered suitable for coating applications, by re-dispersing or dissolving them in the desired medium (water, ethanol etc.).

In other cases, chelating agents could also act as porogens upon their degradation [10], a structural property which is very beneficial for numerous applications as it was discussed in the introduction.

2.1.1 Peroxo- tungsten ions in solutions

Hydrogen peroxide (***H_2O_2***) (peroxy ions (O_2^{2-})) is a common strong chelating agent especially in aqueous solutions, which increases the coordination number of the metal and its partial positive charge. In that way tungsten becomes more attractive towards the nucleophilic attack of water molecules while it remains inactive towards hydrolysis [7].

Usually, the synthesis of the peroxotungstic acid is taking place by mixing metallic tungsten, tungsten carbide or tungstic acid with a solution of hydrogen peroxide [8, 9, 11]. When hydrogen peroxide is in excess, the solution remains stable for several months [8]. Heating or dipping a platinum net into the solution leads to the decomposition of the excess H_2O_2 [12]. This step is necessary, in order to avoid the production of uncontrolled byproducts.

There are different peroxotungstic compounds according to the W/H_2O_2 ratio in the solution, the pH etc. [9, 13, 14]. For example, dimeric species $[W_2O_3(O_2)_4(H_2O)_2]^{2-}$ are easily formed in acidic solutions (see Figure 2.1 a) where the two tungsten atoms are surrounded by two corner-linked pentagonal bipyramids [9, 12, 13, 15]. Kim et al. [15] proposed a chemical reaction for the complexation of peroxide in the coordination sphere of W:

$$2W(s) + 10H_2O_2 \longrightarrow [W_2O_3(O_2)_4(H_2O)_2]^{2-} + 2H_3O^+ + 5H_2O$$

Pecquenard et al. [12] based on ^{183}WNMR identified another anion in equilibrium with the aforementioned dimer, the $[WO_2(O_2)_2]^{2-}$ which according to L. Barrio et al. [13] is present when W and H_2O_2 concentrations are below 0.2M. Other peroxo ions have also been reported in the literature such as $[W_4O_9(O_2)_4(H_2O)_2]^{2-}$, $[W_7O_{23}(O_2)]^{6-}$ and $[W_7O_{22}(O_2)]^{6-}$ [15]. The last two anions have been observed under acidic conditions (pH<4) and at H_2O_2/W<1, when cathodic electrodeposition was employed [15]. When the concentration of the H_2O_2 is maintained low, more condensed species are formed including the well-known $[W_{12}O_{42}H_2]^{10-}$ [9, 13] or $[W_{12}O_{38}(O_2)_6]^{16-}$ [11]. These anions, adopt the paratungstate structure which is presented in Figure 2.1 b. However, in this case, some octahedra are replaced with pentagonal bipyramids in order to introduce the peroxide groups (Figure 2.1 b) [11].

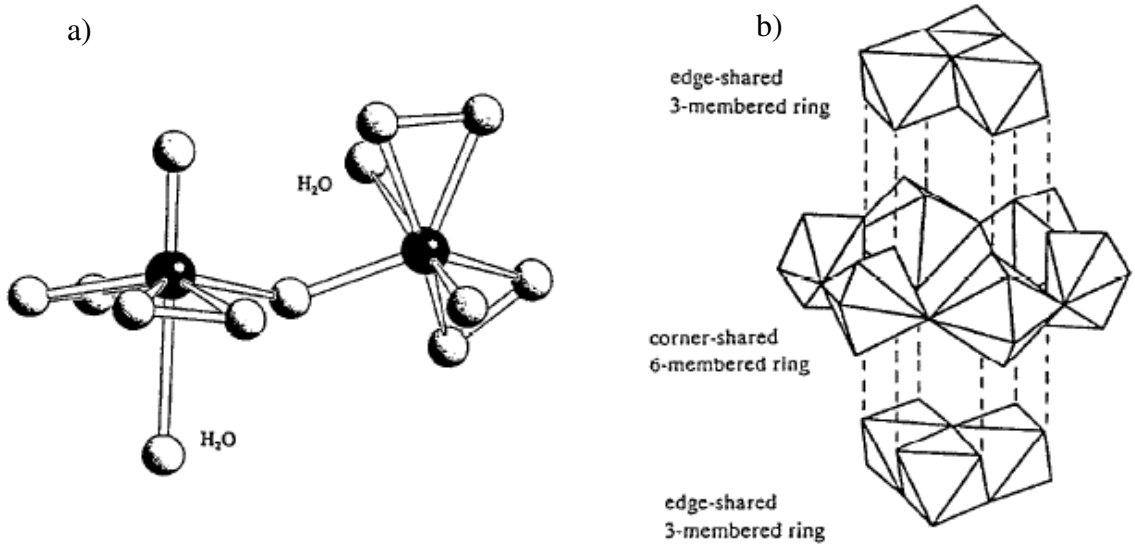

Figure 2.1 [9]: Structural models for a) $[W_2O_3(O_2)_4(H_2O)_2]^{2-}$ and b) $[W_{12}O_{42}H_2]^{10-}$

2.1.2 Peroxopolytungstic acids

The nature of the ***dried*** product is very sensitive to the different experimental conditions such as the ratio of W/H_2O_2 [9, 14] or the evaporation rate during the drying process [8, 12]. For this reason there is a vast number of different peroxo-tungsten products reported in the literature produced at different experimental conditions [8, 12, 16].

For example, according to J. Livage et al. [9] a yellow glassy solid is produced with the general formula $12WO_3{:}7H_2O_2{:}20H_2O$ after the evaporation of the solution (no further information regarding the experimental conditions were given). Drying the solution at 100ºC for 1h resulted in the formation of $WO_3.2H_2O$. On the other hand, Chen and Lin [16] based on thermogravimetric analysis and iodometric titration reported the formation of a solid with the empirical formula $H_2WO_{3.1}(O_2)_{0.9}.1.4H_2O$ when the solution was dried at 40-45ºC. IR spectroscopy revealed that this precursor was comprised by W-OH bonds, hydrogen bonded H_2O, W-O-O-W and W-O-W bonds (see Figure 2.2a and Table 2.1). This precursor was also mixed with an aqueous PVP solution and remained stable for a long period of time.

Pecquenard et al. [8, 12] pointed out the importance of the ***evaporation rate*** on the resulting product (in reference [8] the study was conducted on films). They stated that ***slow evaporation*** at room temperature leads to the production of a crystalline phase. Based on thermal analysis and X-ray diffraction they concluded that the crystalline phase was $[WO_2(O_2)H_2O].nH_2O$ where $1 \leq n \leq 2$ [12] (in some other publications [8, 14] the same product is depicted as $WO_3.H_2O_2.H_2O$ for n=1).

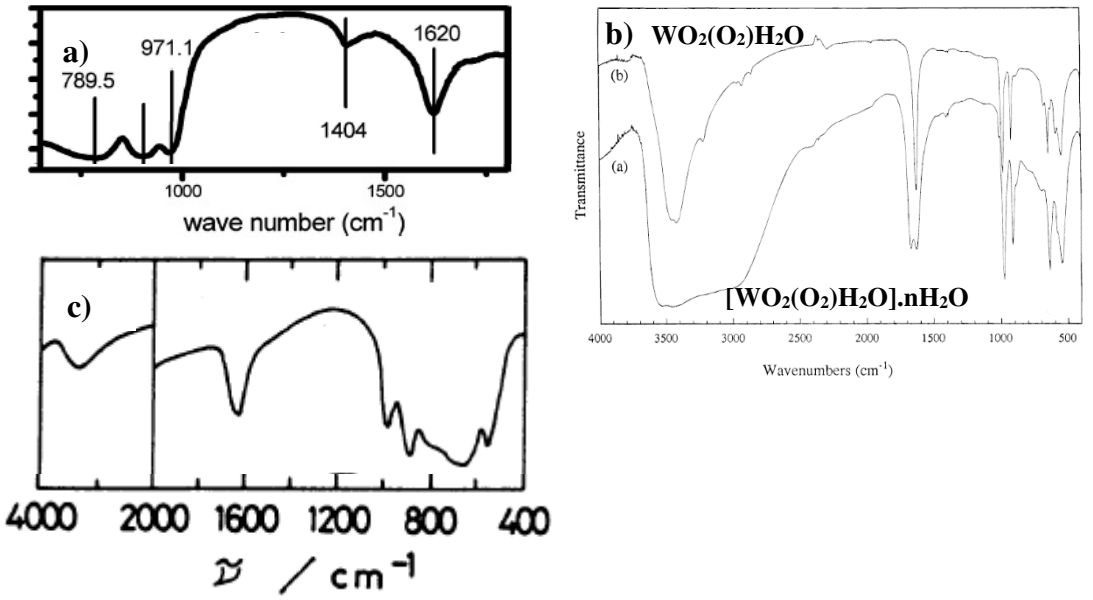

Figure 2.2: Infrared spectra of a) $H_2WO_{3.1}(O_2)_{0.9}.1.4H_2O$ [16] b) $[WO_2(O_2)H_2O].nH_2O$ and $(WO_2(O_2)H_2O)$ [12] and c) amorphous peroxo-tungsten precursor [14]

Further heating at 120°C resulted in the slight dehydration of the solid, obtaining $(WO_2(O_2)H_2O)$ (according to reference [12]) and $WO_3{:}H_2O_2{:}0.14H_2O$ (according to reference [8]). In Figure 2.2 b and Table 2.1 the infrared spectra of the two solids ($[WO_2(O_2)H_2O].nH_2O$ and $WO_2(O_2)H_2O$ from reference [12] are presented. Based on their studies the authors designed the structures of the two phases which are illustrated in Figure 2.3. These structures are comprised by layers of W octahedra where one corner in an equatorial position is occupied by the peroxo group. The axial positions are occupied by one water molecule and a double-bonded oxygen. The octahedra are linked together by sharing edges. The X-ray diffractograms of different crystalline peroxopolytungstic acids are displayed in Figure 2.4. It should be stressed out that in some publications peroxo-groups could be sustainable up to ~120°C [8]. However, in the experiments of Nanba et al. [11] peroxo- groups were present only in the as-prepared solid. By annealing the precipitate at 100°C for 1h the peroxo groups were already decomposed. Generally, TGA (thermogravimetric analysis) and X-ray measurements depicted that peroxide is decomposed between 100-120°C [8, 15].

On the other hand, ***fast evaporation*** at room temperature under a stream of air (or at 100°C) leads to **amorphous solids** with the general formula $WO_3.xH_2O_2.yH_2O$ where $0.05 \leq x \leq 1$ and $3 \leq y \leq 4$ [8, 12]. However, fast evaporation possesses the risk of precipitating the insoluble tungstic acid [15, 17]. For this reason, M.Giannouli and G. Leftheriotis [17] invented a new methodology to produce peroxo tungsten complexes stabilized in their solution. More precisely, after mixing W with a H_2O_2 solution, they placed the mixture in the fridge (2°C) and let W to dissolve for 7 days. Then, in order to eliminate the excess of peroxide, they let the solution in the fridge for 5 more days. This method impeded the precipitation of any kind of solid but it was very time consuming.

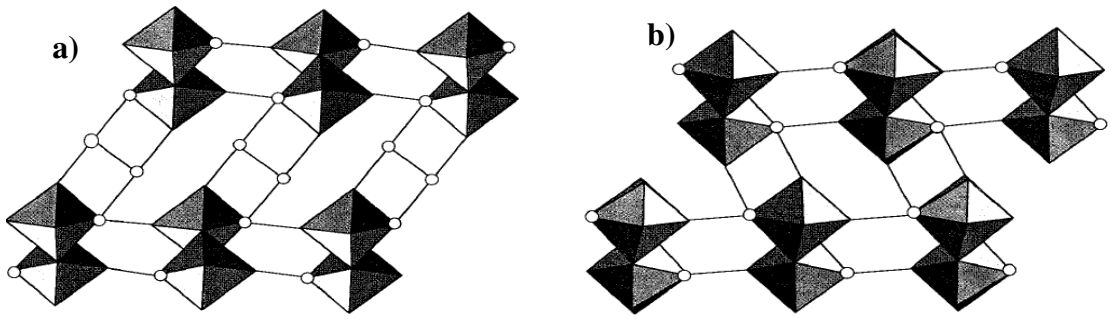

Figure 2.3 [12]: a) $[WO_2(O_2)H_2O].nH_2O$ and b) $WO_2(O_2)H_2O$. The circles correspond to water molecules

Kim et al. [15] investigated the influence of the evaporation under three different atmospheres (hot plate evaporation, N_2 bubbling and rotary evaporation) on the structure of the resulting precipitate. The chemical formulas they suggested based on iodometric titration method was $WO_3:0.13H_2O_2:10H_2O$, $WO_3:0.16H_2O_2:7.1H_2O$, $WO_3:0.15H_2O_2:3H_2O$ respectively. The slowest process (hot plate) resulted in the lowest H_2O_2 content but in the highest water content.

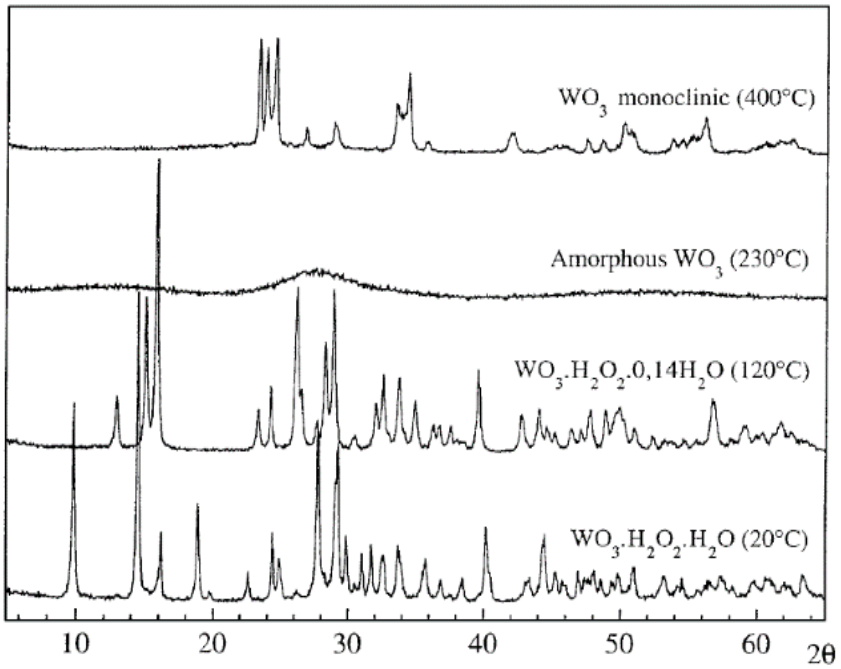

Figure 2.4 [8]: X-ray diffractograms of $WO_3.H_2O_2.H_2O$, $WO_3.H_2O_2.0.14H_2O$ an amorphous product which is obtained at 230°C and monoclinic WO_3. The X-ray diffractograms of the –peroxo complexes are identical to the $[WO_2(O_2)H_2O].nH_2O$ and $WO_2(O_2)H_2O$ in reference [12] respectively

Table 2.1: Assignment of infrared bands for different peroxo-compounds

Corresponding bond	$H_2WO_{3.1}(O_2)_{0.9}.1.4H_2O$ (cm^{-1})	$[WO_2(O_2)H_2O].nH_2O$ (cm^{-1})	$WO_2(O_2)H_2O$ (cm^{-1})	$WO_3.xH_2O_2.yH_2O$ (amorphous) (cm^{-1})	Ref.
H_2O (antisymmetric mode)	N.A	wide peak from 2500-3600	3450	~2000-4000	[12, 16, 18]
H_2O (symmetric mode)	N.A		3405		[12, 18]
H---O-H_2 (bending mode)	1620	double peak at around 1600	1620	~1600	[11, 16, 18]
W-OH	1404				[16]
W-O-O-W (stretching mode)	971.1				[16]
W=O (symmetric mode)		968	968	943	[11, 12]
O-O		903	903	886	[12]
W-O-W (antisymmetric mode)	789.5	650	650	629	[11, 12, 16]
$W(O_2)$ (antisymmetric mode)		540	540	543	[11, 12]

Okamoto et al. [14] emphasized on the role of W/H_2O_2 ratio on the crystalline and stoichiometric phase of the peroxotungstic acids.

Their experiments revealed that when H_2O_2 in the initial solution was high ($H_2O_2/W>1$) then crystalline precipitates were emerging. Despite the initial concentrations in the solutions, the concentration of H_2O_2 in these solids was always at around 3.4 $mmol.g^{-1}$ (determined by titration with $KMnO_4$ solution). These precipitates were insoluble in water or in peroxide solutions and they were characterized with the general formula of $WO_3.xH_2O_2.H_2O$ where x=1 (same as in reference [12]).

On the other hand, when the H_2O_2/W in the solution was approximating 1 (and below) then amorphous compounds were emerging ($1<x<0$ and $1.5<y<3$). The authors [14] also concluded that when x was $1>x>0.53$ then the compound was water soluble while when x was $0.53\geq x>0$ then the precipitate was insoluble. In Figure 2.2 c the infrared spectrum of an amorphous precursor is presented. Even though the spectrum resembles a lot to the rest of the spectra in Figure 2.2 the peaks are wider as a result of its amorphous nature.

2.2 Synthesis of the peroxo tungstic acid precursor (PTA)

As it was shown in the previous paragraphs, the preparation of a peroxo-tungsten precursor is difficult, mainly because of a large product diversity and the risk of tungstic acid precipitation [15]. As it will be shown in the experimental part of this chapter, one of the initial challenges in this PhD was to obtain a soluble peroxo-tungstic acid solid precursor (PTA, $WO_3:xH_2O_2:yH_2O$ where $1>x>0.53$ according to [14]) suitable for coating solutions. However, its synthesis has proved to be difficult, not reproducible and the information drawn from the literature were sometimes confusing and misleading.

2.2.1 Experimental part

The synthesis was based on the publication of Wang et al. [19]. Specifically, 5.0g of H_2WO_4 powder (Research org/inorg chem corp. 99.5%) were dispersed in 86 g of mQ water. In this mixture, 33g of H_2O_2 30 wt% (Merck) were added. The reaction was magnetically stirred at 40°C overnight to produce a colorless solution. PTA powder was obtained by drying the clear solution at 40°C in an oven.

Despite the numerous efforts (see Table 2.2 below) we couldn't finally synthesize a soluble PTA precursor in ethanol or water and therefore no films were produced with the use of the aforementioned precursor. Every time, yellow or white insoluble solids were emerging depending on their consistency. In the work of Wang et al. [19-21] a pale yellow PTA powder was repeatedly produced (the consistency was not defined) which was further used in the coating solutions for the production of mesoporous WO_3 films.

We performed X-ray diffraction on a Powder diffractometer (Siemens D5000) (CuKalpha radiation), a 2-theta range from 10° to 70°, a step size of 0.04° and a scan speed of 1.5 s/step.

IR spectra were recorded in transmission mode with a Bruker Equinox 55 FTIR instrument. Pellets of ~20 mg of sample mixed with ~300 mg of KBr were used for the acquisition of the infrared spectra. A pure KBr pellet was used as a reference.

Table 2.2: Experimental efforts to prepare PTA

Trial	Variable	Result	Observations
1	none	White insoluble powder	1) H_2WO_4 was never completely dissolved in the H_2O_2 solution 2) 3 days needed to completely evaporate the solvent in a high stream of air 3) Solution (just before the complete evaporation) was very acidic (pH~0)
2	no stream of air during drying	Pale yellow insoluble powder	7 days to dry the solid out
3	Dispersion of H_2WO_4 at 60°C	Pale yellow insoluble powder	1) During dissolution a yellow cloudy mixture appeared 2) 6 days needed to dry the solid out
4	1) New batch of H_2O_2 (30%) 2) Centrifuge to remove the insoluble part before drying 3) Drying on the hotplate at 40°C (use of an oilbath)	Yellow and orange insoluble precipitates	5 days needed to dry the solid out
5	1) Direct dissolution of 3.2g of H_2WO_4 in 50g of H_2O_2 30% 2) Centrifuge to remove the insoluble part before drying 3) Dissolution at 50°C	Yellow insoluble precipitate	6 days needed to dry the solid out
6	1) New H_2WO_4[1](Aldrich) 2) Same composition as in 5 3) Vacuum oven at 40°C	White to yellow powder with shiny facets	2 days needed to dry the solid out
7	Same conditions as 6 but precipitation of a white solid	Insoluble solid	1) effort to stabilize the remaining solution with Brij-56 ➔ failed (precipitate)
8	Replication of 6	Yellow insoluble crystal-like solid	

[1] Different characterization techniques were used in order to assess the quality of H_2WO_4 in terms of contamination (SEM (data not shown), EDX ((data not shown), FTIR) in order to explain the difficulty to dissolve it in the peroxide solution, but nothing unusual was observed

2.2.2 Results and discussion

As it is straightforward from paragraph 2.2.1, the synthesis of a suitable PTA precursor for coating solutions was rendered impossible. The results were incoherent, inconclusive and not reproducible. This is verified with the infrared spectra and the powder X-ray diffractograms in Figure 2.5. Trial 1 and 6 display similar infrared spectra with well-

resolved narrow peaks implying their crystalline nature. These spectra also resemble to the ones in Figure 2.2 b which belong to $[WO_2(O_2)H_2O].nH_2O$ and $WO_2(O_2)H_2O$. However, even though trial 8 was a replica of trial 6, it doesn't possess the same infrared spectrum. The FTIR in trial 8 exhibits wide unresolved peaks unlike the one in trial 6. This is a direct evidence of the non-reproducible synthetic route. On the other hand trials 4 and 5 give amorphous significantly less hydrated products compared to the rests (lack of the peaks at 1600 cm^{-1} or at 2000-3000 cm^{-1}). These complexes are much more polymerized than the initial H_2WO_4 considering the lack of the W=O (~950 cm^{-1}). When the X-ray diffractogram of the product (trial 5) was acquired, it appeared that the solid was comprised by two mixed crystalline hydrated oxides with orthorhombic phases ($WO_3.0.33H_2O$ and $WO_3.H_2O$). Most probably these two phases co-exist with other amorphous products (inferred by the wide peaks in the infrared spectrum and in the X-ray diffractogram).

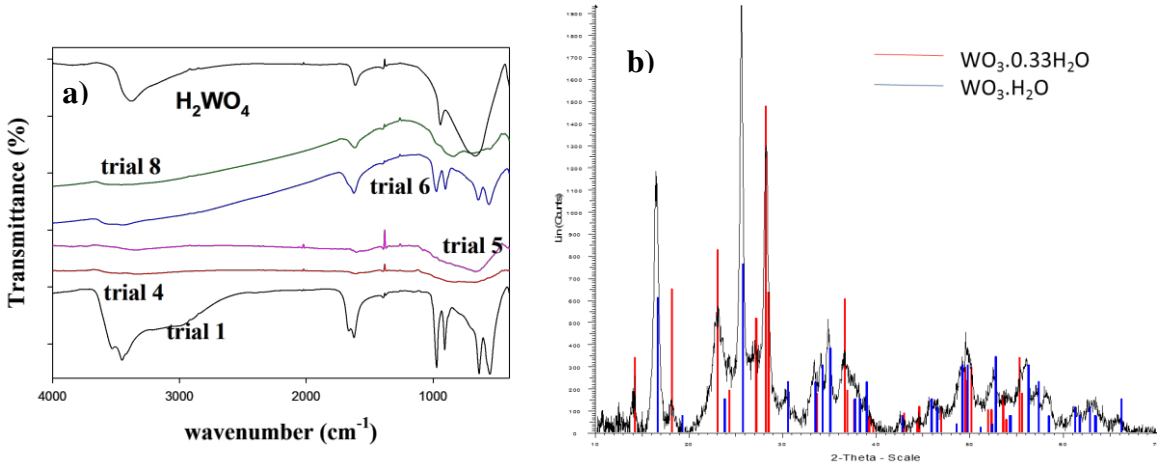

Figure 2.5: a) Infrared spectra of different trials described in Table 2.3. The commercial H_2WO_4 (starting material from Aldrich) is displayed as a comparison b) Powder X-ray diffraction of the solid derived from trial 5. References: red: 00-054-1012 and blue: 00-043-0679

2.3 Acetylated peroxotungstic acid precursor (APTA)

Since the synthesis of peroxotungstic precursor appeared to be difficult, we decided to proceed with another derivative, the so-called acetylated peroxotungstic acid (APTA). The addition of acetic acid provides stabilization as it acts as a chelating ligand for many metals such as Mo, Ti, Zr, W etc [7, 22] . On the other hand, it could also lead to the acceleration of the gelation process in some cases (e.g. $Si(OR)_4$) since it can behave as an acid catalyst as well [7]. It should be mentioned that the literature regarding the structural characterization of the APTA is significantly limited compared to PTA precursor and no efforts to build a structural model or a suggested empirical formula was found in the literature.

The acetate ions can coordinate with the metal in different ways as it is presented in Figure 2.6.

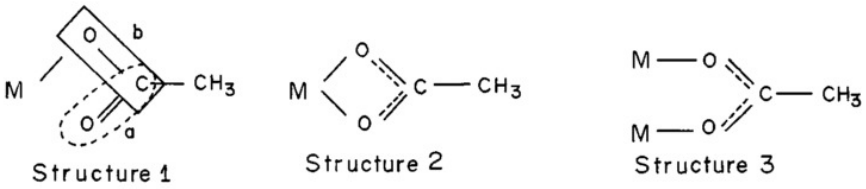

Figure 2.6 [23]: Different ways that acetic acid can coordinate with the metal

The coordination mode of the acetic acid with the metal can also be determined from the infrared spectra of the corresponding precursors [23, 24] according to the shifts of the –COO groups frequencies compared to the free acetate (see Figure 2.7 and Table 2.3).

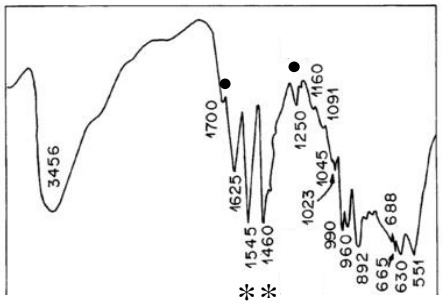

Coordination mode of acetate ion	ν(C – O) or $\nu_{symm}(COO^-)$ (cm^{-1})	ν(C=O) or $\nu_{asymm}(COO^-)$ (cm^{-1})	$\Delta\nu$ (cm^{-1})
Free acetate	1416	1560	144
Bidentate	1460	1545	105
Monodentate	1250	1700	450

Figure 2.7 [23, 24]: FTIR spectrum of the APTA precursor along with the positions of C-O and C=O bands in free, mono- and bidentate coordination modes of acetate ions. The asterisks on the IR spectrum are referring to the bidentate mode and the bullets to the monodentate coordination

The shifts are determined by the delocalization of the π electrons in the bi-dentate mode and the subsequent modifications when the oxygens are reacting with the metal [23, 24] in each case. From the FTIR spectrum in Figure 2.7 it is evident that acetic acid is predominantly in the bidentate mode rather than monodentate.

Table 2.3: Bands assignment in the APTA complex

Corresponding bond[1]	APTA (cm^{-1})	Ref.
H_2O (anti)symmetric mode, vsym/vasym)	3456	[23, 24]
vasym(COO)mono	1700	[23, 24]
δ(H_2O)	1625	[23, 24]
vasym(COO)bi	1545	[23, 24]
vsym(COO)bi	1460	[23, 24]
δ(CH_3)	1437,1415	[23, 24]
vsym(COO)mono	1250	[23, 24]
v(W-O-C)	1160, 1091	[23, 24]
ρr(CH_3)	1023,1045	[23, 24]
v(W=O)	990,960	[23, 24]
v(O-O)	892	[23-25]
vasym(O-W-O), (CH), (COO), δ(O-C=O)	688, 665, 630	[23-25]
v(WO_2)	551	[23-25]

[1] where v = stretching mode, δ = bending mode, ρr = rocking mode, mono/bi = mono/bi-dentate

It is also important to note that APTA possesses a low degree of polymerization (as expected) which is also evident from the FTIR spectrum (two different peaks of terminal W=O bonds are well apparent). Moreover, this precursor is well hydrated, as deduced by the wide peak at around 3500 cm^{-1} and the sharp peak at 1620 cm^{-1}.

Based on FTIR spectra and thermogravimetric/differential thermal analysis the more distinctive changes during thermal treatment occur up to 200ºC. The complexed acetic acid decomposes at ~200ºC [25].

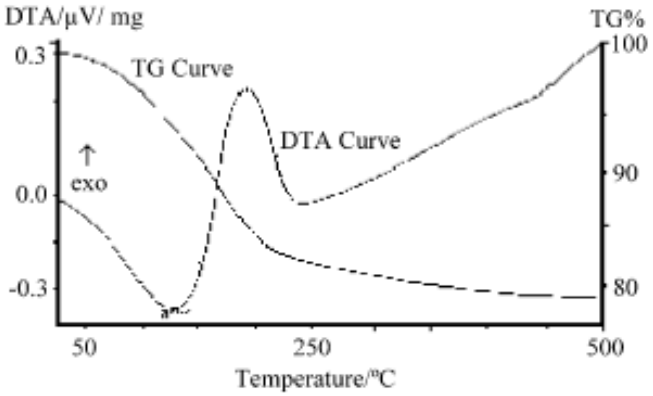

Figure 2.8[25]: TG and DTA plots of the APTA precursor

2.3.1 Experimental part

The synthesis of APTA was based on the work of N. Sharma et al. [24] and N. R. Denny [22]. More specifically, a 150mL flask containing 40mL of hydrogen peroxide (29.0-31.0%, Merck) and 4mL of milliQ water was placed in an ice-bath and 6.5g of W powder (particle size 12µm, 99.9%, Aldrich) were added in small lots. The mixture was stirred at low temperature for about 30 min. After the ice-bath was removed, a condenser was placed at the top of the flask and the mixture was allowed to stir overnight at room temperature until all W was dissolved. Then, 40mL of glacial acetic acid were added (Mobi-lab & Labotec) and the solution was heated at 55ºC for 3h. The yellowish powder (~7g) was recovered by evaporating the solvents in the rotary evaporator at a temperature of 55-60ºC [22].

FTIR set-up was already described in paragraph 2.2.1. For the characterization of this precursor two more techniques were used: TGA-DSC (ThermoGravimetric Analysis and Diferential Scanning Analysis) and SEM (Scanning Electron Microscopy).

The thermal analysis measurements were conducted on a Netzsch STA 449C instrument under air and a temperature rate of 10 K/min.

SEM micrographs were acquired on a FEG- ESEM XL30, 15kV, FEI microscope.

2.3.2 Results and discussion

In Figure 2.9 the FTIR of the APTA precursor is presented. This spectrum resembles a lot with the one presented in Figure 2.7 (it contains the peaks corresponding to acetate and

peroxide vibrations), but it resembles more with the FTIR of the APTA precursor prepared from Na_2WO_4 (Figure 2.9 b), synthesized by the same authors. One of the most noticeable differences is the lack of the monodentate acetate ligand. The authors did not explain the subtle structural differences between the products of the two processes. We believe that these differences emerge from the solvent's evaporation rate (in the publication it wasn't mentioned for example which vacuum technique they used, e.g. vacuum oven, rotary evaporator etc.), the duration of the reflux, or the temperature during solvent's evaporation. Figure 2.9 c corroborates with these assumptions. By evaporating the solvent at lower temperature (40°C), both monodentate and bidentate acetate chelating were maintained. However, it appears that the material is somewhat less hydrated due to the extended evaporation. Nevertheless, the APTA precursor is soluble in both water and ethanol and it is therefore suitable for WO_3 coatings, as it will be discussed in the next chapters.

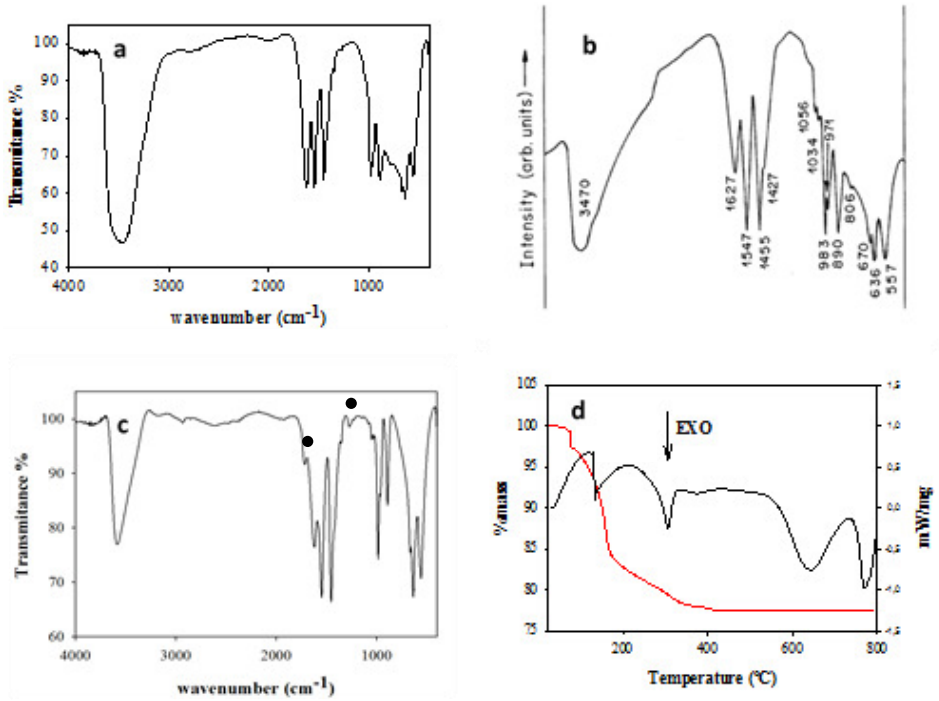

Figure 2.9: a) FTIR spectrum of APTA synthesized in our laboratory b) FTIR spectrum of APTA synthesized by the group of N. Sharma et al. [24] using acidified Na_2WO_4 as a precursor c) APTA precursor synthesized in our laboratory and evaporated at 40°C instead of 55-60°C and d) TG and DSC measurements of APTA

The TG/DSC thermal measurements presented in Figure 2.9 are not consistent with the one presented in Figure 2.8. In our case, the mass loss occurs in the range of 70-400°C with endothermic and exothermic overlapping phenomena taking place. At low temperature (100-130°C), these phenomena are constituted by the evaporation of physisorbed water and the evaporation/decomposition of peroxo and acetate groups [26, 27]. At higher temperature (130-400°C) the condensation reactions between the W-OH groups might be responsible for the exothermic peak at 130°C and the following endothermic peak which might be attributed to the evaporation of the produced water and the structural water [26, 27]. The exothermic peak at 307°C might be associated with further condensation and the

initiation of crystallization. The other two exothermic peaks at very high temperatures (640ºC and 770ºC), correspond either to the conversion into other (presumably more symmetric) crystalline phases [28-30] such as orthorhombic and tetragonal or to the solid's fusion. Based on the TG plot, almost 23% of the initial precursor mass consisted of water, peroxo and acetate groups.

The SEM micrograph in Figure 2.10 a reveals that the typical synthesis of the precursor leads to a powder with a rough surface. By refluxing the precursor for a longer period of time (e.g for 6 hours, Figure 2.10 b) a powder with a smoother surface is obtained. Similar results were emerged by refluxing the precursor for 12 and 24 hours (data not shown).

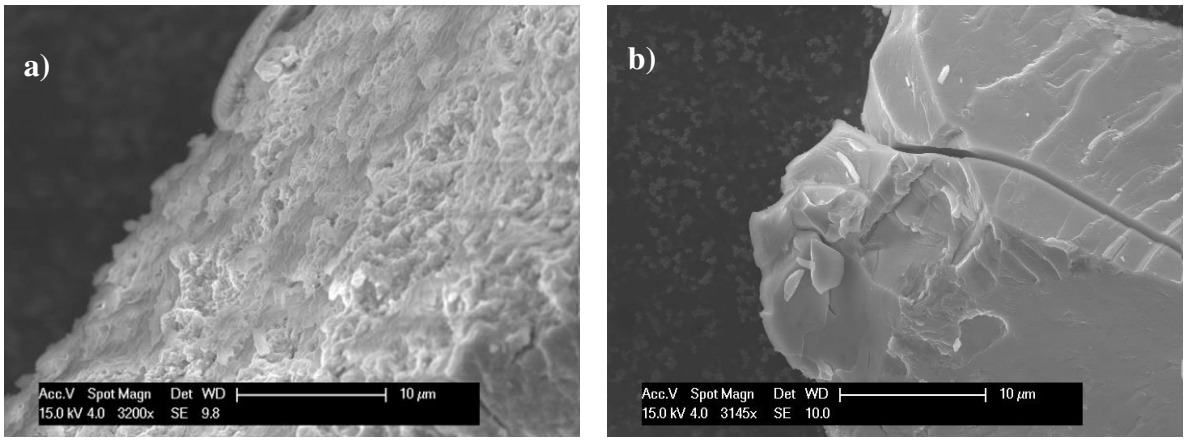

Figure 2.10: SEM micrographs of the precursor a) refluxed for 3h b) refluxed for 6h

2.4 Conclusions

This chapter describes all the efforts which were realized in this PhD in order to synthesize PTA and APTA precursors for coating purposes. Despite all the trials we couldn't finally synthesize a soluble PTA precursor (WO_3:xH_2O_2:yH_2O) suitable for coating solutions. There were practical difficulties to conduct the experiments (reactants solubility constraints, high dependence on the evaporation rate, precipitation of tungstic acid etc.). Moreover, the products were insoluble in water and ethanol and not-reproducible.

For this reason, we implemented the synthesis of the acetylated peroxo tungstic acid derivative (APTA). The addition of acetic acid provides stabilization as it acts as a chelating ligand [7, 22]. Due to the presence of acetic acid, the APTA precursor is much less polymerized and therefore it is easily soluble in aqueous and ethanolic solutions. This precursor was used in the coating solutions throughout this PhD for the formation of mesoporous and dense WO_3 films.

2.5 References for Chapter 2

[1] J. Livage, D. Ganguli, Sol-gel electrochromic coatings and devices: A review, Solar Energy Materials & Solar Cells, 68 (2001) 365-381.

[2] R. Solarska, B.D. Alexander, J. Augustynski, Electrochromic and photoelectrochemical characteristics of nanostructured WO3 films prepared by a sol-gel method, C. R. Chim., 9 (2006) 301-306.

[3] L.H.M. Krings, W. Talen, Wet chemical preparation and characterization of electrochromic WO3, Solar Energy Materials and Solar Cells, 54 (1998) 27-37.

[4] O. Pyper, A. Kaschner, C. Thomsen, In situ Raman spectroscopy of the electrochemical reduction of WO3 thin films in various electrolytes, Solar Energy Materials and Solar Cells, 71 (2002) 511-522.

[5] S. Badilescu, P.V. Ashrit, Study of sol-gel prepared nanostructured WO3 thin films and composites for electrochromic applications, Solid State Ionics, 158 (2003) 187-197.

[6] V. Srivastava, A.K. Srivastava, K.N. Sood, K. Jain, Sol gel synthesis of tungsten oxide thin film in presence of surfactant for NO2 detection, Sensors & Transducers Journal, 107 (2009) 99-110.

[7] J. Livage, M. Henry, C. Sanchez, Sol-gel chemistry of transition metal oxides, Progress in Solid State Chemistry, 18 (1988) 259-341.

[8] B. Pecquenard, H. Lecacheux, S. Castro-Garcia, J. Livage, Electrochromic Properties of Peroxopolytungstic Acid Thin Films, Journal of Sol-Gel Science and Technology, 13 (1998) 923-927.

[9] J. Livage, G. Guzman, Aqueous precursors for electrochromic tungsten oxide hydrates, Solid State Ionics, 84 (1996) 205-211.

[10] H.M.A. Soliman, A.B. Kashyout, M.S. El Nouby, A.M. Abosehly, Effect of hydrogen peroxide and oxalic acid on electrochromic nanostructured tungsten oxide thin films, International Journal of Electrochemical Science, 7 (2012) 258-271.

[11] T. Nanba, S. Takano, I. Yasui, T. Kudo, Structural study of peroxopolytungstic acid prepared from metallic tungsten and hydrogen peroxide, Journal of Solid State Chemistry, 90 (1991) 47-53.

[12] B. Pecquenard, S. Castro-Garcia, J. Livage, P.Y. Zavalij, M.S. Whittingham, R. Thouvenot, Structure of Hydrated Tungsten Peroxides $[WO_2(O_2)H_2O]\cdot nH_2O$, Chemistry of Materials, 10 (1998) 1882-1888.

[13] L. Barrio, J.M. Campos-Martín, J.L.G. Fierro, Spectroscopic and DFT Study of Tungstic Acid Peroxocomplexes, The Journal of Physical Chemistry A, 111 (2007) 2166-2171.

[14] H. Okamoto, A. Ishikawa, T. Kudo, Amorphous and Crystalline Peroxopolytungstic Acids Formed from Tungsten and Hydrogen Peroxide, Bulletin of the Chemical Society of Japan, 62 (1989) 2723-2724.

[15] C.-Y. Kim, M. Lee, S.-H. Huh, E.-K. Kim, WO_3 thin film coating from H_2O-controlled peroxotungstic acid and its electrochromic properties, Journal of Sol-Gel Science and Technology, 53 (2010) 176-183.

[16] X. Chen, Y. Lin, Photochromism of Peroxotungstic Acid/PVP Nanocomposite Obtained by Sol-Gel Method, J. Sol-Gel Sci. Technol., 36 (2005) 197-201.

[17] M. Giannouli, G. Leftheriotis, The effect of precursor aging on the morphology and electrochromic performance of electrodeposited tungsten oxide films, Solar Energy Materials and Solar Cells, 95 (2011) 1932-1939.

[18] M.F. Daniel, B. Desbat, J.C. Lassegues, B. Gerand, M. Figlarz, Infrared and Raman study of WO3 tungsten trioxides and $WO_3.xH_2O$ tungsten trioxide tydrates, Journal of Solid State Chemistry, 67 (1987) 235-247.

[19] W. Wang, Y. Pang, S.N.B. Hodgson, On key factors for the fabrication of mesoporous tungsten oxide films from tungstic acid, Journal of Sol-Gel Science and Technology, 58 (2010) 135-141.

[20] W. Wang, Y. Pang, S.N.B. Hodgson, Preparation, characterisation and electrochromic property of mesostructured tungsten oxide films via a surfactant templated sol–gel process from tungstic acid, Journal of Sol-Gel Science and Technology, 54 (2010) 19-28.

[21] W. Wang, Y. Pang, S.N.B. Hodgson, XRD studies of thermally stable mesoporous tungsten oxide synthesised by a templated sol–gel process from tungstic acid precursor, Microporous and Mesoporous Materials, 121 (2009) 121-128.

[22] N.R. Denny, F. Li, D.J. Norris, A. Stein, In situ high temperature TEM analysis of sintering in nanostructured tungsten and tungsten-molybdenum alloy photonic crystals, Journal of Materials Chemistry, 20 (2010) 1538-1545.

[23] M. Deepa, N. Sharma, P. Varshney, S.P. Varma, S.A. Agnihotry, FTIR investigations of solid precursor materials for sol-gel deposition of WO_3 based electrochromic films, Journal of Materials Science, 35 (2000) 5313-5318.

[24] N. Sharma, M. Deepa, P. Varshney, S.A. Agnihotry, FTIR and absorption edge studies on tungsten oxide based precursor materials synthesized by sol–gel technique, Journal of Non-Crystalline Solids, 306 (2002) 129-137.

[25] A. Patra, K. Auddy, D. Ganguli, J. Livage, P.K. Biswas, Sol–gel electrochromic WO_3 coatings on glass, Materials Letters, 58 (2004) 1059-1063.

[26] M. Deepa, T.K. Saxena, D.P. Singh, K.N. Sood, S.A. Agnihotry, Spin coated versus dip coated electrochromic tungsten oxide films: Structure, morphology, optical and electrochemical properties, Electrochim. Acta, 51 (2006) 1974-1989.

[27] M. Deepa, A.G. Joshi, A.K. Srivastava, S.M. Shivaprasad, S.A. Agnihotry, Electrochromic Nanostructured Tungsten Oxide Films by Sol-gel: Structure and Intercalation Properties, Journal of the Electrochemical Society, 153 (2006) C365-C376.

[28] H. Zheng, J.Z. Ou, M.S. Strano, R.B. Kaner, A. Mitchell, K. Kalantar-zadeh, Nanostructured Tungsten Oxide – Properties, Synthesis, and Applications, Advanced Functional Materials, 21 (2011) 2175-2196.

[29] J.-H. Choy, Y.-I. Kim, J.-B. Yoon, S.-H. Choy, Temperature-dependent structural evolution and electrochromic properties of peroxopolytungstic acid, J. Mater. Chem., 11 (2001) 1506-1513.

[30] D. Isik, M. Ak, C. Durucan, Structural, electrochemical and optical comparisons of tungsten oxide coatings derived from tungsten powder-based sols, Thin Solid Films, 518 (2009) 104-111.

Chapter 3
Mesoporous WO_3 films by dip-coating

3.1 Literature review about templated-assisted dip-coating

In dip-coating, a substrate is dipped in a solution containing the desired reactants including the sol-gel precursor and a volatile solvent (Figure 3.1). Upon withdrawal (at a constant speed) the outer part of the liquid entrained by the substrate returns back to the solution. The solvent in the remaining layer starts to evaporate resulting in a drying line [2]. During this process, concentration gradients are induced and the layer is enriched with metal oxide oligomers. In dip-coating, the thickness of the films can be predicted with the Landau and Levich equation [2]:

$$h = \frac{0.94\ (\eta.v)^{\frac{2}{3}}}{\gamma_{LV}^{\frac{1}{6}}(\rho g)^{\frac{1}{2}}}$$

where h is the thickness of the films, η solution viscosity, v withdrawal rate, γ_{LV} the surface tension at the liquid-vapour interface, ρ the solution density and g the gravitational acceleration. The above equation illustrates that as the withdrawal rate increases the film thickness increases as well. This dependence can be associated with the increase of viscosity at higher shear stress when the substrate is pulled out of the solution. This effect counteracts the natural gravity-induced which draws the liquid back to the solution [6].

For the formation of mesoporous films, a structure-directing agent is needed (surfactant) and EISA (Evaporation Induced Self-Assembly) is employed. In this case, during evaporation the concentration of the surfactant increases as well and when it exceeds its critical micelle concentration micelles begin to form (Figure 3.2). After the drying line, a modulable steady state (MSS) occurs where the mesostructure can be modulated by varying the relative humidity (RH%) [8].

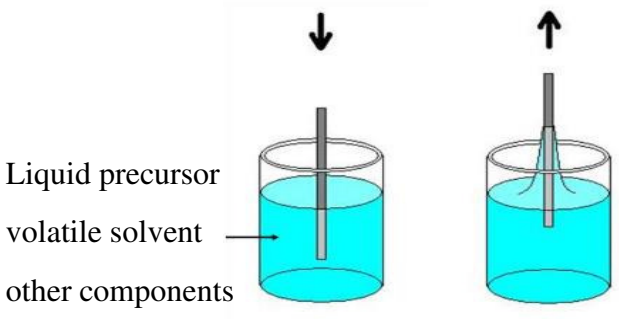

Figure 3.1 [10]: Dip-coating process scheme

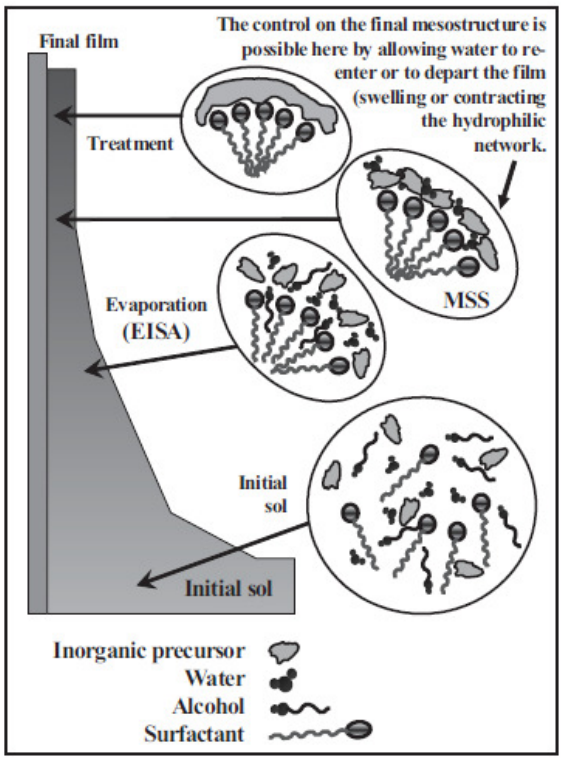

Figure 3.2 [8]: Mesostructured thin film formation by dip-coating

According to D. Grosso et al. [2] who studied the CTAB/$SiO_{1.25}(OH)_{1.5}$ system, at low ratios and high RH% more curved mesostructures are favored such as 2D hexagonal structures while at dry conditions lamellar architectures are obtained. Apart from relative humidity other factors influence the architecture of the final mesostructure such as the relative amounts of the inorganic precursor and surfactant, pH, hydrolysis ratio, nature of the surfactant (surfactant geometry) and the precursor, etc. [2].

Generally the prediction of the mesostructure is difficult and the formation of an ordered architecture relies on the coordinated phenomena of the sol-gel chemistry and self-assembly of the template molecules but also on the kinetics of diffusion of volatile species [2].

Table 3.1: Successful literature results on mesoporous WO_3 films

Surfactant/ Precursor	Solvent	Calcination conditions	Pore's diameter(nm)/ Mesostructure	Film's thickness (nm)	Crystallinity	Application	Reference
P123/PTA	EtOH	200°C/15h, 250°C/4h	d_{100}=2.5/2D hex	<100-150	crystalline	NH_3 gas sensing	[1]
TMDD/WCl_6	EtOH	300°C/2h	3-4/worm-like	200	semicrystalline	electrochromism	[3]
PEG600/WCl_6	EtOH	450°C/30min	N.A	<200	mainly amorphous	electrochromism	[4]
KLE/WCl_6	EtOH/THF	100°C/1h, 300°C/12h, 550°C/1.5h (O_2)	12-13/Cubic	150	polycrystalline	electrochromism	[5]
TMDD/WCl_6	EtOH	120°C/exposure to high RH, 300°C/2h	3.7/worm-like	N.A	N.A	electrochromism	[7]
F127/WCl_6	EtOH	60°C, 250°C/5h washed with EtOH (remove the surfactant)	5.4	N.A	nanocrystallites	NO_2 gas sensing	[9]
P123/WCl_6	EtOH	40°C/ washed with EtOH (remove the surfactant)	4-8/no order	400-500	amorphous	electrochromism	[11]
Tween 60/PTA	H_2O/EtOH	100°C/1h 300°C/1h	no porosity	N.A	N.A	N.A	[12]
Brij-56/PTA	H_2O/EtOH	190°C/2h 350°C/1h	2-3/hexagonal	~100	N.A	electrochromism	[12-14]
P123/Brij-35/PTA	H_2O/EtOH	100°C/1h 200°C/20min	no porosity	N.A	N.A	N.A	[14]
KLE/WCl_6	EtOH	550°C	6/cubic	150	crystalline	Electrochromism	[15]

P123 ($EO_{20}PO_{70}EO_{20}$), TMDD ($C_{14}H_{24}EO_{20}$), PEG (HO-[CH_2CH_2O]-H, KLE ($H(CH_2CH_2CH_2(CH)CH_2CH_3)_{89}(OCH_2CH_2)_{79}OH$), F127 ($EO_{100}PO_{64}EO_{100}$), Tween 60 ($C_{24}H_{46}O_6(C_2H_4O)_{20}$), Brij-56 ($C_{16}H_{33}EO_{10}$)

Templating in combination with the dip-coating technique is utilized very commonly for the synthesis of mesoporous films. For the synthesis of mesoporous tungsten oxide films a versatile number of surfactants and tungsten precursors have been employed and different mesostructures have emerged, as it is shown in Table 3.1.

As it was explained in the introduction (chapter 1) in this PhD, Brij-56 (or Brij-C10) was used as a structure directing agent ($C_{16}EO_{10}$). This surfactant is an oligomer and produces pores with a small size (2-3 nm). The privilege of oligomers, is that they possess small hydrophilic segments, rendering the pores more sustainable towards thermal treatment. It is more difficult to decompose surfactants with higher hydrophilic chains (such as P123) and preserve an organized mesostructure due to stronger interactions with the inorganic framework [14]. For comparison purposes a larger triblock co-polymer (F127, $EO_{100}PO_{64}EO_{100}$) was also used which could potentially produce larger pores [16] and thicker inorganic walls [17].

In addition, all the films that were studied in this thesis were amorphous (unless otherwise mentioned). It has already been documented in the literature that amorphous films exhibit better electrochromic performance than the crystalline films [18, 19]. Our study in this chapter corroborates with this statement. Further discussion will take place in the following paragraphs.

3.2 Experimental part

For the synthesis of mesoporous WO_3 films, APTA precursor was used as described in chapter 2.

The experiments for the preparation of mesoporous WO_3 films were based on previous publications [10-12]. Typically, 1g of APTA was dissolved in 2g of milliQ water and 1g of absolute ethanol (Fischer Scientific). The solution was stirred at room temperature for 2h. The surfactant solution was prepared by dissolving 0.2g Brij-56 (Brij C10, Mn~683, $C_{16}H_{33}EO_{10}$ Aldrich) in 2.5g of milliQ water and 1.25g of absolute ethanol and the mixture was stirred in a water-bath at 40^{o}C for 2h. After mixing both solutions (W/EO molar ratio =~1 based on the TGA measurements presented in chapter 2), the final solution was stirred for 1h at room temperature before using. This mixture remains stable for several days. However, once it is heated at 40^{o}C or 60^{o}C a white solid precipitate (tungstic acid) occurs in less than 10 min. For the dense films, the same procedure was followed, without the addition of the surfactant. However, it was observed that the adherence of the film was seriously reduced without the surfactant and thus a very small amount of Brij-C10 was added.

The WO_3 thin films were deposited on pre-cleaned glass substrates (SnO_2:F coated glass substrates, TEC15, 15Ω/sq, 2cm x 2cm x 2,2mm, Dyesol) and silicon wafers. The substrates were cleaned by consecutive immersion under sonication in milliQ water (5min), acetone (15 min) and ethanol (15 min). Then, the substrates were dip-coated in the aforementioned final solution at a constant dipping speed (2.5 mm/s) and controlled relative humidity (50%). After deposition, the films were left in the chamber for 5 min before being

thermally stabilized in an oven at 170°C for 1h in order to evaporate the remaining solvents and initiate the polymerization of the film. Finally, the films were calcined at a high temperature under air (heating ramp 1°C/min, natural cooling down in the furnace) to induce the formation of the oxide. The dense films were calcined at 300°C for 1h to avoid crystallization. The mesoporous films were calcined at 350°C for 2h. The presence of surfactant in the material was reported to delay the crystallization of tungsten oxide [4, 11]. Moreover, such a higher temperature for a longer period of time is required to ensure the total elimination of the surfactant.

For comparison purposes, a few experiments were conducted with another surfactant F127 (EO_{109}-PO_{70}-EO_{109}) instead of Brij-56. In this case, 0.18g of F127 were used in order to obtain the same W/EO molar ratio.

After calcination, dense films were translucent while mesoporous films possess a pale yellow-brown color. Moreover, all the films obtained from this experimental procedure contain defects (visually detected as spots). As it will be discussed later in this chapter, these spots are attributed to the formation of cracks which are formed at the very early stages of deposition (as soon as the drying line passes). Additionally, the films exhibit non-reproducible thickness which is visible from the different colorations observed on Si wafers from sample to sample. In order to address these problems different experimental modifications have been attempted as it will be discussed in the next paragraph.

The films were structurally characterized by profilometry, X-Ray Diffraction (XRD), Transmission Electron Microscopy (TEM), Scanning Electron Microscopy (SEM), Infrared Spectroscopy (IR), Raman analysis, UV-Vis spectroscopy and ellipsometry.

The thickness was determined by mechanical profilometry (Dektak 150, VEECO) on the FTO/glass substrates.

X-ray diffraction was performed on a Bruker D8 diffractometer (CuKalpha radiation) in grazing incidence configuration with an incident angle of 0.5°, a 2-theta range from 10° to 70°, a step size of 0.02° and a scan speed of 1 s/step. All the films that have been studied are amorphous unless otherwise mentioned.

TEM micrographs were acquired at an acceleration voltage of 200kV in bright field (BF) modes (Tecnai, G2, Twin, FEI). Films were scratched from the substrates, sonicated in ethanol and then deposited on a carbon-coated grid.

The morphology and the relative amount of W in the films was studied by SEM (FEG-ESEM XL30, 15kV, FEI and EDS spectrometer, Bruker). The relative amount of W in the films was extracted from their X-ray emission spectrum. More specifically, the intensity of W Lα peak was recorded and compared to a pure W standard to calculate the so-called k-ratio of tungsten atom in the films. We used this k-ratio value to normalize the charge capacity of the films in electrochemical experiments.

IR spectra were recorded in transmission mode from films deposited on silicon wafers using a Bruker Equinox 55 FTIR instrument. The reference was a bare silicon wafer.

Raman measurements were performed directly on films deposited on FTO/glass substrates using a Horiba- Jobin Yvon LabRam 300 spectrometer equipped with a microscope (x100 Olympus objective). The excitation laser was a He-Ne (Melles Griot) emitting at 632.8 nm and the power at the sample was 0.6 mW. For each sample, the Raman spectrum of the glass was recorded on a film-free area and quantitatively subtracted (until disappearance of the silicate 1100 cm^{-1} band). For the coloration process, the sample was subjected to -1V vs. Ag/AgCl/KCl (3.5M) for 120s and for the bleaching process the film was subjected to -1V vs. Ag/AgCl/KCl (3.5M) for 120s and then at +1V vs. Ag/AgCl/KCl (3.5M) for 120s at ambient atmosphere. Before acquisition, the electrochemically modified films were rinsed with pure acetonitrile in order to remove any propylene carbonate's residues.

Ellipsometric measurements were performed on an ultraviolet-visible (from 250 nm to 1000 nm) GES5E Spectroscopic Ellipsometer from SOPRALAB, and the data analysis was performed with the WINSE software. First, the optical response of the dense film was modelled and it was used as a reference film. The dispersion law was tuned to fit the best with experimental ellipsometric parameters (cos Δ, tan Ψ) between 200-800 nm. It consists in a standard dielectric function with a Cauchy law for the visible and UV description. A vibrational term is added in the form of a Lorentz absorber at 300 nm to improve fitting. The optical index η (real part of the refractive index) obtained for the reference film is 2,3-2,4 at λ = 525 nm.

Secondly, porous films (with Brij-56 and F127) were analyzed and fitted with a model mixing voids and dense film. The fitted data give access to a global η_λ optical index resulting from the averaged response of dense walls and empty pores, following the Bruggeman mixed phases law. This analysis was performed on 2 replicates and 3 distinct points on each type of films. The results were considered valid when the quantity of the fitting was $R^2 > 0.99$ and they are presented in Table 3.2.

Table 3.2: Ellipsometric parameters for the porous and dense films

Film	η_{525}	thickness	Percentage of air (%)
Porous film (Brij-56)	2.080	110	23
Porous film (F127)	2.244	130	12
Dense film	2.3-2.4	80-100	---

We also tried to perform adsorption-desorption of water in order to obtain information regarding the pores size and size dispersity but these experiments did not succeed due to an artefact at very high relative humidity. Specifically, the wet films did not give any fridges in the cos Δ, tan Ψ at a refractive humidity close to 100%, making the fitting of thickness and refractive index impossible. This was observed on both porous films. Moreover, the observed steady-state thickness upon water vapor increases suggesting that the films are water repellant. The treatment of films by UV irradiation in order to remove possible organic residues and activate the hydrophilicity of the surface did not solve the problem. Moreover, we observed that the optical index had a tendency to decrease with water uptake, which is contradictory to what is expected in an absorption experiment. We suppose that

the haziness of the films in the dried state is lowered at high relative humidity, resulting in a modification of the optical behavior (diffusive-transparent transition) which cannot be supported by the model.

The electrochemical properties were determined using a three electrode configuration (Figure 3.3 a) in which the working electrode consisted of the dip-coated WO_3 films deposited on FTO/glass substrates in contact with a 0.5M $LiClO_4$ (≥95.0%, Aldrich) in anhydrous propylene carbonate (99.7%, Aldrich) solution.

The reference electrode was an Ag/AgCl/KCl (3.5M) and the counter electrode was a platinum foil. The experiments were carried out on an SP-200 BioLogic potensiostat with an EC-Lab express software for collection and analysis of data. Prior to each electrochemical measurement, the electrolyte solution was bubbled for 10 min with purified N_2 gas in order to purge dissolved moisture and oxygen. Afterwards the cell was let in an open circuit voltage for 1 min in order to reach equilibrium conditions. Two kinds of electrochemical measurements were conducted, cyclic voltammetry and chronoamperometry. In cyclic voltammetry, current was measured against the applied voltage in the range of ±1V vs. Ag/AgCl/KCl (3.5M) at a constant voltage scan rate ($20mV.s^{-1}$). In chronoamperometric measurements, current was measured with respect to time at constant voltage steps (-1V for 120s, +1V for 120s).

The electrochemical performances were also studied in an argon-filled glovebox, in the absence of air and humidity. A three-electrode configuration was used as well (Figure 3.3 b), where the WO_3 was completely immersed in the electrolyte solution (in this case the $LiClO_4$/PC electrolyte was purged with Ar, dried with molecular sieves and stored in the glovebox). Li foil was used as a reference and a counter electrode as well. The experiments were carried out on Princeton Applied Research- EG&G, 263A potensiostat with a CVIEW 2 software for collection and analysis of data. Prior to each electrochemical measurement, the film remained in a vacuum chamber for 5 mins in order to remove the moisture and free oxygen. The same experiments were conducted as described in the previous paragraph, cyclic voltammetry and chronoamperometry in a voltage range of 2.225 V and 4.255 V vs. Li/Li^+.

The UV spectra were acquired ex-situ on a Perkin Elmer lambda 14P (300-1000nm). For the measurement, 1 cm polystyrene disposable cuvettes filled with electrolyte were used. The film was immersed in the electrolyte sealed on top and transferred in the UV chamber before or after the electrochemical measurement (chronoamperometry). A cuvette filled with electrolyte was used as a reference.

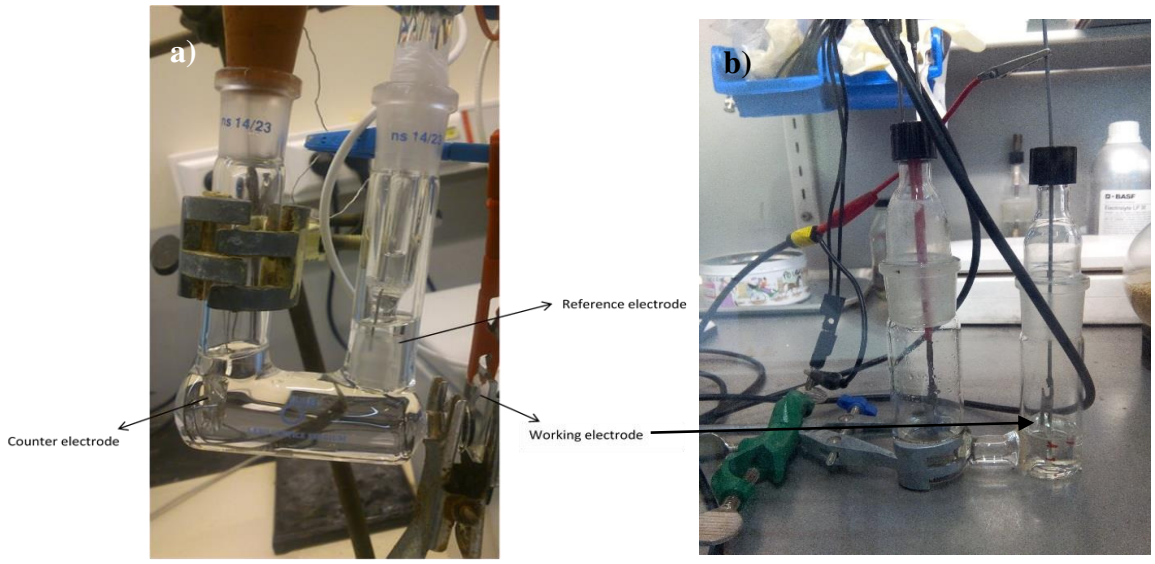

Figure 3.3: Electrochemical set-up a) in ambient conditions and b) in the glovebox

3.3 Results and discussion

3.3.1 Microstructural properties

Improvement of visual homogeneity

All the attempts to improve the quality of the films are shown in Table 3.3. Unfortunately, none of them resulted in crack-free and uniform films.

Generally, cracks occur due to intrinsic, thermal or mechanical (external) stresses. The former is induced by different factors such as grain growth, defect annihilation (vacancies at grain boundaries), phase transition and evaporation of the solvent. In our case, the latter seems to induce the occurrence of surface cracks, since they emerge instantly after the deposition, as soon as the drying line passes (Figure 3.4). Therefore, the increase of the evaporation rate (by increasing the ratio of ethanol/water, see Figure 3.4) gives rise to bigger spots (subsequently bigger cracks).

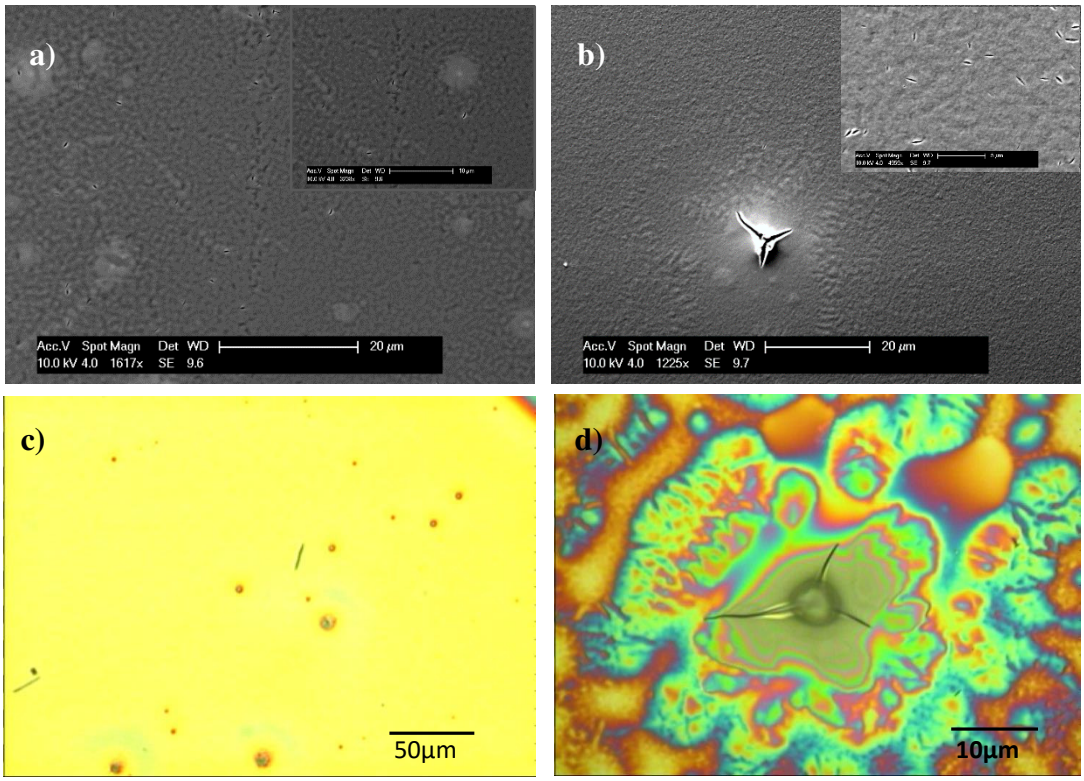

Figure 3.4: a) b) SEM micrographs of a a) calcined dense and b) calcined surfactant-assisted film c), d) cracks under the optical microscope (the films were stabilized at 170°C)

In Figure 3.4, SEM micrographs and optical microscope images confirm the presence of multiple spots/cracks in both dense and porous films. As it is shown in Figure 3.4 b, c and d, porous films are comprised by at least two types of cracks: big cracks of more than 10 μm that stem from the interface between the substrate and the film (micrographs b, c, d) and smaller cracks less than 2 μm which occur on the surface of the films (see the inset in b). By comparing the porous film (micrograph in b) with the dense film (micrograph in a) it is concluded that the surfactant-containing solution exhibits better wetting properties than the surfactant-free solution (more visible in the insets). This effect (which will be more distinct in the spraying method chapter) is attributed to the decrease of the solution's surface tension and the subsequent improvement of its coating properties [20-25].

In order to reduce the stresses arising during evaporation, a much less volatile solvent (ethylene glycol) was used in expense of ethanol (see Table 3.3 and Figure 3.5). Even though at low concentrations, ethylene glycol did not have any impact on the porosity or the appearance of the films, at higher concentrations the evaporation rate became very low and less uniform throughout the film (different drying lines and thicknesses). Moreover, the long range periodicity of the pores decayed as the amount of ethylene glycol increased (see also the TEM micrograph of an ethylene-glycol free film in Figure 3.7 a). This observation signifies that the presence of ethylene glycol disrupts the self-assembly of micelles during evaporation.

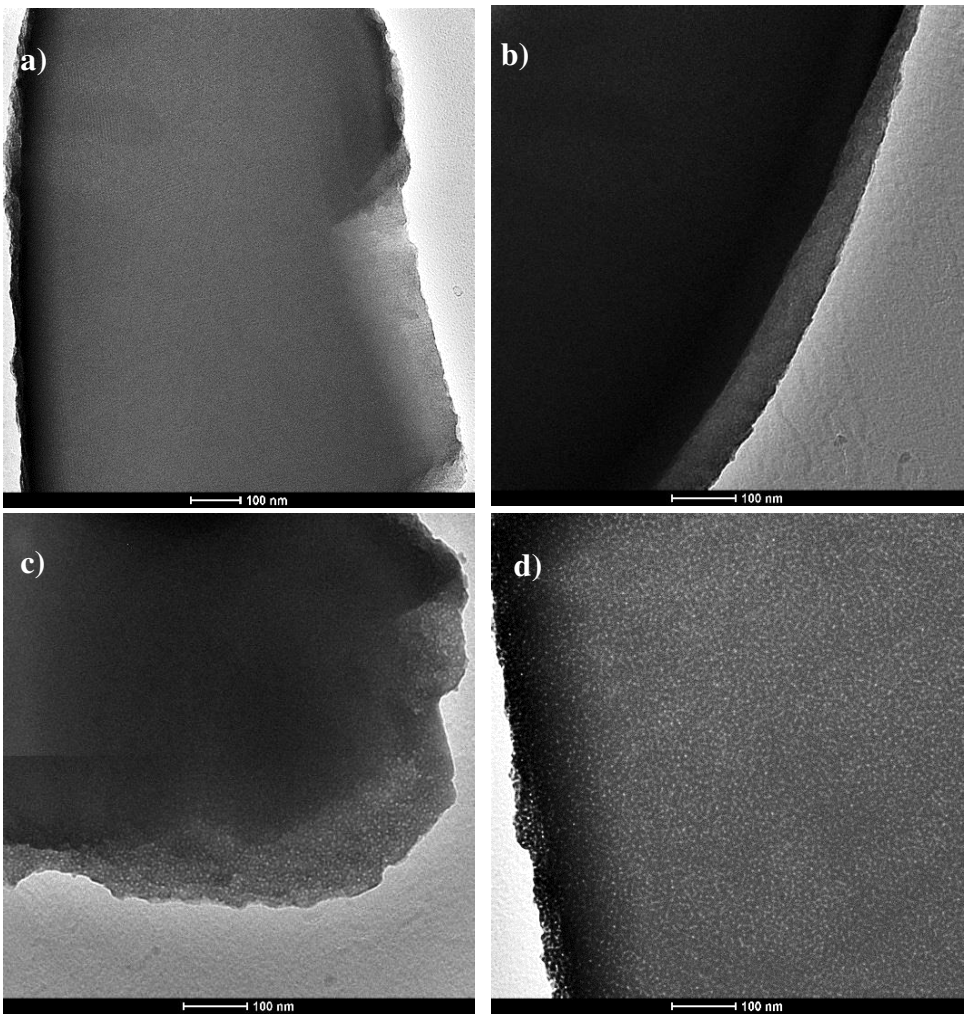

Figure 3.5: TEM micrographs of porous films with a) 0.25 g EG/0.75 g EtOH before any thermal treatment b) 0.75 g EG/0.25 g EtOH before any thermal treatment c) 0.50 g EG/0.50 g EtOH after calcination d) 0.75 g EG/0.25 g EtOH after calcination

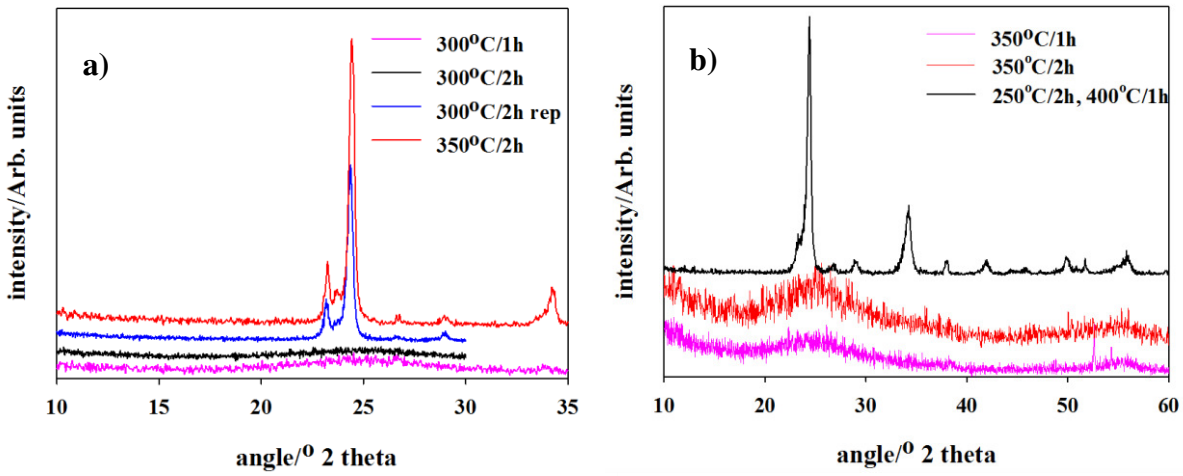

Figure 3.6: X-ray diffractograms of films prepared a) without and b) with Brij-56 in the coating solution

Table 3.3: Trials to improve the quality of the films

Modified parameter	"standard" procedure	Modified procedure	Observation
EtOH:H_2O weight proportion	1.25:2 (surfactant solution)	2.00:1.75 3.25:0.5	immiscible phases
		3.75:0.00	white solid after mixing the two solutions
EtOH:H_2O weight proportion	1.00:2:00	3:00:0.00 (precursor and final solution was also stirred at 50°C)	transparent solution not uniform films large spots (cracks) not porous films (data not shown)
RH%	50%	30%, 70%	not uniform films many spots (cracks)
storage at high relative humidity	-----	stored overnight in a closed chamber under RH 75%	many spots (cracks)
Addition of ethylene glycol	-----	0.25 g EG/0.75 g EtOH precursor solution	no change ordered porosity
		0.50 g EG/0.50 g EtOH precursor solution	Inhomogeneous films. Presence of cracks less ordered films
		0.75 g EG/0.25 g EtOH precursor solution	Very slow and inhomogeneous evaporation. Presence of multiple drying lines and cracks no periodical pores

Effect of thermal treatment on crystallinity and porosity

As it was already discussed earlier and in the introduction (Chapter 1), amorphous over crystalline films have been selected in this PhD.

Figure 3.6 displays the X-ray diffractograms of films which have been thermally treated at different conditions, prepared in the absence and in the presence of Brij-56 (Figure a and b respectively). From the diffractograms, it is straightforward that the presence of surfactant in the coating solution delays the crystallization of tungsten oxide. The surfactant-containing films remain amorphous up to 350°C/2h while the dense films are already crystalline at these conditions. It appears that crystallization in the dense films initiates even at a lower temperature (300°C). This is evidenced by the non-reproducible diffractograms when the film was annealed for 2h at 300°C. The effect of crystallization obstruction in the presence of a surfactant is already documented in the literature. For example A. Cremonesi et al. [4] and W. Cheng [11] et al. observed a crystallization delay when using PEG and P123 respectively as structure directing agents. Presumably, the interactions of the template with the inorganic matrix upon calcination reduce the nucleation rate of the W-O groups [26].

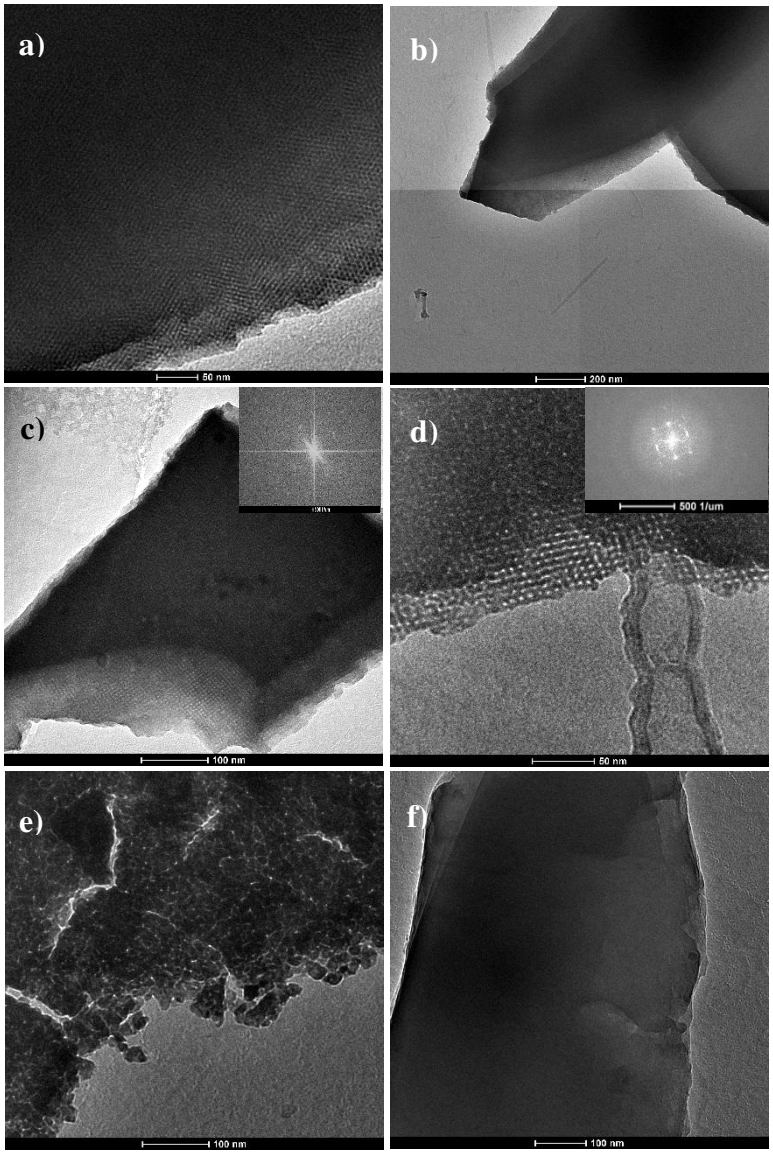

Figure 3.7: TEM micrographs of a film a) stabilized at 170°C b) annealed at 250°C. The visible quadrants are a temporary artefact of the camera c) annealed at 350°C/1h d) annealed at 350°C/2h e) annealed at 250°C/2h and then at 400°C/1h f) dense film at 300°C/1h. In c) and d) the corresponding fast Fourier transformation patterns are displayed

The post-thermal treatment is an important step in the surfactant assisted sol-gel method. Many structural modifications occur during this step such as solvents evaporation, polymerization of the network, crystallization, surfactant's elimination etc. It is already well documented that for the formation of a stable mesostructure, an intermediate thermal step is required otherwise pores collapse or their thermal resistance is significantly reduced. At this step, the solvent is evaporated, the surfactant is partially decomposed and the polymerization process is initiated before the surfactant is completely departed from the material [5, 7, 12, 14, 27].

In this PhD, 170°C was selected as an intermediate temperature. At this temperature, most of the peroxides and some of the acetate groups are decomposed (based on the TGA measurement in chapter 2) and subsequently the partial polymerization begins. On the other hand, surfactant is completely decomposed at around 400°C [14]. Therefore, at 170°C most of the surfactant is still inside the pores of the films. IR spectrum corroborates with the above statements (data not shown). Figure 3.7 shows the TEM micrographs of films which were annealed at different temperatures. Long-range organized open pores of about 3 nm oriented in different directions and wall thicknesses of about 5 nm are observed during the stabilization step at 170°C (Figure 3.7 a). Upon annealing at 250°C/1h, (Figure 3.7b) mesostructure is preserved, however the low quality of the images did not permit us to calculate the pore size and wall thickness. Ordered mesopores are still observed at a higher temperature (350°C/1h, Figure 3.7 c). At this temperature, the extended polymerization resulted in the ordering of porosity in fewer directions compared to the stabilized film in Figure a. Moreover, due to the elimination of the surfactant, the polymerization of the network and the subsequent contraction, the wall thicknesses and pore sizes were slightly reduced (~3nm and ~2nm respectively). The Fast Fourier Transformation pattern in Figure c confirms the presence of ordering by pairs of dots possessing specific orientations. We calculated the pore-to-pore distance from the distance between opposite located dots, which is around 5 nm in this case. The brownish color of the films indicated that at this temperature not all of the combusted surfactant products have been removed. For this reason, we subjected the films to ozonolysis for 30 and 60 min. However, no difference in the color has resulted.

In order to fully eliminate the residues of the organic substances, we applied an extended thermal treatment (at 350°C) for 2h rather than 1h. The extension of the thermal treatment by 1h did not affect the pores size, or wall thicknesses (~2 nm and ~3 nm respectively) and therefore we have decided to proceed in electrochemical measurements with the films treated at 350°C for 2h.

Further increase of temperature (400°C/1h, Figure d) and the introduction of an additional intermediate thermal step (250°C/2h) had led to the formation of crystalline films as already discussed in the previous paragraph. Subsequently under this thermal treatment, porosity is collapsed and individual crystalline particles started to grow.

As expected, the film prepared in the absence of a surfactant lacks of porosity and it appears dense and compact in the TEM micrographs (Figure 3.7 e). According to the ellipsometric measurements the film that has been prepared in the presence of Brij-56 and calcined at 350°C/2h contains 23% of porosity compared to the dense film.

Vibrational investigation by infrared spectroscopy

FT-IR spectra (Figure 3.8 and Table 3.4) show that mesoporous films contain a great number of hydroxyls and water molecules physically or chemically absorbed inside the pores of the material [28]. Therefore mesoporous films can be described as a $WO_{3-x-y}OH_x.yH_2O$ material with different hydration and hydroxylation modes [28] in the high and medium wavelength regions (2650-3700 cm^{-1}, 1620 and 1420 cm^{-1}) while dense film is

much less hydrated. Apart from this difference, the FT-IR spectra of the two films look very much alike. As we will show in the discussion of the Raman spectra in the following paragraphs, the two films possess more structural differences than presented here.

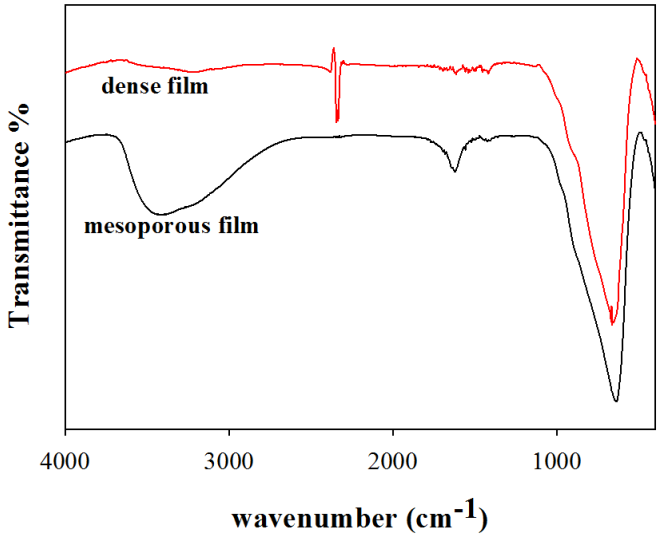

Figure 3.8: Infrared Spectra of a porous and a dense film

Table 3.4: Infrared peaks assignement for the porous and the dense films

Mesoporous film (cm^{-1})	Dense film (cm^{-1})	Peak assignment [29]
644	663	v-O-W-O
1420	NA	δ-OH
1642/1623	NA	δ-OH (structural)
----	2345	CO_2 (instrument's artifact)
2568-3757	----	Surface H-OH, hydroxylation and hydration

Change of template

As mentioned earlier, we have tried to prepare ordered porous films with the triblock co-polymer F127 (EO_{109}-PO_{70}-EO_{109}). According to the theory, surfactants with high molecular weight could potentially lead to larger pores [16] and thicker inorganic walls [17]. In the literature, F127 produces cubic [16, 30] and worm-like [31] architectures, depending on the experimental parameters such RH% and surfactant-to-metal ratio.

Here, we obtained worm-like architecture with F127 for the film that was stabilized at 170°C (Figure 3.9 a). The worm-like mesophase and the random pores orientation has also been confirmed by the Fast Fourier Transformation pattern (inset in Figure a). The pattern reveals a constant pore-to-pore distance of ~9 nm. By calcining the film at 350°C for 2h most of the pores collapse as shown in Figure 3.9 b. According to ellipsometry measurements, the calcined films prepared with F127 possesses 12% of porosity compared to the dense film.

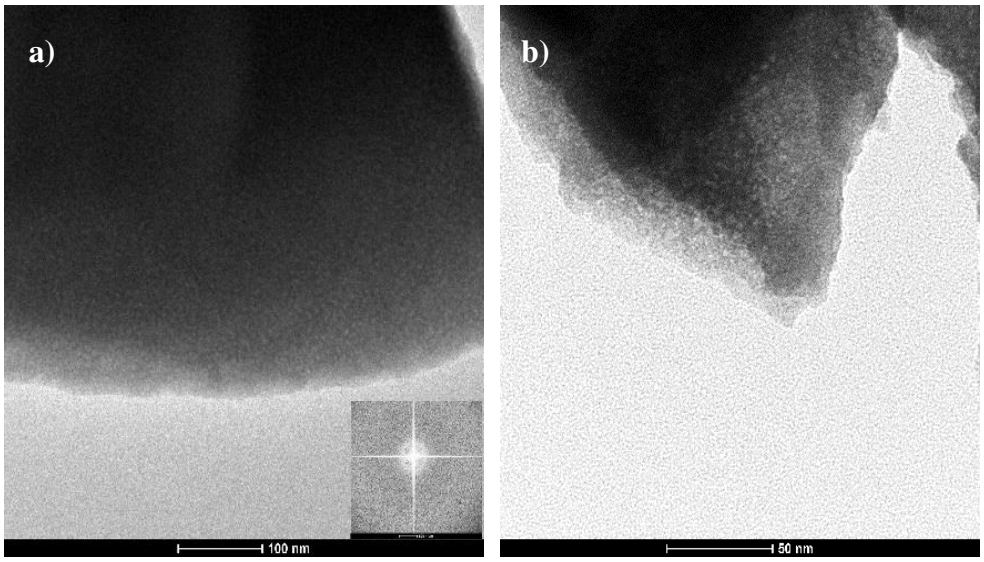

Figure 3.9: TEM micrographs of films prepared with F127 a) stabilized at 170°C/1h b) annealed at 350°C/2h

Thickness and W content

In Table 3.5 the values of thickness, k-ratio and the percentage of air for dense and porous films are listed. From the values, it is evident that the films thickness emerging from this experimental process are very low. Moreover, the values acquired from profilometry and ellipsometric measurements are not consistent. This is probably due to the morphology of the substrate (rough surface of the FTO), or a lower adherence of the coating solution on the FTO surface compared to the silicon wafers.

The k-ratio values which were acquired from the Energy Dispersive X-ray (EDX) method correlates the surface area of the W peak with the amount of W in the film based on the surface area of a pure W reference. Based on that value, we compared the relative amount of W in the films. In the following paragraphs we will use the k-ratio values in order to normalize the charge capacities of the films according to their W content. According to the values of Table 3.5 porous films (with Brij-56) possess the lowest amount of W.

Table 3.5: Thickness, k-ratio and percentage of air for different films

Film	Thickness (nm)[1]	k-ratios	Percentage of air (%)[2]
Porous film (Brij-56)	60-80 [110]	0.15	23
Porous film (F127)	N.A.[130]	0.24	12
Dense film (1 layer)	30-50 [80-100]	0.19	N.A
Dense film (2 layers)	N.A.	0.37	N.A

[1] The values in brackets were calculated by ellipsometric measurements (Si wafers) while the actual values were acquired from profilometry from films deposited on FTO glass
[2] Extracted from ellipsometric data

Influence of crystallinity

The effect of crystallinity on the electrochromic performance of WO_3 films has been the subject of interest in numerous publications. Firstly, crystalline or polycrystalline films

interact differently with light compared to their amorphous counterparts. The formers modulate optical transmission by absorption and reflection mostly in the near infrared regions and the coloration is attributed to a Drude-like free electron absorption (or scattering) model while the latter modulate light by absorption in the visible spectrum (polarons formation) [32-34]. Moreover, in polycrystalline films, the microstructure plays a significant role on the electrochemical properties and therefore the control over the grain size and the inter-particle porosity is considered to be very crucial [5]. For example, some publications report that the grain size should be small enough to permit fast kinetics and large enough to minimize electron scattering and subsequently films resistivity [32, 35]. S. Sallard et al. [5] studied the electrochromic properties of WO_3 films with varying degrees of crystallinity. They found that crystalline films increase the energy barrier for cations insertion and subsequently their charge capacity and coloration properties [36] are inferior compared to the amorphous films. Contrarily, owning to their more rigid framework, crystalline films are more reversible and more sustainable upon continuous cycling. On the other hand, Y. Zhang et al. [3] and T. Brezesinski [15] reported that semicrystalline porous films possess better electrochromic performance compared to fully crystalline and fully amorphous films in terms of reversibility, optical modulation, and coloration efficiency. This is due to the large surface area induced by porosity and the surface nanograin boundaries.

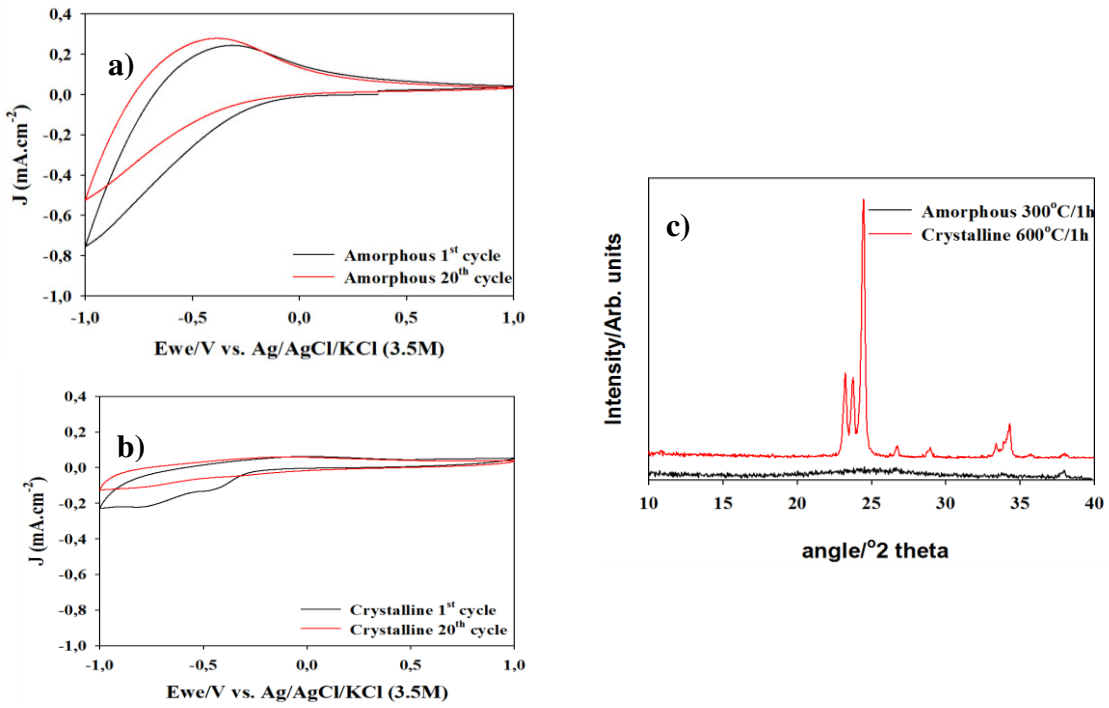

Figure 3.10: Cyclic voltammograms of a) a dense amorphous film calcined at 300°C/1h b) a dense crystalline film calcined at 600°C/1h. The voltage scan rate was 20mV.sec^{-1}. c) corresponding X-ray diffractograms

In our case, the crystalline films exhibit a milky appearance presumably as a result of the diffusive light scattering from the crystalline grains. This effect constrains the potential of these materials to modulate light efficiently.

3.3.2 Electrochemical properties of porous and dense films

In Figure 3.10 the cyclic voltammograms of an amorphous (Figure a) and a crystalline film (Figure b) along with their X-ray diffractograms (Figure c) are presented. From these voltammograms it is straightforward that the shape of the curves is substantially influenced by the microstructure of tungsten oxide. More specifically, the amorphous film exhibits a typical cyclic voltammogram with no noticeable peaks during intercalation and an ill-defined peak during de-intercalation. The featureless shape of this voltammogram is indicative of the amorphous nature of the film [32, 37, 38]. On the other hand, the crystalline film possesses two distinct cathodic peaks at around -0.5V and at -0.8V which are attributed to the monoclinic (triclinic)-tetragonal and tetragonal-cubic transitions [15]. Moreover, it is straightforward from the cyclic voltammograms that the current induced in the crystalline films is much less compared to its amorphous counterpart. By converting the above voltammograms into I = f(t) graphs and calculating the amount of charge that is intercalated and de-intercalated from both films, it is concluded that the amorphous film intercalates ~3 times more lithium cations compared to the crystalline film (Table 3.6).

In accordance with the literature, the crystalline films exhibit a slightly better reversibility compared to the amorphous films, while the latter remain blue after the electrochemical characterization. Despite of that, we decided to study amorphous films rather than crystalline ones due to their significantly higher charge capacity and to emphasize on the role of the templating on the electrochromic properties of the films without compromising porosity due to crystallites growth.

Table 3.6: Charge capacities and reversibilities calculated by the cyclic voltammograms (I=f(t)) in the 1st and 20th cycle

Film	Charge intercalated (mC.cm^{-2})	Charge de-intercalated (mC.cm^{-2})	R (%)
Amorphous	20.3 [11.8][1]	11.2 [11.1]	55 [94]
Crystalline	7.3 [4.0]	4.5 [4.1]	61 [100]

[1] In brackets the corresponding charge capacities (reversibilities) in the 20th cycle are presented

Influence of porosity

Figure 3.11 illustrates the cyclic voltammograms of porous films prepared with Brij-56, films with a very low percentage of porosity (prepared with F127) and dense films (surfactant-free). All the films are characterized by smooth voltammograms as a result of their mainly amorphous nature and a well-defined anodic peak. The dense film (Figure a), presents large modifications between the first and the rests of the cycles due to the substantial trapping of lithium cations (Table 3.7) in the first cycle. Upon further cycling, the dense film exhibits good persistence and durability, as concluded from the superimposition of the curves at the 10th and 20th cycle. This film has been tested up to 1000 cycles (data not shown) and we observed that its activity is not severely altered upon consecutive cycling. However, after the electrochemical measurement it remains blue unlike the two more open-structured films whose reversibility is substantially improved (Table 3.7). We also observed that the F127 films exhibit similar capacity properties with

the Brij-56 (Table 3.7) despite the significant pores fraction difference. This is attributed to the higher content of W (see k-ratio in Table 3.5) in the films prepared with F127.

Owning to their different surface architecture, mesoporous films possess an extra anodic shoulder (0.8-0.9V), which probably stems from the de-intercalation of cations located at different surface sites [11, 39-41]. Some authors who studied proton intercalation/de-intercalation, associated the origin of the peak with the work of D-J Kim and S-I Pyun [42] who supported that water-rich films (in their case sputtered films, in our case porous films) provide wider path for proton movement in the film and suggested the existence of different proton sites. In other publications [41, 43] which studied the intercalation of ***lithium cations*** in the presence of added water or in water-rich films, it was suggested that the second anodic peak is attributed to protons and the main peak to the lithium cations. Moreover, it was found that the intensity of the second anodic peak was increased as the amount of water in the electrolyte was increased as well [43]. The effect of water in the electrochemical properties of the films will be discussed in more detail in a following paragraph.

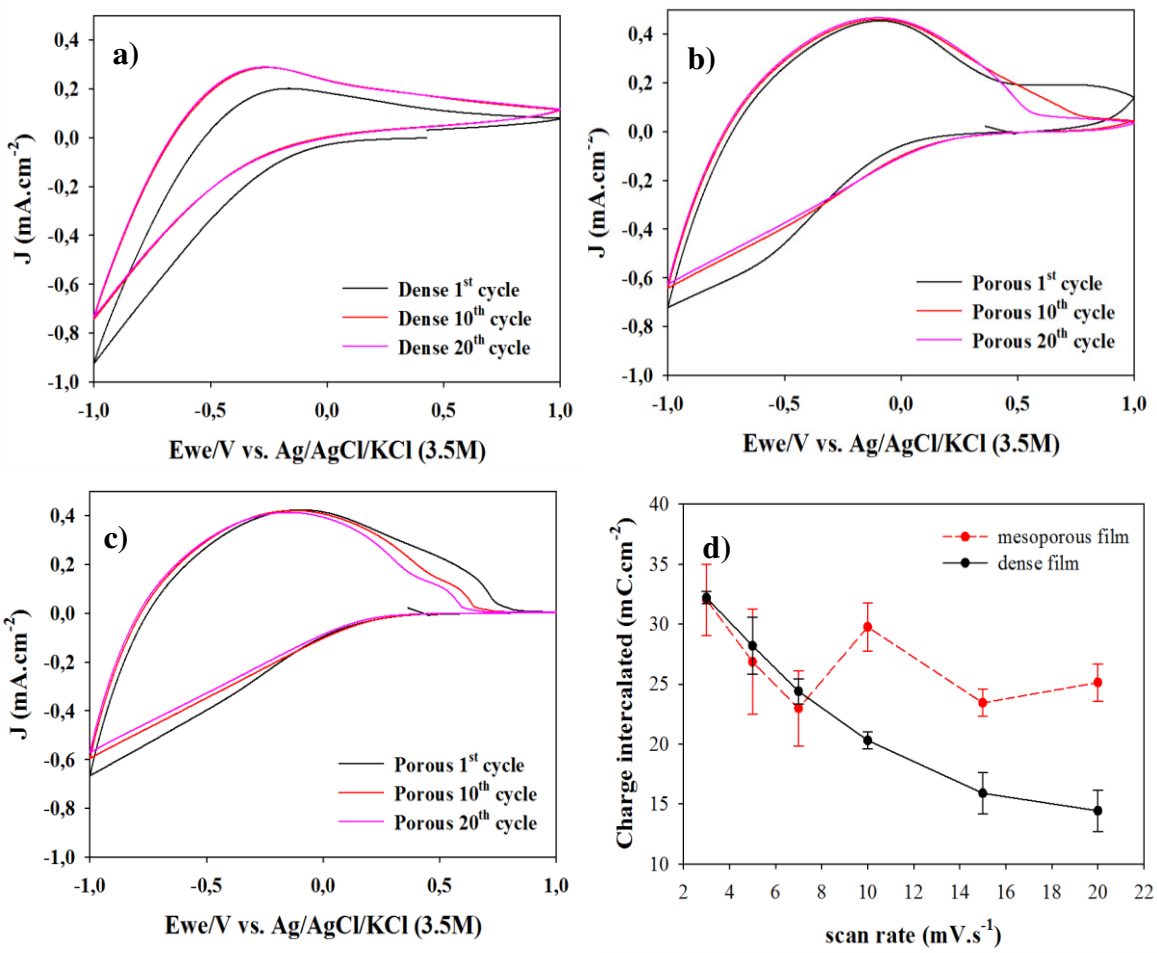

Figure 3.11: Cyclic voltammograms of a a) dense film (2 layers) b) template-assisted film (F127) and template-assisted film (Brij-56). Scan rate: 20mV.sec^{-1} d) plot of the inserted charge (10th cycle) in the dense and the mesoporous film vs. the scan rate in cyclic voltammetry (we used the 1-layered dense film in these experiments)

Table 3.7: Charge capacities and reversibilities calculated by the cyclic voltammograms (I=f(t)) in the 1st and 20th cycle

Film	Charge intercalated (mC.cm^{-2})	Charge de-intercalated (mC.cm^{-2})	R (%)
Dense (2 layers)	29 [17.5]	12.6 [15.9]	43 [91]
Templated with F127	25.5 [23.1]	24.7 [23.2]	97 [100]
Porous (Brij-56)	23.8 [19.1]	22.3 [18.9]	94 [99]

In parenthesis the corresponding charge capacities (reversibilities) in the 20th cycle are presented

In order to investigate Li^+ insertion/de-insertion kinetics, we plotted the intercalated charge at the 10th cycle, against the voltage scan rate for the porous (Brij-56) and the dense film. As observed in Figure 3.11 d, in the case of the dense film when the scan rate increases, the intercalated charge progressively decreases, while in mesoporous film it remains somewhat constant. This is a direct evidence that the dense film does not have the time to reach equilibrium conditions as the scan rate increases in contrast to the mesoporous film.

The chronoamperometric measurements permitted the calculation of the switching kinetics (the time needed to attain the 10% of the initial current value) and the charge capacity of the films (Figure 3.12 a and b and Table 3.8). From the values in Table 3.8 (and Figure 3.12 a) and in accordance with the literature and the plot in Figure 3.11 d it is discerned that the more porous the film is, the faster the switching kinetics for both intercalation and de-intercalation processes are. It is also observed that the switching kinetics for the de-intercalation process are always faster than the switching kinetics of intercalation. This is attributed to two factors: i) in the de-intercalation process, the electronic conductivity of the Li_xWO_3 layer is higher than the one of WO_3 ((if a free-charge-carrier Drude model is assumed [44]) ii) during intercalation a back electromotive force (EMF) is developed which delays the coloration process while the de-intercalation process is a spontaneous reaction [45].

The evolution of the charge capacity (Figure 3.12 b) with cycling follows a similar trend with the results of Table 3.7. Based on the chronoamperometric measurements, the three films possess a capacity between 70-80 mC.cm^{-2} in the first cycle. In the next cycles, the dense film loses almost 30% of its capacity but it remains stable upon further cycling. The porous film exhibits a progressive degrading capacity, presumably due to the progressive degradation of the film with cycling. This is a reasonable result if we consider the high contribution of water in the mechanism of intercalation and de-intercalation in the porous film.

Table 3.8: Switching kinetics for the films calculated from chronoamperometric measurements (acquired at ambient atmosphere)

Film	t_{int} (1st) (s)	$t_{de\text{-}int}$ (1st) (s)	t_{int} (20th) (s)	$t_{de\text{-}int}$ (20th) (s)
Dense	>180	25	111	32
Templated with F127	82±21	20±0	66±1	17±4
Porous Brij-56	33±4	8±3	21±6	4±1

Ex-situ Raman analysis

In order to specify the origin of the traps evidenced for the dense film and to better understand where Li^+ cations reside inside the materials, we performed Raman measurements on a dense and a porous film (Brij-56) in ambient atmosphere (Figure 3.13 a and b).

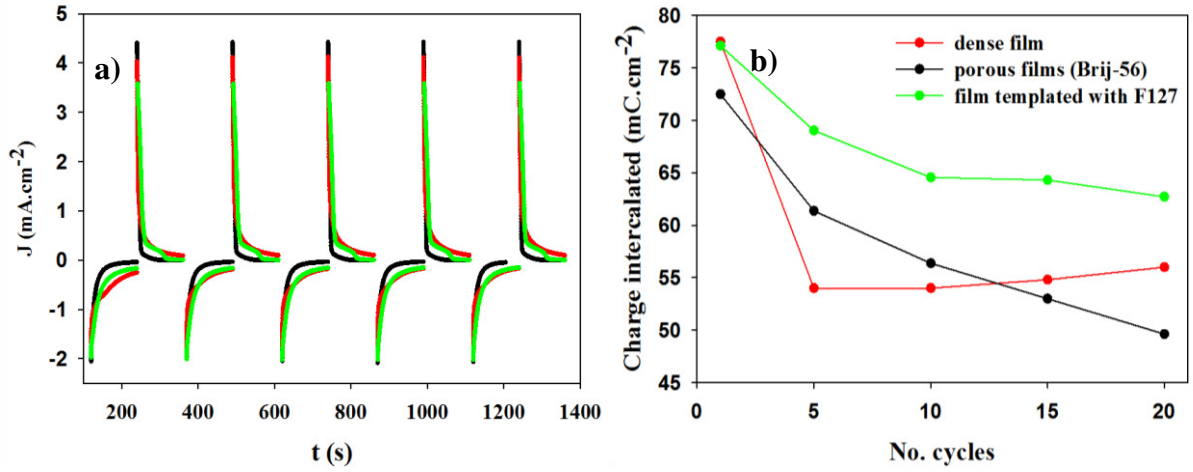

Figure 3.12: a) Chronoamperometric graphs of five consecutive cycles of the dense (red graph), porous (Brij-56) and the film templated with F217 b) charge capacity evolution with cycling of the three different films. Each point corresponds to the mean value of two measurements. The values were normalized according to the k-ratio determined in Table 3.5. The experiments were conducted at ambient atmosphere

Raman spectra show that before Li^+ intercalation the two films exhibit mainly two wide peaks in the high wavelength region. A broad and multicomponent peak (500-850 cm^{-1}) is attributed to the stretching vibrations of W-O (bridging/terminal W-OH) and a single band (around 950 cm^{-1}) is attributed to W=O bonds [46-49].

The broadness of the peaks and the presence of W=O bonds (which are absent in crystalline materials [46, 48, 50] designate the amorphous nature of the two films.

The network linkage looks somewhat different in the two films: the ratio of various W-O bands in the range 500-850 cm^{-1} is different and the mesoporous film exhibits an extra peak at 558 cm^{-1}. Overall, the different W-O peaks appear more distinctly in the mesoporous film in respect to the dense, which is attributed to the high surface to bulk ratio. Those W-O bonds should therefore be preferentially located at the surface of the material.

The peak at 780 cm^{-1} is attributed to the antisymmetric stretching vibration of W-O-W bonds [51]. Different clusters (W_2O_6 and W_3O_8 according to [52] presumably exist on the surface of the films and their stretching mode of terminal W-O bonds give rise to the peak at 697/692 cm^{-1}. The band at 639 cm^{-1} is attributed to the lattice phonon vibrations of $WO_3(H_2O)_x$ [53]. This band is stronger in mesoporous film (633 cm^{-1}), confirming its higher degree of hydration. No information was found in the literature regarding the peak at 558 cm^{-1} in the spectrum of the mesoporous film. We presume that this peak originates from longer W-O bonds (curved surface in the pores) associated with water molecules [54].

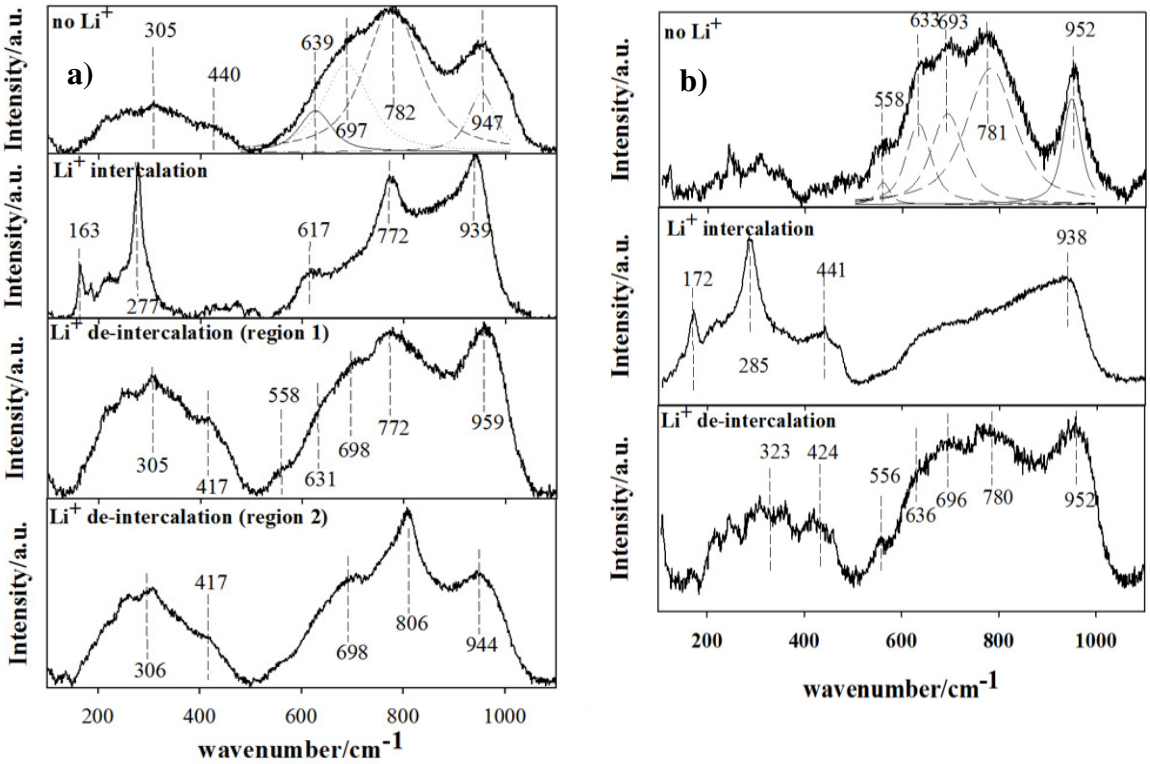

Figure 3.13: Raman spectra of a a) dense and a b) porous film before and after Li^+ intercalation and de-intercalation

In the low wavelength region (100-500 cm^{-1}) dense film (and to a lesser extend mesoporous film) possesses a broad peak centered at around 300 cm^{-1} related to W^{4+}-O bonds and a small band located at 440 cm^{-1} assigned to the W^{5+}=O vibration. This implies that the dense film is defined by WO_{3-x} formula and thus it contains W atoms at different valence states (W^{4+},W^{5+},W^{6+}) [46, 48, 49, 55].

Upon Li^+ intercalation (Figure 3.13 a and b), in the low wavelength region, Li^+ cations induce the appearance of distinct peaks (171/164 and 287/278 cm^{-1}) in both films, attributed to the stretching (ν) and bending vibrations (δ) of O-W-O bonds in M_xWO_3 materials [29, 46].

However, a different intercalation behavior of Li cations between the two films appears in the high wavelength region (500-850 cm^{-1}). In the mesoporous film, Li^+ cations disrupt the W-O lattice bonds located at the surface of the pores, as evidenced by the overall diminution of the broad band in the 500-850 cm^{-1} region.

In the dense film, the peaks at 782 cm^{-1} (antisymmetric stretching vibration of W-O-W) and 639 cm^{-1} (lattice vibrations of the hydrated oxide $WO_3.xH_2O$) slightly shift to lower wavelengths (772/617 cm^{-1}) but they remain intact upon lithium intercalation. Contrarily, the peak at 697 cm^{-1}, previously assigned to the terminal oxygens of surface clusters, vanishes after lithium intercalation.

These observations suggest that the cations not only reside in the cavities created by the perovskite-like structure of tungsten oxide but they also react with bonds and clusters on

the surface of the two films. These interactions become more pronounced in the porous film, as a result of its high surface area. The latter observation might explain the progressive degradation of the porous film with cycling as previously stated (Figure 3.12 b).

The interaction of the inorganic network with the intercalated species is already documented in the literature. For example, J. V. Gabrusenoks et al. [54] the intercalated cations react with the host's bridging oxygens by breaking network's W-O-W chains and creating new W=O bonds [28, 34, 50, 56-58] according to the equation:

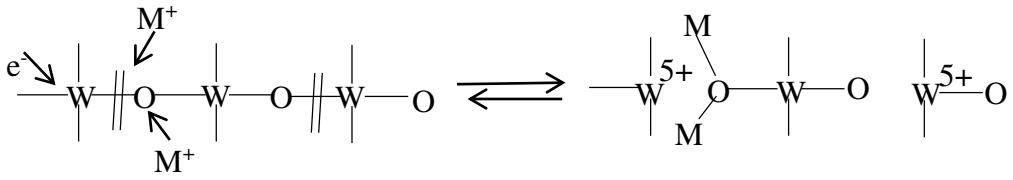

Contrarily, Ohtsuka et al. [59] based on their Raman and infrared findings, claim that coloration originates from the reaction of W=O bonds with the cations (H^+) and the subsequent formation of colored W^{5+}-OH, but this hypothesis was ruled out in later publications [57]. H. Zhang et al. [34] supported that upon electrons and cations insertion, two W=O terminal groups react together in order to produce W^{5+}-O-W^{5+} colored centers and M_2O (Li_2O and H_2O in lithium and proton media respectively). Others [46, 60] suggested that cations react with the bridging oxygens at low intercalated charge but at higher amounts they react with W=O as well. Interestingly, the W=O bands in our systems do not disappear upon Li^+ intercalation as stated by others [46, 60]. They only slightly shift to lower wavelengths in both cases (dense film from 947 to 939 cm^{-1} and mesoporous film from 952 to 938 cm^{-1}) probably due to the presence of the cations which weaken the strength of the double bond. This displacement, is reversible in both films after lithium extraction.

It is worth noting that no peaks attributed to Li-O bonds appear in the spectra of the two films as already inferred in the literature [46], even though it is already proposed that the cations affect network vibrations [28, 29, 46, 56] instead of residing only within the lattice channels. Bueno et al. [46] support that, at high amounts of lithium insertion, there is a very weak interaction (W^{5+}-O $\leftarrow$ Li^+) between the lithium ions and the network, which immobilizes the ions inside the film (although Li-O bond is not detectable by Raman). Our observation of disappearance of the network's vibrations upon lithium intercalation, corroborates with this suggestion.

Nevertheless, de-insertion of the Li^+ cations should revert the films to their initial state.

In the case of the mesoporous film (Figure 3.13 b) the spectrum after one complete cycle looks very much alike to the one before the electrochemical insertion, in accordance with the recovered transparency and reversibility values in Table 3.7.

In the dense film, de-intercalation is not homogeneous and two regions co-exist with different structural characteristics (Figure 3.13 a). The spectrum acquired in the region 1 looks alike the initial one, before any lithium intercalation. However, in the low wavelength

region (200-400 cm^{-1}) the broad peak around 300 cm^{-1} re-appears with higher intensity, indicating that some reduced tungsten atoms remain inside. This is in accordance with previous observations and the permanent coloration of the film after the measurement.

In the region 2, a new phase is detected (Figure 3.13 a). This spectrum resembles to a great extent with the ones reported for lithiated tungsten oxide films at the initial steps of crystallization [35, 46]. From these references, such a spectrum stems from Li_xWO_3 crystallites. It is likely therefore, that the insertion of lithium cations in this film increases the ordering degree of tungsten oxide resulting in irreversible bronze crystallites (Li_xWO_3) [61]. This phenomenon however, is not observed in the porous films. Based on earlier discussions we presume that porous films are highly amorphous while the dense films are closer to the crystallinity threshold.

All the electrochemical measurements presented so far were realized under ambient atmosphere in the presence of humidity. Moreover, the mesoporous films contain a significant amount of water molecules as a result of their porous nature (see infrared spectrum in Figure 3.8). The role of water in the performance of the films has been studied by many researchers. For example it was reported in the literature that the presence of free water in the $LiClO_4$/PC (propylene carbonate) electrolyte, or the use of water-rich films increases the diffusion co-efficient of the intercalated species in a value range approaching the ***proton*** diffusion co-efficients (10^{-7}-10^{-10} cm^2/s) rather than ***lithium*** (10^{-11}-10^{-13} cm^2/s) [41]. This suggests that a part of the intercalated species is constituted by protons from the water molecules and not from the lithium cations. Also it was proposed that the abundance of W-OH groups in porous films is also affecting their electrochemical performance. It was suggested that during lithium intercalation, exchange reactions might occur between the Li^+ and the W-OH groups. This reaction occurs until all the available W-OH groups are exhausted and protons are produced in exchange of lithium cations [41].

Others [43], concluded that the higher the water content is in the electrolyte, the conductivity of the electrolyte increases along with the switching kinetics. In our case, we measured the water content of the $LiClO_4$/PC by the Karl-Fischer technique and the results are presented in Table 3.9.

As it is shown in the table, the amount of water in the electrolyte which was prepared in ambient atmosphere is substantial and it increases even more after an extended electrochemical activity. It's not easy to determine when the electrolyte is considered anhydrous or wet. For example, O. Pyper et al. [29] suggested based on Raman studies that the addition of 500 ppm H_2O does not alter the intercalation of lithium cations while others [43] considered anhydrous the electrolyte which contained 100 ppm of H_2O.

Table 3.9: Water content in the $LiClO_4$/PC electrolyte measured by the Karl-Fischer technique

Electrolyte ($LiClO_4$/PC)	H_2O content (ppm)
Old batch stored in ambient atmosphere	1294
Fresh batch stored in ambient atmosphere	844
After an extended electrochemical measurement at ambient atmosphere	1735
After storing for 3 days in molecural sieves	24
After and extended electrochemical measurement where the electrolyte was stored in molecular sieves and the cell was assembled under Ar atmosphere	604

The influence of water in the electrochemical properties of the films was further corroborated by treating the dense films in different temperatures (Figure 3.14 a): 170ºC which still contains a significant amount of water, 250ºC and 300ºC which are almost anhydrous. As it is evidenced from Figure 3.14 b, the increase of the water content in the structure of the dense film, considerably improves the reversibility of the films.

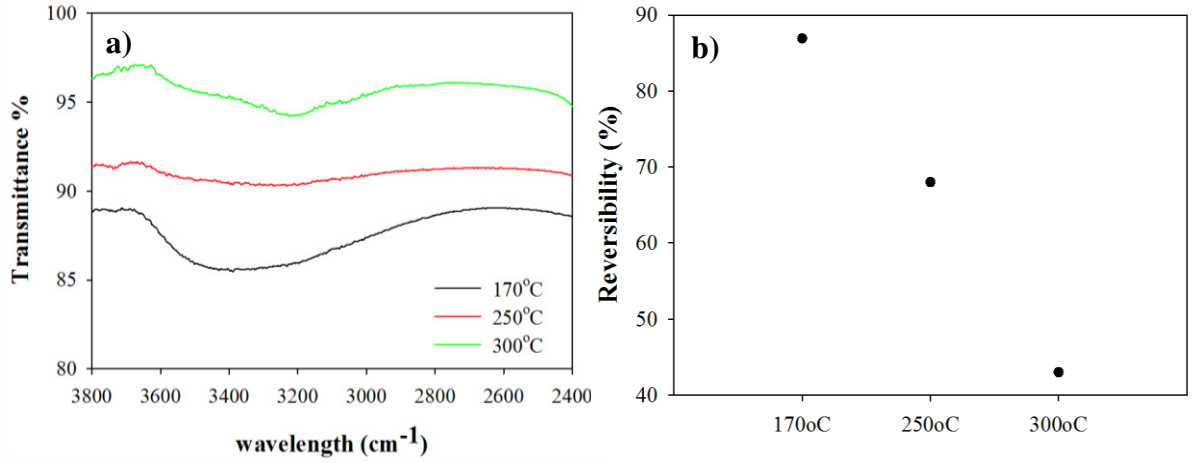

Figure 3.14: IR spectra for the dense films which were thermally treated at 170ºC (black line), 250ºC (red line) and 300ºC (green line). The peak depicts the hydroxyl and water bands b) Plot of reversibilities against the treated temperature for the dense film

Effect of water traces: experiments conducted in glovebox

In order to avoid the interference of atmospheric water in the electrochemical performance of the films, we also conducted cyclic voltammetry and chronoamperometry in a glovebox filled with Ar. Prior the experiment, the films were placed for five minutes in a vacuum chamber, to eliminate the free water and the oxygen. In this paragraph, only the results of the dense and the porous film (templated with Brij-56) will be discussed.

Figure 3.15 presents the cyclic voltammograms of the dense and the porous films which were conducted in the glovebox. The dense film (Figure 3.15 a and b) suffers from a slight irreversibility in the first cycle (more noticeable in the magnified plot in Figure 3.15 b), while the porous film (Figure 3.15 c) is well persistent since the first cycle. Moreover, the

porous film attains a higher current during the measurement, which indicates its higher conductivity due to its more open structure. Additionally, the extra anodic peak at higher voltages previously observed in ambient atmosphere is missing, confirming the assumption that the origin of the peak was stemming from the participation of the free water in the pores of the film and in the electrolyte. It should also be mentioned that when the film was not adequately deaerated in the vacuum chamber (retention time <5mins), then the second anodic peak was apparent again.

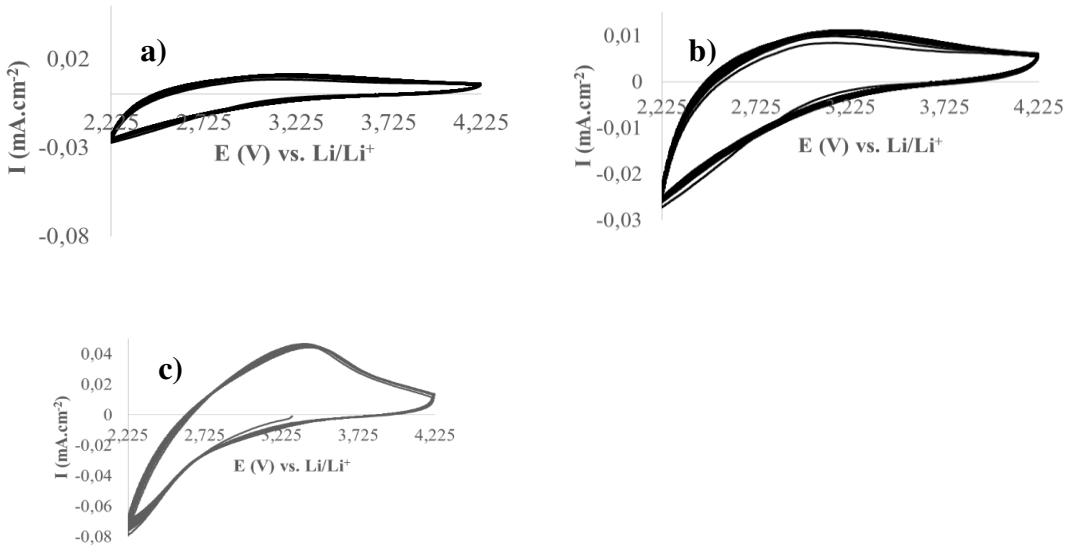

Figure 3.15: Cyclic voltammograms conducted in the glovebox of a a) dense film b) same voltammogram as a) but magnified and c) porous film

Surprisingly, the chronoamperometric measurements in a controlled atmosphere revealed different trend for the two films compared to the ones conducted in ambient atmosphere.

Figure 3.16 a and Table 3.10 show that the porous films repeatedly exhibit slower switching kinetics compared to the dense film in contrast to the previously mentioned results and other studies which stated that porosity accelerates the intercalation and de-intercalation of cations inside the films. This controversial observation might be attributed to the substantial higher lithium capacity of the porous film (see Table 3.10) which probably creates a barrier in the interface between the electrolyte and the film. Nevertheless, the TEM micrograph in

Figure 3.16 b, reveals that porosity is sustainable after twenty consecutive lithium insertions and de-insertions. Based on the micrograph and the fast Fourier transformation pattern in the inset, it is concluded that porosity is still periodically structured, however, the pores on the surface of the film are randomly oriented and the pairs of selectively oriented spots in the FFT pattern in Figure 3.7 d were replaced by a diffused circle in the pattern of Figure 3.16 b.

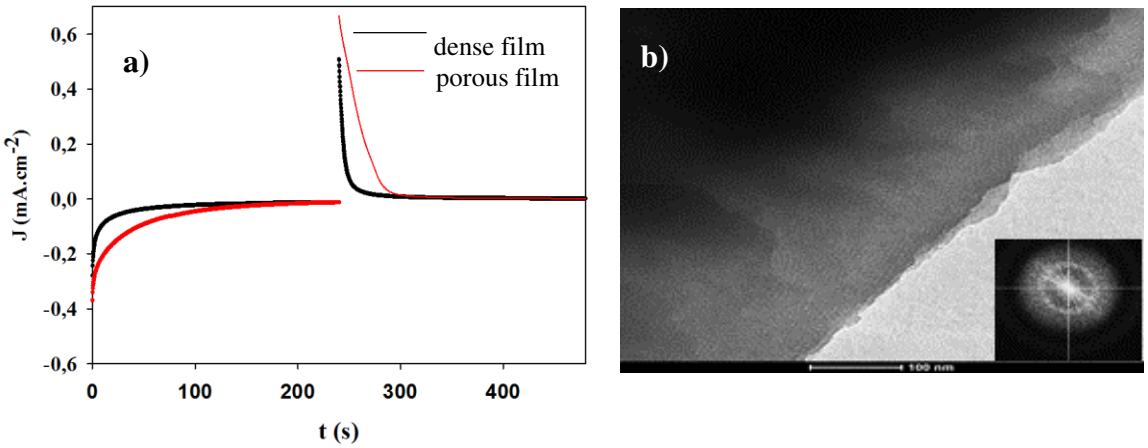

Figure 3.16: a) Chronoamperometric measurements of a dense and a porous film conducted in the glovebox b) TEM micrograph of a porous film after 20 consecutive cycles along with its FFT (Fast Fourier Transformation) pattern

Table 3.10: Electrochromic characteristics of the dense and porous film as calculated from the chronoamperometric measurements conducted in an Ar-filled glovebox

Sample	Charge capacity ($mC.cm^{-2}$)[1]	Normalised charge capacity ($mC.cm^{-2}$)[2]	R%	t_{in} (s)	$t_{de\text{-}int}$ (s)	$\Delta T\%_{550}$[3]	η_{550} (cm^2/C)[3]
Dense film	3.9±1.3	3.9±1.3	52±26	61±20	11±2	4,6	11,6
Porous film	10.7±0.5	26.8±7.1	93±4	141±39	44±9	27,2	24,6

[1] charge capacities were calculated from the 1st cycle of chronoamperometric measurements
[2] standard deviations for the normalized values and the reversibilities were calculated according to the formula $\frac{Dz}{z} = \sqrt{(\frac{Da}{a})^2 + (\frac{Db}{b})^2 + (\frac{Dc}{c})^2}$ for an equation $z \pm Dz = \frac{(a \pm Da).(b \pm Db)}{c \pm Dc}$
[3] calculated from the 20th cycle

As it is evident from the UV-visible spectra in Figure 3.17 and in Table 3.10 the most efficient properties in respect to reversibility, optical contrast and coloration efficiency stemmed from the porous film due to its higher surface to bulk ratio. While this film exhibits a significant variation of optical contrast and optical efficiency ranging from 6-40% and 10-52 cm^2/C respectively, the corresponding properties for the dense film remain somewhat constant through the whole optical range (6% and 14-18 cm^2/C). Even though the films exhibit their maximum performance in wavelengths over 650 nm, 550 nm was selected as a reference in this study due to the maximum human eye sensitivity at this wavelength [62].

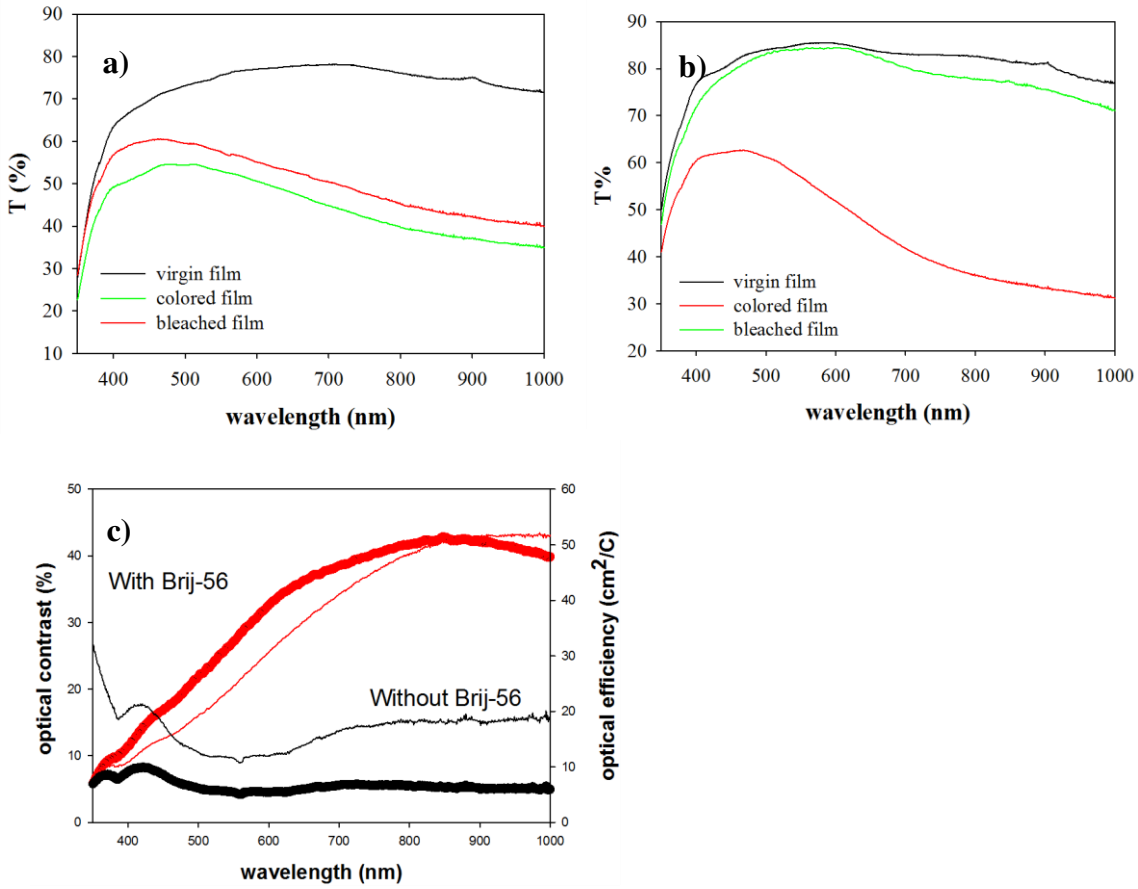

Figure 3.17: UV spectra of a) dense film and a b) porous film after cycling for 19th cycles and c) plots of the optical contrast (thick lines) and optical efficiency (thin lines) in the whole spectrum (300-1000 nm). Red plots illustrate the results from the porous films and black plots from the dense films

3.4 Conclusions

In this chapter, porous and dense amorphous films have been prepared with the dip-coating technique. APTA (acetylated peroxo tungstic acid) and Brij-56 have been used as a tungsten precursor and structure directing agent respectively. In some experiments a large triblock co-polymer (F127) has been used as a structure directing agent instead. A long range organized architecture is obtained with Brij-56 with pores sizes of about 2 nm and wall thicknesses of 3 nm. With F127, a worm-like architecture is obtained in the uncalcined film, however with further thermal annealing the porous structure is collapsed. Based on ellipsometric measurements, the calcined Brij-56 templated films contain 23% of porosity while F127 templated films contain 12% of porosity.

The main drawback of these films is the occurence of cracks and the inconsistent thickness. Unfortunately, all the attempts did not lead to any improvement of the quality of the films.

We selected to work with amorphous rather than crystalline films. Based on our results and in accordance with the literature, crystalline films possess inferior optical and

electrochemical properties due to their dense and rigid structure [36]. Even though they exhibit slightly better reversibility, the growth of crystallites is detrimental for porosity.

By treating the dense and porous films at different thermal conditions, we observed that the presence of surfactant delays the crystallization of the oxide network. While dense films begin to crystallize after 2h at 300ºC the porous film remains amorphous at 350ºC/2h. This effect is already cited in the literature [4, 11] and it might be associated with the decrease of the W-O groups nucleation rate, due to interactions of the template and the inorganic matrix [26].

IR and Raman spectra revealed that the porous films are highly hydrated and characterized by the general formula $WO_{3-x-y}OH_x.yH_2O$, while dense films are much less hydrated. We showed that the atmospheric water in the electrolyte and the abundance of water molecules and hydroxyls in the porous films, modify the electrochemical reaction. Probably protons are intercalating and de-intercalating as well and/or W-OH groups release protons in exchange of lithium cations. This effect results in the appearance of a second anodic peak in the cyclic voltammograms in ambient atmosphere, which disappears when the experiments are conducted in an argon-filled glovebox. The implication of water in the electrochemical processes, improves the switching kinetics, and the reversibility of the films in ambient atmosphere. On the contrary, when the experiments were conducted in a glovebox, porous films exhibited much slower kinetics compared to the dense films. This is probably due to the lack of excess water in the electrolyte, but also to the substantially higher charge capacity of the porous films which might create a barrier in the interface between the electrolyte and the film. According to the values in Table 3.10 and despite the fact that the porous films consists of almost 2.5 times less W (based on the k-ratio values in Table 3.5) compared to the dense films, the former intercalate almost 3 times more lithium cations than the latter. This infers than the flat surface of the dense film does not permit the penetration of the cations in the interior of the films.

Finally, we performed Raman spectra in ambient environment before, during intercalation and after lithium de-intercalation. It was found that lithium cations, not only reside in the channels of the perovskite-like channels of WO_3 but they interact with the surface of the films by disrupting the inorganic network. This is more distinct in the porous films, whose surface/bulk ratio is higher. There are different theories in the literature regarding these interactions, some of them involving the breakage of W-O-W bonds or the condensation of two W=O groups and the subsequent formation of coloring centers and M_2O (in our case $M=Li^+$). The irreversibility of the dense films was also noticeable in Raman spectra. More specifically, a new phase was detected which according to the literature was attributed to the formation of Li_xWO_3 crystallites [35, 46]. This suggests that the intercalation of lithium cations can increase the degree of crystallinity of the films, but further investigations should be carried out in order to confirm this assumption.

3.5 References for Chapter 3

[1] Z.-M. Qi, H.-S. Zhou, T. Watanabe, I. Honma, Synthesis, characterization and optical gas-sensing application of block copolymer templated mesostructured peroxopolytungstic acid films, Journal of Materials Chemistry, 14 (2004) 3540-3547.

[2] C.J. Brinker, A.J. Hurd, P.R. Schunk, G.C. Frye, C.S. Ashley, Review of sol-gel thin film formation, Journal of Non-Crystalline Solids, 147–148 (1992) 424-436.

[3] Y. Zhang, J. Yuan, J. Le, L. Song, X. Hu, Structural and electrochromic properties of tungsten oxide prepared by surfactant-assisted process, Solar Energy Materials & Solar Cells, 93 (2009) 1338-1344.

[4] A. Cremonesi, Y. Djaoued, D. Bersani, P. Lottici, Micro-Raman spectroscopy on polyethylene-glycol assisted sol–gel meso and macroporous WO3 thin films for electrochromic applications, Thin Solid Films, (2007).

[5] S. Sallard, T. Brezesinski, B.M. Smarsly, Electrochromic Stability of WO_3 Thin Films with Nanometer-Scale Periodicity and Varying Degrees of Crystallinity, The Journal of Physical Chemistry C, 111 (2007) 7200-7206.

[6] J. Dewalque, Templated TiO2 mesoporous films used as highly efficient photoelectrode in Dye-Sensitized Solar Cells, phD dissertation, chapter 2, (2013).

[7] J. Yuan, Y. Zhang, J. Le, L. Song, X. Hu, New templated method to synthesize electrochromic mesoporous tungsten oxides, Materials Letters, 61 (2007) 1114-1117.

[8] D. Grosso, F. Cagnol, G.J.d.A.A. Soler-Illia, E.L. Crepaldi, H. Amenitsch, A. Brunet-Bruneau, A. Bourgeois, C. Sanchez, Fundamentals of Mesostructuring Through Evaporation-Induced Self-Assembly, Advanced Functional Materials, 14 (2004) 309-322.

[9] L.G. Teoh, Y.M. Hon, J. Shieh, W.H. Lai, M.H. Hon, Sensitivity properties of a novel NO_2 gas sensor based on mesoporous WO_3 thin film, Sensors and Actuators B: Chemical, 96 (2003) 219-225.

[10] J. Dewalque, Templated TiO2 mesoporous films used as highly efficient photoelectrode in Dye-Sensitized Solar Cells, PhD dissertation, (2013).

[11] W. Cheng, E. Baudrin, B. Dunn, J.I. Zink, Synthesis and electrochromic properties of mesoporous tungsten oxide, Journal of Materials Chemistry, 11 (2001) 92-97.

[12] W. Wang, Y. Pang, S.N.B. Hodgson, Preparation, characterisation and electrochromic property of mesostructured tungsten oxide films via a surfactant templated sol–gel process from tungstic acid, Journal of Sol-Gel Science and Technology, 54 (2010) 19-28.

[13] W. Wang, Y. Pang, S.N.B. Hodgson, Design and fabrication of bimodal meso-mesoporous WO_3 thin films and their electrochromic properties, Journal of Materials Chemistry, 20 (2010) 8591.

[14] W. Wang, Y. Pang, S.N.B. Hodgson, XRD studies of thermally stable mesoporous tungsten oxide synthesised by a templated sol–gel process from tungstic acid precursor, Microporous and Mesoporous Materials, 121 (2009) 121-128.

[15] T. Brezesinski, D.F. Rohlfing, S. Sallard, M. Antonietti, B.M. Smarsly, Highly crystalline WO3 thin films with ordered 3D mesoporosity and improved electrochromic performance, Small, 2 (2006) 1203-1211.

[16] Y. Wan, Y. Shi, D. Zhao, Designed synthesis of mesoporous solids via nonionic-surfactant-templating approach, Chemical Communications (Cambridge, United Kingdom), (2007) 897-926.

[17] C. Sanchez, C. Boissière, D. Grosso, C. Laberty, L. Nicole, Design, Synthesis, and Properties of Inorganic and Hybrid Thin Films Having Periodically Organized Nanoporosity†, Chemistry of Materials, 20 (2008) 682-737.

[18] E.L. Runnerstrom, A. Llordes, S.D. Lounis, D.J. Milliron, Nanostructured electrochromic smart windows: traditional materials and NIR-selective plasmonic nanocrystals, Chemical Communications, 50 (2014) 10555-10572.

[19] B.W. Faughnan, R.S. Crandall, Electrochromic displays based on tungsten oxide, Topics in Applied Physics, 40 (1980) 181-211.

[20] D. Perednis, O. Wilhelm, S.E. Pratsinis, L.J. Gauckler, Morphology and deposition of thin yttria-stabilized zirconia films using spray pyrolysis, Thin Solid Films, 474 (2005) 84-95.

[21] M. Deepa, M. Kar, D.P. Singh, A.K. Srivastava, S. Ahmad, Influence of polyethylene glycol template on microstructure and electrochromic properties of tungsten oxide, Solar Energy Materials and Solar Cells, 92 (2008) 170-178.

[22] R. Neagu, D. Perednis, A. Princivalle, E. Djurado, Initial Stages in Zirconia Coatings Using ESD, Chemistry of Materials, 17 (2005) 902-910.

[23] L.M. Bertus, C. Faure, A. Danine, C. Labrugere, G. Campet, A. Rougier, A. Duta, Synthesis and characterization of WO3 thin films by surfactant assisted spray pyrolysis for electrochromic applications, Materials Chemistry and Physics, 140 (2013) 49-59.

[24] J. Denayer, G. Bister, P. Simonis, P. Colson, A. Maho, P. Aubry, B. Vertruyen, C. Henrist, V. Lardot, F. Cambier, R. Cloots, Surfactant-assisted ultrasonic spray pyrolysis of nickel oxide and lithium-doped nickel oxide thin films, toward electrochromic applications, Applied Surface Science, 321 (2014) 61-69.

[25] J. Denayer, P. Aubry, G. Bister, G. Spronck, P. Colson, B. Vertruyen, V. Lardot, F. Cambier, C. Henrist, R. Cloots, Improved coloration contrast and electrochromic efficiency of tungsten oxide films thanks to a surfactant-assisted ultrasonic spray pyrolysis process, Solar Energy Materials and Solar Cells, 130 (2014) 623-628.

[26] N.-L. Wu, S.-Y. Wang, I.A. Rusakova, Inhibition of Crystallite Growth in the Sol-Gel Synthesis of Nanocrystalline Metal Oxides, Science, 285 (1999) 1375-1377.

[27] R. Ostermann, B. Smarsly, Does mesoporosity enhance thin film properties? A question of electrode material for electrochromism of WO_3, Nanoscale, 1 (2009) 266-270.

[28] G. Leftheriotis, S. Papaefthimiou, P. Yianoulis, The effect of water on the electrochromic properties of WO3 films prepared by vacuum and chemical methods, Solar Energy Materials & Solar Cells, 83 (2004) 115-124.

[29] O. Pyper, A. Kaschner, C. Thomsen, In situ Raman spectroscopy of the electrochemical reduction of WO3 thin films in various electrolytes, Solar Energy Materials and Solar Cells, 71 (2002) 511-522.

[30] P. Yang, D. Zhao, D.I. Margolese, B.F. Chmelka, G.D. Stucky, Generalized syntheses of large-pore mesoporous metal oxides with semicrystalline frameworks, Nature, 396 (1998) 152-155.

[31] J. Dewalque, R. Cloots, F. Mathis, O. Dubreuil, N. Krins, C. Henrist, TiO2 multilayer thick films (up to 4 [small micro]m) with ordered mesoporosity: influence of template on the film mesostructure and use as high efficiency photoelectrode in DSSCs, Journal of Materials Chemistry, 21 (2011) 7356-7363.

[32] M. Deepa, D.P. Singh, S.M. Shivaprasad, S.A. Agnihotry, A comparison of electrochromic properties of sol–gel derived amorphous and nanocrystalline tungsten oxide films, Current Applied Physics, 7 (2007) 220-229.

[33] S.-H. Lee, M.J. Seong, H.M. Cheong, E. Ozkan, E.C. Tracy, S.K. Deb, Effect of crystallinity on electrochromic mechanism of LixWO3 thin films, Solid State Ionics, 156 (2003) 447-452.

[34] J.G. Zhang, D.K. Benson, C.E. Tracy, S.K. Deb, A.W. Czanderna, C. Bechinger, Chromic Mechanism in Amorphous WO_3 Films, Journal of the Electrochemical Society, 144 (1997) 2022-2026.

[35] M. Deepa, A.G. Joshi, A.K. Srivastava, S.M. Shivaprasad, S.A. Agnihotry, Electrochromic Nanostructured Tungsten Oxide Films by Sol-gel: Structure and Intercalation Properties, Journal of the Electrochemical Society, 153 (2006) C365-C376.

[36] B.W. Faughnan, R.S. Crandall, Electrochromic displays based on WO_3, in: J.I. Pankove (Ed.) Display Devices, Springer Berlin Heidelberg1980, pp. 181-211.

[37] M. Deepa, T.K. Saxena, D.P. Singh, K.N. Sood, S.A. Agnihotry, Spin coated versus dip coated electrochromic tungsten oxide films: Structure, morphology, optical and electrochemical properties, Electrochim. Acta, 51 (2006) 1974-1989.

[38] M. Deepa, A.K. Srivastava, S.A. Agnihotry, Influence of annealing on electrochromic performance of template assisted, electrochemically grown, nanostructured assembly of tungsten oxide, Acta Materialia, 54 (2006) 4583-4595.

[39] S.-H. Baeck, K.-S. Choi, T.F. Jaramillo, G.D. Stucky, E.W. McFarland, Enhancement of photocatalytic and electrochromic properties of electrochemically fabricated mesoporous WO3 thin films, Advanced Materials (Weinheim, Germany), 15 (2003) 1269-1273.

[40] W. Wang, Y. Pang, S.N.B. Hodgson, On key factors for the fabrication of mesoporous tungsten oxide films from tungstic acid, Journal of Sol-Gel Science and Technology, 58 (2010) 135-141.

[41] J.G. Zhang, C.E. Tracy, D.K. Benson, S.K. Deb, The influence of microstructure on the electrochromic properties of lithium tungsten oxide (Li_xWO_3) thin films. Part I. Ion diffusion and electrochromic properties, J. Mater. Res., 8 (1993) 2649-2656.

[42] D.-J. Kim, S.-I. Pyun, Hydrogen transport through rf-magnetron sputtered amorphous WO3 film with three kinds of hydrogen injection sites, Solid State Ionics, 99 (1997) 185-192.

[43] O. Bohnke, C. Bohnke, G. Robert, B. Carquille, Electrochromism in WO3 thin films. I. LiClO4-propylene carbonate-water electrolytes, Solid State Ionics, 6 (1982) 121-128.

[44] M.F. Saenger, T. Höing, B.W. Robertson, R.B. Billa, T. Hofmann, E. Schubert, M. Schubert, Polaron and phonon properties in proton intercalated amorphous tungsten oxide thin films, Physical Review B, 78 (2008) 245205.

[45] K.-H. Heckner, A. Kraft, Similarities between electrochromic windows and thin film batteries, Solid State Ionics, 152–153 (2002) 899-905.

[46] P.R. Bueno, F.M. Pontes, E.R. Leite, L.O.S. Bulhões, P.S. Pizani, P.N. Lisboa-Filho, W.H. Schreiner, Structural analysis of pure and LiCF3SO3-doped amorphous WO_3 electrochromic films and discussion on coloration kinetics, Journal of Applied Physics, 96 (2004) 2102-2109.

[47] S.-H. Lee, H.M. Cheong, C.E. Tracy, A. Mascarenhas, J.R. Pitts, G. Jorgensen, S.K. Deb, Alternating current impedance and Raman spectroscopic study on electrochromic a-WO3 films, Applied Physics Letters, 76 (2000) 3908-3910.

[48] A. Baserga, V. Russo, F. Di Fonzo, A. Bailini, D. Cattaneo, C.S. Casari, A. Li Bassi, C.E. Bottani, Nanostructured tungsten oxide with controlled properties: Synthesis and Raman characterization, Thin Solid Films, 515 (2007) 6465-6469.

[49] S.-H. Lee, H.M. Cheong, C.E. Tracy, A. Mascarenhas, D.K. Benson, S.K. Deb, Raman spectroscopic studies of electrochromic a-WO3, Electrochimica Acta, 44 (1999) 3111-3115.

[50] P. Delichere, P. Falaras, M. Froment, A. Hugot-Le Goff, B. Agius, Electrochromism in anodic WO3 films I: Preparation and physicochemical properties of films in the virgin and coloured states, Thin Solid Films, 161 (1988) 35-46.

[51] B.M. Weckhuysen, J.-M. Jehng, I.E. Wachs, In Situ Raman Spectroscopy of Supported Transition Metal Oxide Catalysts: $^{18}O_2$–$^{16}O_2$ Isotopic Labeling Studies, The Journal of Physical Chemistry B, 104 (2000) 7382-7387.

[52] W. Weltner Jr, D. McLeod Jr, Spectroscopy of tungsten oxide molecules in neon and argon matrices at 4° and 20°K, Journal of Molecular Spectroscopy, 17 (1965) 276-299.

[53] M.F. Daniel, B. Desbat, J.C. Lassegues, B. Gerand, M. Figlarz, Infrared and Raman study of WO_3 tungsten trioxides and $WO_3.xH_2O$ tungsten trioxide tydrates, Journal of Solid State Chemistry, 67 (1987) 235-247.

[54] J.V. Gabrusenoks, P.D. Cikmach, A.R. Lusis, J.J. Kleperis, G.M. Ramans, Electrochromic colour centres in amorphous tungsten trioxide thin films, Solid State Ionics, 14 (1984) 25-30.

[55] S.-H. Lee, H.M. Cheong, C.E. Tracy, A. Mascarenhas, A.W. Czanderna, S.K. Deb, Electrochromic coloration efficiency of a-WO_{3-y} thin films as a function of oxygen deficiency, Applied Physics Letters, 75 (1999) 1541-1543.

[56] B. Orel, U.O. Krasovec, N. Groselj, M. Kosec, G. Drazic, R. Reisfeld, Gasochromic behavior of sol-gel derived Pd doped peroxopolytungstic acid (W-PTA) nano-composite films, J. Sol-Gel Sci. Technol., 14 (1999) 291-308.

[57] J.L. Paul, J.C. Lassègues, Infrared Spectroscopic Study of Sputtered Tungsten Oxide Films, Journal of Solid State Chemistry, 106 (1993) 357-371.

[58] B. Orel, N. Grošelj, U.O. Krašovec, R. Ješe, A. Georg, IR Spectroscopic Investigations of Gasochromic and Electrochromic Sol-Gel—Derived Peroxotungstic Acid/Ormosil Composite and Crystalline WO_3 Films, Journal of Sol-Gel Science and Technology, 24 (2002) 5-22.

[59] T. Ohtsuka, N. Goto, N. Sato, Change of the anodic oxide films of tungsten during the electrochromic reaction, Journal of Electroanalytical Chemistry and Interfacial Electrochemistry, 287 (1990) 249-264.

[60] S.-H. Lee, H.M. Cheong, C. Edwin Tracy, A. Mascarenhas, R. Pitts, G. Jorgensen, S.K. Deb, Influence of microstructure on the chemical diffusion of lithium ions in amorphous lithiated tungsten oxide films, Electrochimica Acta, 46 (2001) 3415-3419.

[61] H. Kamal, A.A. Akl, K. Abdel-Hady, Influence of proton insertion on the conductivity, structural and optical properties of amorphous and crystalline electrochromic WO_3 films, Physica B: Condensed Matter, 349 (2004) 192-205.

[62] H.M.A. Soliman, A.B. Kashyout, M.S. El Nouby, A.M. Abosehly, Effect of hydrogen peroxide and oxalic acid on electrochromic nanostructured tungsten oxide thin films, International Journal of Electrochemical Science, 7 (2012) 258-271.

Chapter 4
Electrodeposition

4.1 Introduction and literature review

The electrodeposition process in ceramic materials involves the precipitation of insoluble MO_x on a surface where exchange of electrons takes place. In general, the oxidation state of a M^+ in a soluble precursor is modified through oxidation/reduction in order to form insoluble hydroxides or oxy-hydroxide phases on the surface of an electrode. In the special case where this process occurs in the presence of a surfactant then the precipitation could potentially take place around the micellar templates (Figure 4.1) [1]. Alternatively, the inorganic precursor precipitates through electrochemically induced local pH. More specifically, as O_2 and precursor counteranions or chelating agents (e.g. NO_3^- or H_2O_2) are reduced, OH^- is generated which catalyzes the hydrolysis and condensation of the inorganic precursor [1-3].

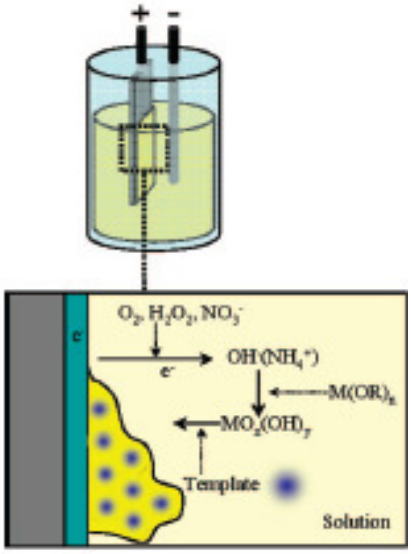

Figure 4.1 [1]: Mesophase formation in electrodeposition

Electrodeposition is frequently employed for the formation of mesostructured porous films. Some examples, are transition metal oxides such as ZnO [2, 4], WO_3 [5], MnO_2 [6, 7],

SnO_2 [3], Cu_2O [4], $Co(OH)_2$ [8], $Ni/Ni(OH)_2$ [9], $Ni(OH)_2$ [10], RuO_2 [11] and metals like Sn [12], Pt [13] .

In electrodeposition the nature of the amphiphiles plays a tremendous role in the formation of a mesophase. By selecting surfactants with the appropriate head groups the metal species can be strongly bound as counter ions on their surface enabling the hydrolysis and condensation of the precursor when a voltage is applied [2, 3]. It is worthy to mention that surfactants are spontaneously aggregate in micelles or self-assemblies on the surface of a substrate by surface forces (e.g. electrostatic interaction between surfactant head group and a surface charge, hydrophilicity of the surface etc.) creating solid-liquid interfaces below their critical micelle concentration [2, 3, 10]. For example lamellar ZnO mesostructures are obtained when $Zn(NO_3)_2$ is mixed with anionic surfactants such as SDS (sodium dodecyl sulfate), AOT (dioctyl sulfosuccinate sodium salt), DP (monododecyl phosphate) etc [2]. It appears that the $[Zn(H_2O)_4]^{2+}$ species interact with the anionic headgroups, thereby robust amphiphilic organic-inorganic assemblies emerge. Likewise, lamellar structures have been obtained with SDS and a peroxo tungsten complex at a specific potential (-0.5 V vs. Ag/AgCl) [5]. However, in both cases the mesophases were lacking of thermal stability and therefore solvent extraction was necessary in order to remove surfactant and preserve the mesoporous structure. Interestingly, the removal of SDS it can be accomplished easily as the interactions between the metal and the sulfate head groups disappear once the neutral MO_x is formed [3, 13]. On the other hand, no mesostructures were obtained with cationic surfactants of the general formula $C_nH_{2n+1}(CH_3)_3NBr$ such as CTAB (n=16) in ZnO films [2]. Other researchers worked with non-ionic surfactants as well [4, 6, 7]. In that case the selection of a suitable precursor is important since the precursor counter ions affect the solubility of the metal precursor (e.g. Cl^- and SO_4^{2-} transition metal salts do not dissolve in the presence of non-ionic surfactants [14]) the hydrophilicity of the surfactants and subsequently their mesostructure [6]. T. Xue et al. [6] prepared MnO_2 films with hexagonal and cubic mesostructures with P123 ($EO_{20}PO_{70}EO_{20}$) and F127 ($EO_{106}PO_{70}EO_{106}$) respectively where $MnAc_2$ was selected as a precursor. In that study however, the organization in both cases is not long-range. Apart from P123 and F127 other non-ionic surfactants have been successfully applied for the formation of different metal oxides as well namely Brij-56 ($C_{16}EO_{10}$) (ZnO, Cu_2O, MnO_2 , $Co(OH)_2$, $Ni/Ni(OH)_2$) [4, 7-9], Brij-76 ($C_{18}EO_{10}$) (ZnO, Cu_2O, Sn) [4, 12], Brij-78 ($C_{18}EO_{20}$) (ZnO, Cu_2O, Sn) [4, 12] $C_{16}EO_8$ (Sn) [12], or mixtures of ionic and non-ionic surfactants such as SDS/P123 ($Ni(OH)_2$) [10]. In the latter case, a conversion from lamellar into hexagonal mesophase was reported with the addition of the non-ionic P123 as a co-surfactant. A. Gomes et al. [15] investigated the influence of three surfactants (SDS, CTAB, Triton X100 ($C_{34}H_{62}O_{11}$) as additives in the electrodeposition of Zn (porosity was not studied in this publication). The authors found that the presence of surfactants in the plating solution reduces the current density of Zn deposition and shifts its reduction to more cathodic potentials. The explanation for this obstruction is the coverage of the electrode surface with the surfactant which decreases the nucleation rate and affects the nucleation mechanism [15].

The applied potential is another parameter which can determine the occurrence, the extent or the architecture of the mesophase as it defines the charge density of the depositing surface [3, 13]. For example, worm-like structures were obtained when SDS and a peroxide tungsten complex were used as a surfactant and a tungsten precursor respectively, at a potential of -0.2 V vs. Ag/AgCl while lamellar structure was the prevailed phase when the potential was increased at -0.5 V [5]. It has also been reported that when the applied potential is excessively high (too negative), then uncontrolled precipitation of MO_x occurs before an organized inorganic-organic interface is formed [2]. In other cases too negative potentials result in the precipitation of the metallic compound rather the oxide [4]. This threshold potential varies from metal to metal. For example, -1V vs. Ag/AgCl was suitable for the deposition of ZnO but a potential of -0.6 V was enough to induce the precipitation of Cu instead of Cu_2O [4].

Table 4.1: Preparation of electrodeposited WO_3 in the presence of surfactants

Precursor	Surfactant	Deposition potential	Thermal treatment	Crystallinity	Pores/structural characteristics	Reference
W mixed with H_2O_2	SDS	-0.2≤V vs. Ag/AgCl ≤-0.5	-----	N.A	Needle-like particles lamellar(-0.5V) or worm-like (-0.2V) mesostructure	[5]
W mixed with H_2O_2	PEG /CTAB	-0.45V vs. Ag/AgCl	100-500°C	Triclinic[1] (except the film treated at 100°C)	Spheres and needle-like particles interstitial porosity random templated pores in the as-deposited	[16]
W mixed with H_2O_2	SDS	-0.45V vs. Ag/AgCl	100-500°C	Orthorombic (250°C/ 500°C) Tetragonal $WO_{2.9}$ (100°C)[2]	Nanoparticles/ rods intersitial porosity	[17, 18]
W mixed with H_2O_2	PEG	-0.45V vs. Ag/AgCl	-----	Triclinic	rod-like structures spherical particles interstitial porosity	[19]

[1] the as-deposited film exhibits a triclinic structure
[2] the as-deposited film exhibits a hexagonal structure

The synthesis of electrodeposited templated tungsten oxide films with or without template has also been reported in the literature. Table 4.1 lists some of the efforts reported in the

literature to prepare porous tungsten oxide films in the presence of a structure directing agent.

From the table some interesting remarks can be derived: 1) the presence of surfactant influences the microstructure of tungsten oxide. One dimensional particles are produced even in their as-deposited state under certain circumstances [19]. These particles are not observed when surfactants are not present [20] 2) The surfactants in electrodeposition do not typically lead to templated-induced porosity but rather to interstitial porosity. However, it should be mentioned that interstitial porosity is also reported in films which have been prepared in the absence of a surfactant. For example, in the work of A.K. Srivastava et al. [20] a homogeneous crack-free granular structure has been observed with uniform distribution of pores. In this case, the authors used APTA (described in chapter 2) as a precursor where peroxo and acetylated groups were present. It is also mentioned that the acetyl and peroxy groups are not detected by infrared spectroscopy even in the as-deposited film, signifying that the precipitating species in electrodeposition are comprised by polytungstate ions rather than the initial precursor. This is also described in the following equation where elemental W in a peroxide solution is electrodeposited on a surface [21]:

$$W_2O_{11}^{2-} + (2+x)\,H^+ + xe^- \longrightarrow 2WO_3 + (8-x)/4\,O_2 + (2+x)/2\,H_2O$$

No further information about the involvement of the acetyl groups in the APTA precursor were found in the literature. On the other hand, in the work of M. Giannouli and G. Leftheriotis [21] mostly uniform and continuous films have been observed when W/H_2O_2 solution was deposited on a surface. The precursor in this case was devoid of acetyl groups and additionally the plating solution was stored in the fridge for 10 days before use. Therefore we believe that the acetyl groups in the work of A.K. Srivastava et al. [20] might be responsible for the granular morphology of the films. The pH of the plating solution is another parameter that has also been reported to affect the interstitial porosity of the electrodeposited films [22] 3) electrodeposition does not lead to the expected thermodynamic crystalline phases [23]. Moreover, Table 4.1 signifies that the presence of surfactants has also an impact on the occurring crystalline phase. For example, a hexagonal mixed with amorphous phase is detected when APTA is electrodeposited and then stabilized at 100°C [20]. On the other hand, a triclinic structure has been observed at 100°C when the starting solution contained PEG (see Table 4.1). Contrarily, a tetragonal $WO_{2.9}$ phase has been detected when SDS was used as a structure directing agent. According to the authors the latter crystalline phase which is very beneficial for intercalation applications is typically observed at temperatures above 1200 K [17].

In this chapter two different surfactants have been used in order to prepare electrodeposited mesoporous tungsten oxide films, a non-ionic surfactant (Brij-56 or Brij-C10) and an

anionic polymer (Poly(sodium 4-styrene sulfonate)) whose chemical formulas are presented in Figure 4.2.

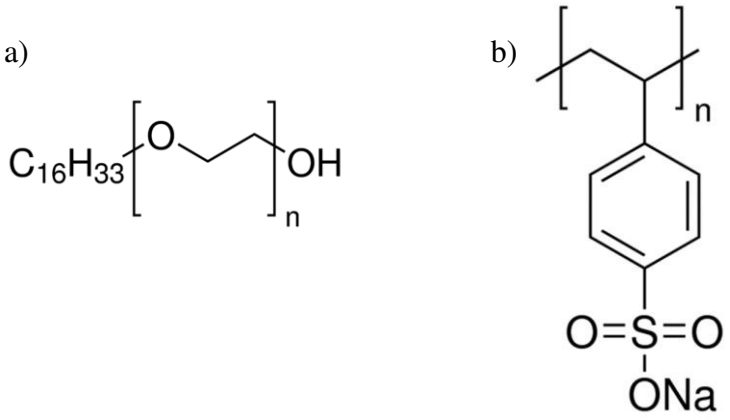

Figure 4.2: Chemical formulas of the templating agents used a) Brij-56 and b) PSS-Na

The experiments which are presented in this chapter encountered many problems: low coverage, no solid evidences of porosity, lack of reproducibility and low electrochemical properties. For this reason, the experiments will be briefly presented. Moreover, due to the insufficient electrochemical properties this part won't be discussed.

4.2 Experimental part

Brij-56 (Brij-C10, average Mn: 683, Sigma Aldrich), PSS-Na (Poly(sodium 4-styrene-)sulfonate, average Mw:70000, Sigma Aldrich) and APTA (see chapter 2) were used as templating agents and a tungsten precursor respectively. For the electrodeposited films, the APTA precursor remained stabilized in its aqueous solvent rather than precipitating as a solid by rotary evaporator. In that way, the need of ethanol as a re-dispersing agent was avoided in the plating solution.

For the plating solution with Brij-56, different amounts of Brij-56 were dissolved in water at 40ºC. After cooling down, 10 mL of APTA precursor were added and the yellow solution was stirred at room temperature for 1h before transfer in the electrochemical cell.

The three electrode configuration cell for the electrodeposition is presented in Figure 4.3 where the respective electrodes are annotated. As in the dip-coated experiments, all the films were deposited on pre-cleaned glass substrates (SnO_2:F coated glass substrates, TEC15, 15 Ω/sq, 2 cm x 2 cm x 2,2 mm, Dyesol). For the Brij-56 containing solutions, -0.35 V vs. Ag/AgCl was applied for a certain period of time, until a considerable amount of material is deposited on the surface (300-400 $mC.cm^{-2}$). The films exhibit a blue color during and right after the electrodeposition which fades out as soon as the films come in contact with air. After removal the films are rinsed with pure ethanol, dried in air and stabilized at 170ºC for 1h. Between electrodepositions the solution is mildly magnetically stirred and the counter electrode is rinsed with pure ethanol and dried in air. Finally the films are calcined at 300ºC for 1h with a ramp of 1ºC/min. Calcining at the same temperature as the mesoporous dip-coated films (350ºC/2h) resulted in crystalline films.

The films without any surfactant, have been treated at lower temperature (250ºC for 1h rather than 300ºC) to prevent crystallization occurrence. The effect of the surfactant in film crystallization has already been discussed in chapter 3.

Similarly with PSS-Na containing solutions and following the work of S-H. Baeck et al. [5] for SDS templated tungsten oxide films, 1 g of PSS-Na was dissolved in 17.6 ml of mQ water. Then 4.8 mL of APTA were added and the final solution was magnetically stirred at room temperature for 1h before use. The electrodeposition proceeded as described in the previous paragraph for Brij-56. The applied potential was varied between -0.4 V and -0.6 V. It appeared that PSS-Na had a high affinity for the glass/FTO electrode which obstructed the deposition of tungsten oxide species. Therefore the films were only partially covered. Lower amounts of PSS-Na (0,33 g) have been tested as well but no changes have been observed.

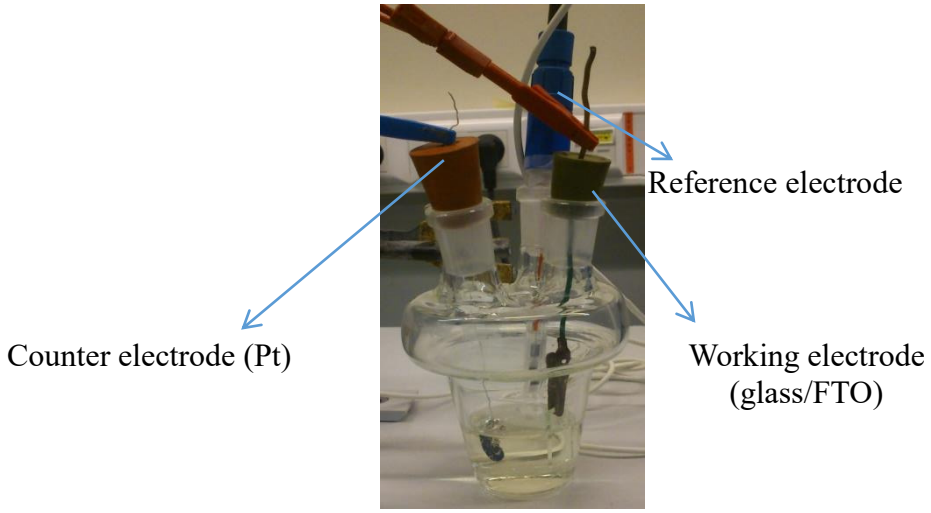

Figure 4.3: The three electrode configuration set-up for electrodeposition

None of the films were uniform and transparent. Significant border effect and incomplete coverage were the main characteristics of these films along with inconsistency in the experimental process.

The films were characterized by XRD (X-Ray Diffraction), TEM (Transmission Electron Microscopy) and SEM (Scanning Electron Microscopy). These techniques are described in Chapter 3. Additionally, ATR-FTIR (Attenuated Total Reflectance-Fourier Transformation Infrared Spectroscopy) was acquired for the PSS-Na containing films on a Bruker Equinox 55 FTIR instrument and a germanium crystal.

4.3 Results and discussion

4.3.1 Films deposited with Brij-56 surfactant

Different EO/W ratios (0, 2 and 5) have been tested in order to obtain porous electrodeposited films. First of all, the films were amorphous in the selected aforementioned thermal treatment (data not shown).

Figure 4.4 presents the electrodeposition curves for the three different solutions. The presence of Brij-56 in the plating solutions influences somewhat the rate of deposition. While 5 mins are needed to deposit ~300 mC.cm^{-2} in the surfactant-free solution in the Brij-56 containing solutions ~ 7 mins are required to reach the same charge density.

The SEM micrographs in Figure 4.5 reveal that the presence of the surfactant in the plating solution does not significantly affect the microstructure of the films. A rough surface with spherical particles is present in every case.

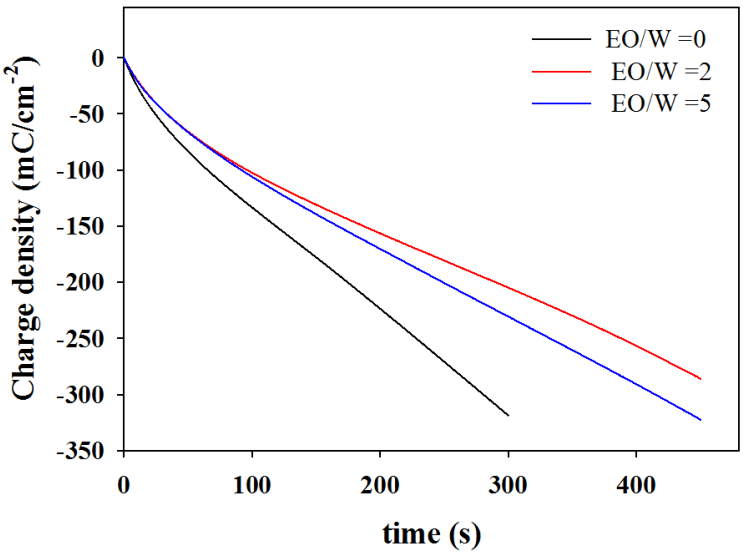

Figure 4.4: Electrodeposition curves for three Brij-56 containing solutions, EO/W=0 (black curve), EO/W=2 (red curve), EO/W=5 (blue curve)

Figure 4.6 b/c presents the TEM micrographs of the films electrodeposited at different EO/W ratios. From the images it is suggested that the films electrodeposited with Brij-56 contain very small worm-like pores. However, since the film with no Brij-56 (Figure 4.6 a) exhibits similar pore–like features we cannot confirm the presence of porosity induced by the templating mechanism in the Brij-56 containing films. In any case, the presence of ‘’porosity’’ in these films did not lead to any improvement in their electrochemical properties.

It should also be mentioned that some porosity is observed when the electrodeposition potential is increased at -0.65 V as well (Figure 4.7). However further investigations should be carried out in order to further confirm the existence of porosity through templating and the reproducibility of the electrodeposition process. The application of lower potentials (e.g. -0.1 V) were too time-consuming (more than one hour to obtain a charge density of about 300 mC.cm^{-2}) and therefore they were not studied any further.

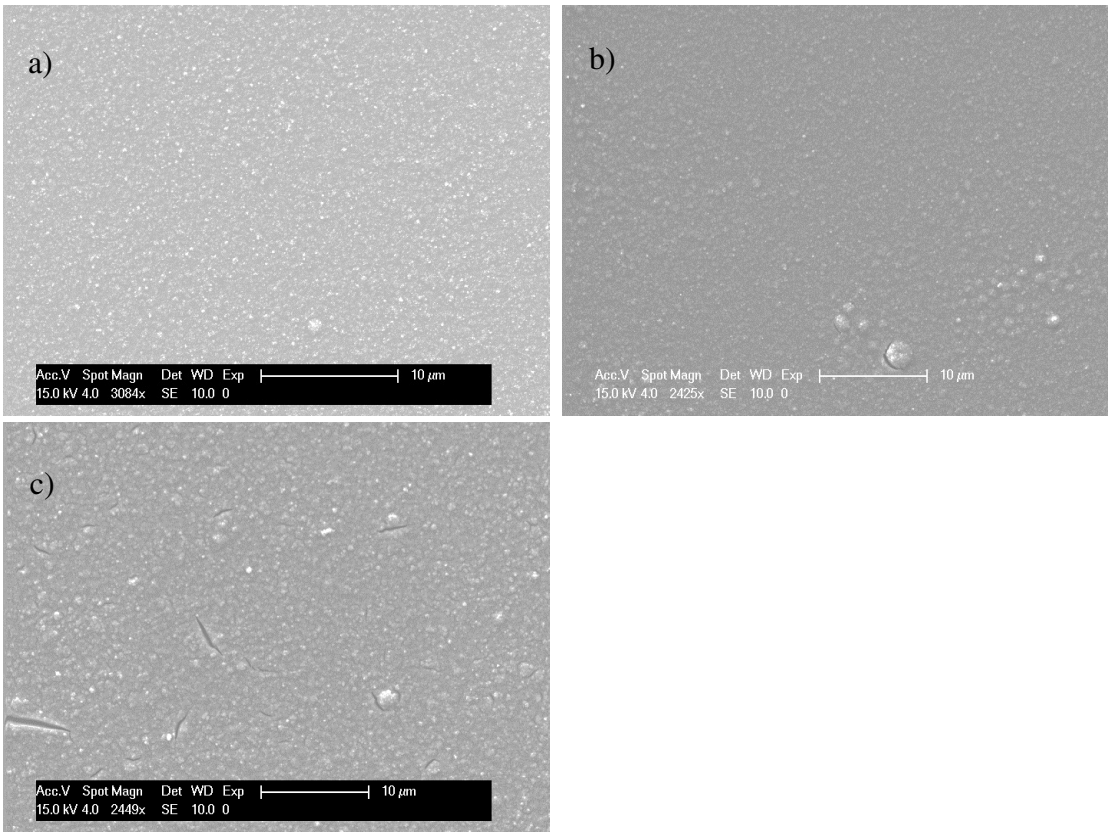

Figure 4.5: SEM micrographs of films with different EO (from PEO)/W ratio of: a) 0, b) 2, c) 5

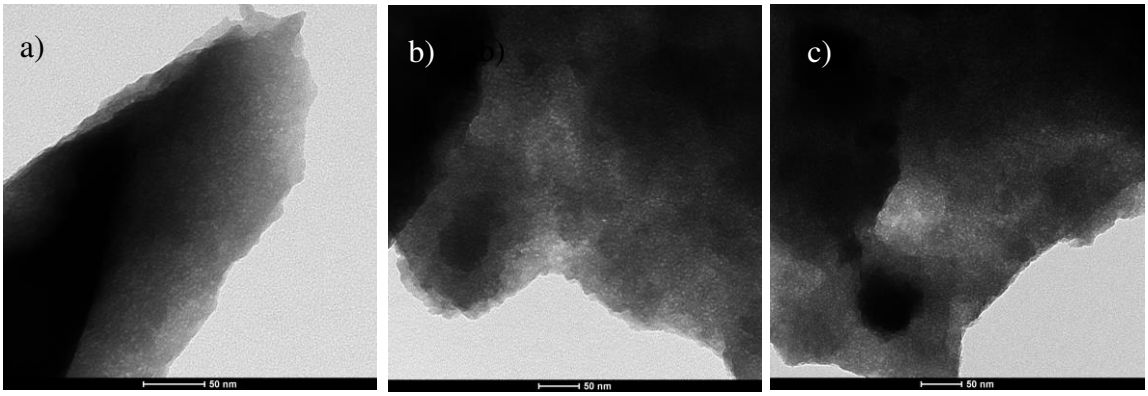

Figure 4.6: TEM micrographs of films with different EO (from PEO)/W ratio of: a) 0, b) 2, c) 5

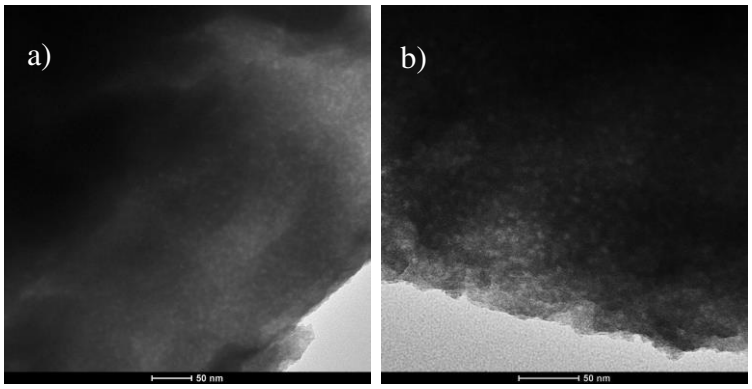

Figure 4.7: TEM micrographs from different regions of an as-deposited film electrodeposited at -0.65V

4.3.2 Films deposited with PSS-Na surfactant

Owning to their non-uniform deposition and the polyanionic nature of PSS-Na the study of PSS-Na-containing films was rendered very difficult under the microscope. Figure 4.8 presents two TEM micrographs acquired from different regions of the same as-prepared film electrodeposited at -0.4 V (Figure 4.8 a and b) and another micrograph from a film electrodeposited at -0.5 V (Figure 4.8 c). As it is depicted in the micrographs a and b, two different regions co-exist in the same film, one polymer-rich region (Figure a) and another one with dense inorganic matter (Figure b). Likewise, no porosity was observed in the film electrodeposited at -0.5 V (Figure c).

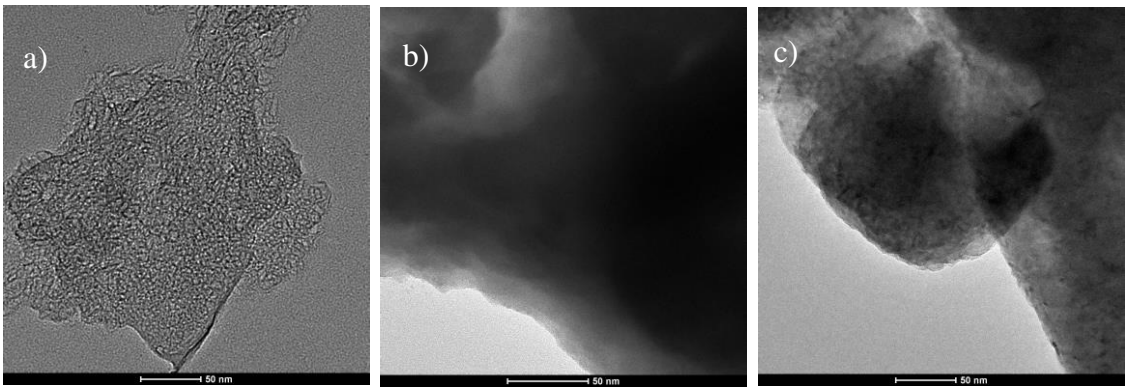

Figure 4.8: TEM micrographs of as-deposited PSS-Na-containing films. Micrographs a) and b) were acquired from different regions from a film electrodeposited at -0.4 V and at c) -0.5 V

The films electrodeposited at -0.4, -0.5 and at -0.6 V were thermally treated at 350ºC/2h and the micrographs are presented in Figure 4.9. Figure a illustrates a porous particle from a film deposited at -0.4 V where presumably PSS-Na efficiently templated tungsten oxide. However, this result cannot be generalized for the whole film since most matter in the same sample displayed more compact and dense entities. The films which were deposited at -0.5 V (Figure b) and -0.6 V (Figure c) did not display any porous structure.

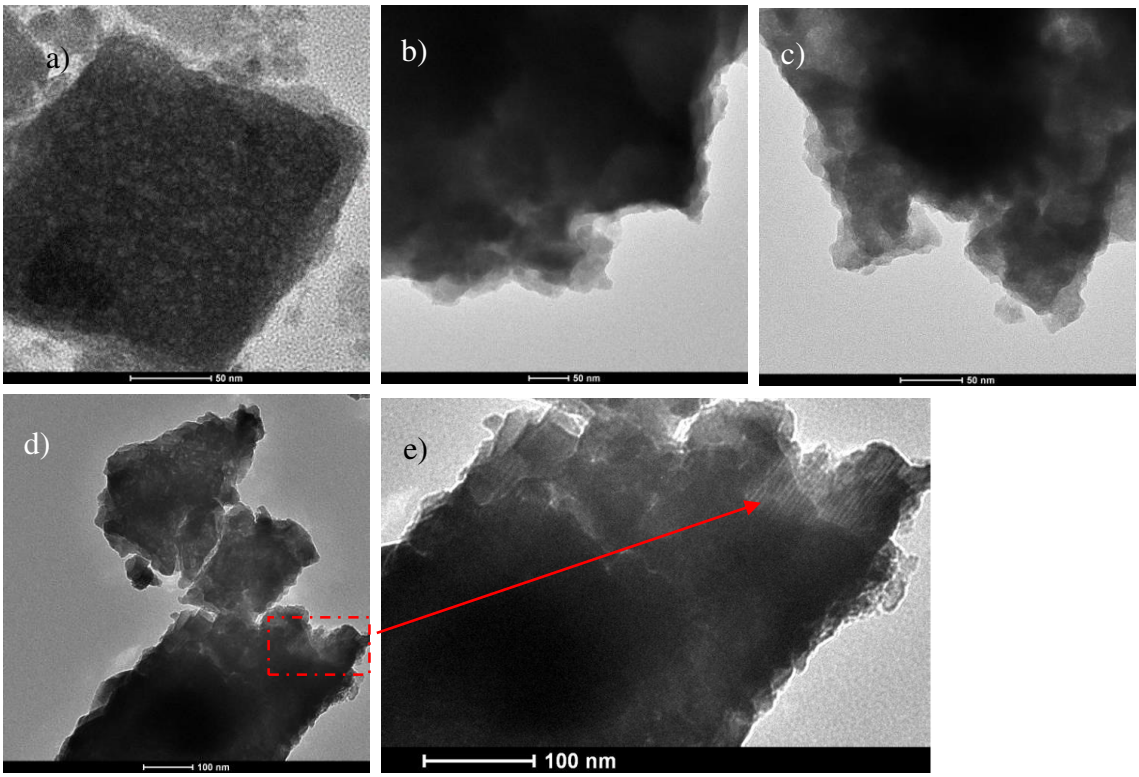

Figure 4.9: TEM micrographs of films deposited at a) -0.4 V and calcined at 350°C/2h b) -0.5 V and calcined at 350°C/2h c)-0.6 V and calcined at 350°C/2h, d) -0.4 V and calcined at 400°C/1h and e) magnification of micrograph d)

The film that was deposited at -0.4 V was also calcined at 400°C/1h (Figure 4.9 d and e). Even though this film was partially crystalline (data not shown) it randomly displayed some organized mesostructure (see Figure 4.9 d and e). Once more, the templating phenomenon only occurred at a low yield according to TEM micrographs (not shown) and most particles under the microscope appeared to be dense.

ATR/FTIR spectra of as-deposited films electrodeposited at -0.4 V and at -0.5 V were also acquired (Figure 4.10). In both cases, the peaks attributed to PSS-Na are discernible and annotated in the spectrums. In the film that was deposited at -0.5 V (black spectrum in Figure 4.10) a wide peak attributed to the stretching vibration of O-W-O is also detected. This signifies that the as-deposited film already consists of a tungsten oxide network. On the other hand, the film that was deposited at -0.4 V (red spectrum in Figure 4.10) is mostly comprised by the peaks of PSS-Na. No characteristic peaks of the APTA precursor or of the inorganic network are observed in this film. However, the small peaks at around 1000 cm^{-1}, 960 cm^{-1}, 890 cm^{-1}, 580 cm^{-1} might be possibly attributed to different types of W-O bonds (e.g. W=O, O-W-O) stemming from different clusters in the film. It should be mentioned that a second spectrum of this film was acquired while the beam was focused on another region in the film and the result was again the same (spectrum not shown). Nevertheless, after calcination the ATR-FTIR spectra of both films are characterized by a distinct O-W-O peak of the inorganic network (data not shown). Therefore, we believe that

the templating mechanism in the films that were deposited at -0.4 V might be possibly favored by the deceleration of the inorganic network formation.

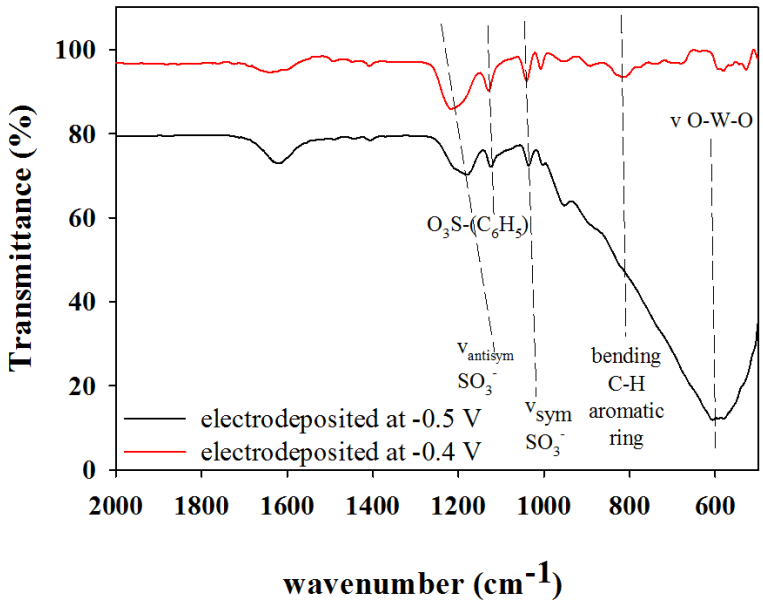

Figure 4.10: ATR-FTIR spectra of as-deposited films electrodeposited at -0.4 V (red spectrum) and -0.5 V (black spectrum). The annotations for PSS-Na were based in the analysis of [24]

4.4 Conclusions

In this chapter, we studied the possibility of producing mesoporous tungsten oxide films through electrodeposition. Two different surfactants have been tested for this purpose one non-ionic (Brij-56) and one anionic (PSS-Na). However, mesoporous films via this method appeared to be a challenging task and further investigations should be carried out in order to optimize all the experimental parameters. Low coverage, no strong evidences of porosity, lack of reproducibility and low electrochemical properties are some of the problems encountered in this chapter.

In the Brij-56 systems, the films exhibit a granular morphology despite of the content of the surfactant in the plating solution. There is some evidence of porosity based on TEM micrographs but no direct proof that templating is indeed taking place.

In PSS-Na systems, some random evidences of templating have been found in films that were deposited at -0.4 V. The porosity occurs in a very low degree in the films and most part appears to be dense and compact. No porosity has been detected in films that have been deposited at higher potentials (-0.5 V and -0.6 V). ATR-FTIR spectra showed that very fast network condensation occurs at -0.5 V (a wide peak assigned to O-W-O bond appears in the ATR spectrum) unlike the films deposited at -0.4 V where small peaks of W-O bonds are detected probably attributed to different W-O clusters.

4.5 References for Chapter 4

[1] C. Sanchez, C. Boissière, D. Grosso, C. Laberty, L. Nicole, Design, Synthesis, and Properties of Inorganic and Hybrid Thin Films Having Periodically Organized Nanoporosity†, Chemistry of Materials, 20 (2008) 682-737.

[2] Y. Tan, E.M.P. Steinmiller, K.-S. Choi, Electrochemical Tailoring of Lamellar-Structured ZnO Films by Interfacial Surfactant Templating, Langmuir, 21 (2005) 9618-9624.

[3] R.L. Spray, K.-S. Choi, Electrochemical synthesis of SnO_2 films containing three-dimensionally organized uniform mesopores via interfacial surfactant templating, Chemical Communications, (2007) 3655-3657.

[4] H. Luo, J. Zhang, Y. Yan, Electrochemical Deposition of Mesoporous Crystalline Oxide Semiconductor Films from Lyotropic Liquid Crystalline Phases, Chemistry of Materials, 15 (2003) 3769-3773.

[5] S.H. Baeck, K.S. Choi, T.F. Jaramillo, G.D. Stucky, E.W. McFarland, Enhancement of Photocatalytic and Electrochromic Properties of Electrochemically Fabricated Mesoporous WO3 Thin Films, Advanced Materials, 15 (2003) 1269-1273.

[6] T. Xue, C.-L. Xu, D.-D. Zhao, X.-H. Li, H.-L. Li, Electrodeposition of mesoporous manganese dioxide supercapacitor electrodes through self-assembled triblock copolymer templates, Journal of Power Sources, 164 (2007) 953-958.

[7] B. Dong, T. Xue, C.-L. Xu, H.-L. Li, Electrodeposition of mesoporous manganese dioxide films from lyotropic liquid crystalline phases, Microporous and Mesoporous Materials, 112 (2008) 627-631.

[8] W.-j. Zhou, J. Zhang, T. Xue, D.-d. Zhao, H.-l. Li, Electrodeposition of ordered mesoporous cobalt hydroxide film from lyotropic liquid crystal media for electrochemical capacitors, Journal of Materials Chemistry, 18 (2008) 905-910.

[9] P.A. Nelson, J.M. Elliott, G.S. Attard, J.R. Owen, Mesoporous Nickel/Nickel Oxidea Nanoarchitectured Electrode, Chemistry of Materials, 14 (2002) 524-529.

[10] Y. Tan, S. Srinivasan, K.-S. Choi, Electrochemical Deposition of Mesoporous Nickel Hydroxide Films from Dilute Surfactant Solutions, Journal of the American Chemical Society, 127 (2005) 3596-3604.

[11] K.-H. Kim, K.S. Kim, G.-P. Kim, S.-H. Baeck, Electrodeposition of mesoporous ruthenium oxide using an aqueous mixture of CTAB and SDS as a templating agent, Current Applied Physics, 12 (2012) 36-39.

[12] A. H. Whitehead, J. M. Elliott, J. R. Owen, G. S. Attard, Electrodeposition of mesoporous tin films, Chemical Communications, (1999) 331-332.

[13] K.S. Choi, E.W. McFarland, G.D. Stucky, Electrocatalytic Properties of Thin Mesoporous Platinum Films Synthesized Utilizing Potential-Controlled Surfactant Assembly, Advanced Materials, 15 (2003) 2018-2021.

[14] Ö. Dag, S. Alayoğlu, C. Tura, Ö. Çelik, Lyotropic Liquid-Crystalline Phase of Oligo(ethylene oxide) Surfactant/Transition Metal Salt and the Synthesis of Mesostructured Cadmium Sulfide, Chemistry of Materials, 15 (2003) 2711-2717.

[15] A. Gomes, M.I. da Silva Pereira, Pulsed electrodeposition of Zn in the presence of surfactants, Electrochimica Acta, 51 (2006) 1342-1350.

[16] M. Deepa, A.K. Srivastava, S. Lauterbach, Govind, S.M. Shivaprasad, K.N. Sood, Electro-optical response of tungsten oxide thin film nanostructures processed by a template-assisted electrodeposition route, Acta Mater., 55 (2007) 6095-6107.

[17] M. Deepa, A.K. Srivastava, S.A. Agnihotry, Influence of annealing on electrochromic performance of template assisted, electrochemically grown, nanostructured assembly of tungsten oxide, Acta Materialia, 54 (2006) 4583-4595.

[18] M. Deepa, A.K. Srivastava, K.N. Sood, S.A. Agnihotry, Nanostructured mesoporous tungsten oxide films with fast kinetics for electrochromic smart windows, Nanotechnology, 17 (2006) 2625-2630.

[19] M. Deepa, M. Kar, D.P. Singh, A.K. Srivastava, S. Ahmad, Influence of polyethylene glycol template on microstructure and electrochromic properties of tungsten oxide, Solar Energy Materials and Solar Cells, 92 (2008) 170-178.

[20] A.K. Srivastava, M. Deepa, S. Singh, R. Kishore, S.A. Agnihotry, Microstructural and electrochromic characteristics of electrodeposited and annealed WO_3 films, Solid State Ionics, 176 (2005) 1161-1168.

[21] M. Giannouli, G. Leftheriotis, The effect of precursor aging on the morphology and electrochromic performance of electrodeposited tungsten oxide films, Solar Energy Materials and Solar Cells, 95 (2011) 1932-1939.

[22] B. Yang, H. Li, M. Blackford, V. Luca, Novel low density mesoporous WO_3 films prepared by electrodeposition, Current Applied Physics, 6 (2006) 436-439.

[23] H. Zheng, J.Z. Ou, M.S. Strano, R.B. Kaner, A. Mitchell, K. Kalantar-zadeh, Nanostructured Tungsten Oxide – Properties, Synthesis, and Applications, Advanced Functional Materials, 21 (2011) 2175-2196.

[24] K.-H. Ko, H.R. Park, J.-S. Kim, Y.-W. Kim, Tangible plasticization/filler effects of sodium salts of dimer acids on the mechanical properties of styrene ionomers, Journal of Applied Polymer Science, 129 (2013) 2443-2450.

Chapter 5
Ultrasonic Spray Pyrolysis Technique (USP)

5.1 Generally about spraying methods

In spray pyrolysis methods, a film is deposited by spraying a solution on a heated substrate [1] (Figure 5.1). These methods were first introduced in 1966 by Chamberlin and Skarman [2] who produced among others (mostly sulfides, cadmium and selenide compounds) CdS films for applications in solar cells. They can be found in the literature with different names such as ‘’solution aerosol thermolysis’’, ‘’mist decomposition’’, ‘’aerosol decomposition’’ etc. according to the working temperature range, but ‘’spray pyrolysis’’ has predominated over the last years [3]. The interest in the spraying methods has progressively expanded in an industrial level over the years, due to their cost-effectiveness [4-6], their fast and continuous production rates [6-8], without requiring vacuum conditions [6, 9]. Besides sulfides [2, 10] much work has also been accomplished on semiconductive oxide films including WO_3, some of them being listed in Table 5.1. These materials act as transparent conductive electrodes in different applications such as in solar cells, antireflection coatings, gas sensors, electrochromics, electronics, battery electrodes, fuel cells, biomedical materials, etc. [9, 11-13]. It is worthy to note that the idea of combining the spraying methods for the application of conductive coatings on float glass was suggested as early as in 1975 [4].

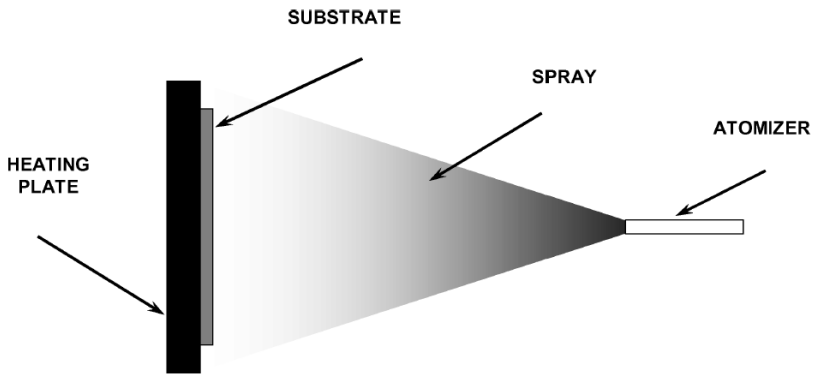

Figure 5.1 [1]: A simplified spraying set-up

Table 5.1: Inorganic oxides that have been prepared with different spraying methods

Metal oxide	Spraying technique	Reference
SnO_2/In_2O_3:Sn	Air-pressurized spray pyrolysis	[14, 15]
CeO_2	two fluid nozzle, airblast spray pyrolysis	[13, 16]
Mixed oxides (e.g. $La_{0.8}Sr_{0.4}Co_{0.2}Fe0.8O_{3-\delta}$, $Ce_{0.8}Gd_{0.2}O_{1.9-x}$, NiO-$Ce_{0.8}Gd_{0.2}O_{1.9-x}$ $LaCrO_3$ $(La_{0.8}Ca_{0.2})CrO_3$ $La(Cr_{0.5}Mn_{0.5})O_3$)	Air-pressurized spray pyrolysis, ultrasonic spray pyrolysis, two-fluid nozzle	[12, 13, 17, 18]
ZnO	Air-pressurized spray pyrolysis	[19]
NiO_x	Air-pressurized spray pyrolysis, ultrasonic spray pyrolysis	[20, 21]
WO_3	Ultrasonic Spray Pyrolysis, Air-pressurized spray pyrolysis	[22-32]
TiO_2	Ultrasonic spray pyrolysis	[6]
Co_xO_y	Glass nozzle (method not specified)	[33]
Fe_xO_y	Pressurized spray pyrolysis	[34]
CuO	Air-pressurized spray pyrolysis	[14]
MgO	Ultrasonic Spray Pyrolysis	[35]
Ytria stabilized zirconia (YSZ)	Electrostatic and Pressurized spray deposition	[5, 11]
ZrO_2	Electrostatic Spray Pyrolysis	[36]

The spraying methods are categorized as electrostatic [3, 9, 11, 12, 37], pressured [3, 9, 11, 12, 17], or ultrasonic [3, 9, 12, 18, 26], according to the applied spraying mechanism. In this PhD, an ultrasonic nozzle AccuMist (Sono-Tek), presenting an apical spraying geometry, has been used for the production of porous and non-porous WO_3 films (Figure 5.2).The ultrasonic atomization exhibits different advantages compared to other types of atomization, such as smaller droplet size (1-100 vs. 10-100 μm for pressure nozzles), smaller size distribution with a lower power supply, droplets with finer sphericity and lower momentum [3, 38, 39]. These advantages enable a better control over the film growth and hence more homogeneous, more continuous and more transparent films are yielded [10, 30].

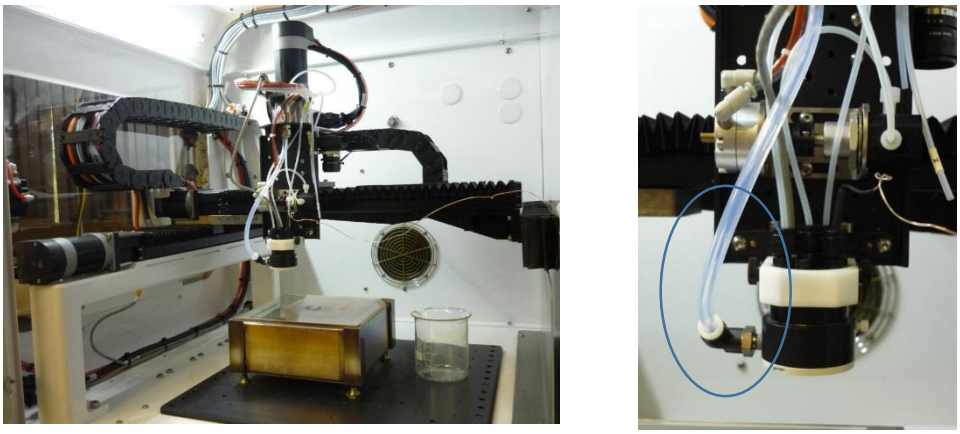

Figure 5.2: The USP device (Exactacoat, Sono-Tek) which is available in the lab a) Nozzle system and the hot plate are displayed b) The AccuMist nozzle from a closer view. From aside (circled area) compressed air stream is supplied and is mixed with the droplets

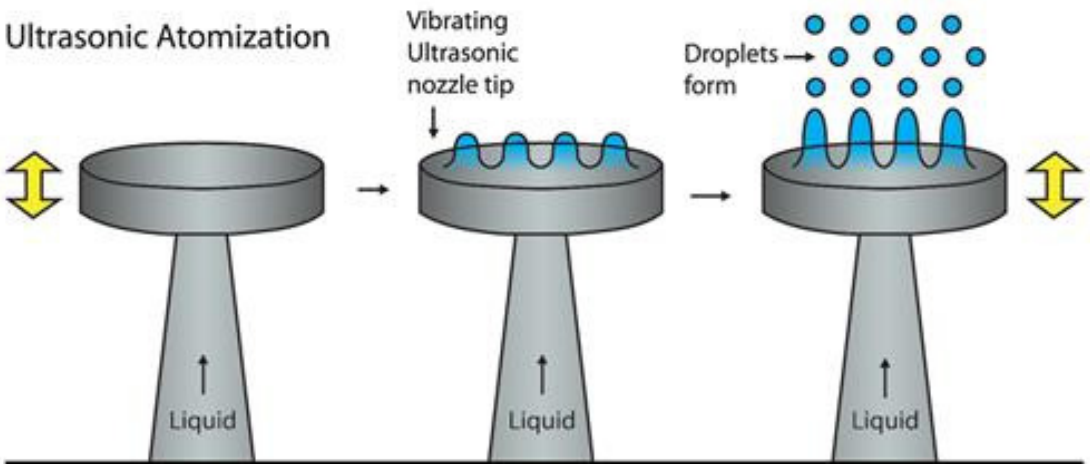

Figure 5.3[40]: The principle of droplets' formation by an ultrasonic nozzle

The ultrasonic atomization process is based on the formation of ultrasonic waves (capillary waves) in the spraying solution on an ultrasonic excited metal surface. At some point, the tips of these waves become unstable and release small droplets, as depicted in the scheme in Figure 5.3 [7, 38, 39].

In our case, compressed air was used in order to conduct the mist of the droplets towards the substrate. For a more uniform deposition and thickness, the nozzle was moving during spraying with a certain type of motion and specific speed over the substrate. For the same reasons, other mobile systems have been reported [4, 10] such as substrate's motion or a combined movement of the substrate and the nozzle.

5.2 Spraying stages and spraying conditions

There are many different processes occurring simultaneously or sequentially during spraying and subsequently different varying parameters could influence the film growth. Generally, the spraying process consists of four major stages: 1) Dissolution or dispersion of the inorganic precursor (or other components if they exist) into the solvent 2) Solution

atomization 3) droplets transport under the influence of gravitational and drag forces, evaporation of the solvent and diffusion of its vapors from the surface of the droplet to the carrier gas, shrinkage of the droplet, diffusion of the solutes towards the center of the droplet due to a concentration gradient and 4) drying and decomposition of the inorganic precursor [1, 36]. Simultaneously other phenomena could take place during drying such as nucleation, crystal growth, different chemical reactions and sintering [8]. Solution conditions, solution flow rate, nozzle-to-substrate distance, droplets size, nozzle or substrate motion, substrate temperature etc. are some of the parameters which could affect droplets evaporation rate, precursor decomposition (or other reactions) and eventually the film growth [1, 3, 4, 12, 41]. Some of these parameters will be further discussed in the following paragraphs. It is noteworthy to mention that for the successful formation of a continuous film it is desired that most of the droplets strike the substrate and spread in the maximum possible extent [1].

5.2.1 Influence of the substrate's temperature on the atomization process

According to the literature, substrate temperature is one of the most (if not the most) important varying parameter in the spraying process [5, 12, 13, 17]. The heat (convective and radiant) [36] nearby the substrate influences the trajectory of the droplets, their evaporation rate, the rate and the nature of the reactions and eventually the films growth [13]. Moreover, the temperature selection should be made according to the nature of the deposition solution (precursor, additives and their concentrations) in order to obtain a uniform and a continuous film [12].

Depending on the temperature, four spraying steps were identified (initially proposed by J.C. Viguie and J. Spitz [41]) (Figure 5.4) [1, 9, 41]: **a)** in the lowest temperature range the wet droplets reach the substrate, they spread and wet the surface. At the same time, solvent is evaporating, solid is precipitating and precursor is decomposing. In this case, due to the presence of the solvent, the temperature of the substrate is significantly reduced [36] **b)** at higher temperatures the droplets evaporate completely during the flight and decomposition is completed on the substrate **c)** at even higher temperatures the solvent evaporates before the droplet reaches the substrate, the precipitate melts and vaporizes and the vapors diffuse to the substrate where the precursor is decomposed and precipitates. **d)** At the highest temperatures the same process as in c) occurs but the precursor solidifies before it reaches the substrate. Case d is preferably avoided (and also sometimes case a when the amount of solvent is too high) as it produces rough, non-adherent [1, 6] or powdery [5, 6] films.

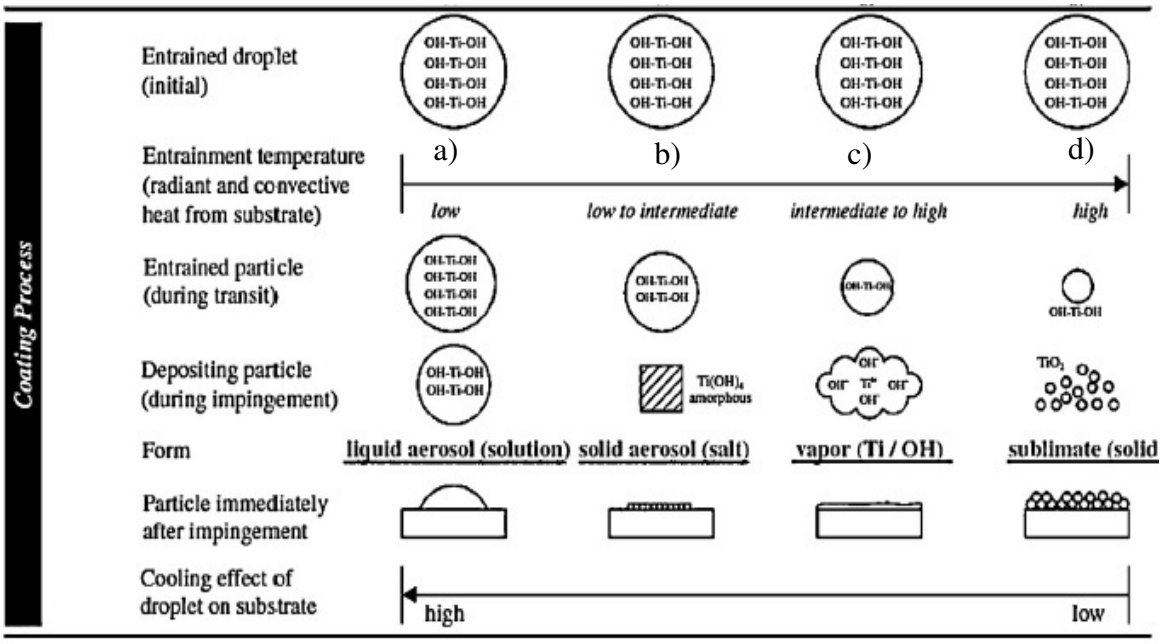

Figure 5.4 [9]: Illustration of TiO_2 film formation under different temperature ranges

The efficient temperature range for uniform films varies from system to system and it depends on many factors [5, 12, 13] such as the nature of the material that is deposited, the solvent, the gas and the liquid flow rate, the set-up geometry, the drying and the decomposition kinetics, the type of the substrate [17] etc.

Muecke et al. [17] for instance, found that the maximum temperature to obtain continuous and uniform films for their system under study ($Ni/Ce_{0.8}Gd_{0.2}O_{1.9-x}$) was linearly proportional to the solvent boiling point and it was always higher by approximately 100ºC. Above the maximum temperature no film was formed and below this range the films were non-continuous. They attributed this relation to the thermophoretic forces where the smaller droplets dry out and blow away from the substrate, and to the Leidenfrost effect where the droplets are dragged away by the air stream while they are levitating above a vapor layer which covers the substrate [13, 17]. Moreover, above a certain temperature, the droplets dry out before reaching the substrate and subsequently due to limited spreading, discrete particles are formed rather than a continuous film layer [5]. All these phenomena lead to the decrease of the deposition rate with the increase of the temperature.

Similarly, D. Beckel et al. [12] studied the optimal deposition temperature for their system ($La_{0.6}Sr_{0.4}Co_{0.2}Fe_{0.8}O_{3-\delta}$ in a mixture of ethanol and diethylene glycol monobutyl ether). They investigated the morphology of their films according to the $T_{depositon}/T_{solvent\ boliling\ point}$ ratio. They observed that regardless the composition of their solvent mixture, there was one optimum ratio for their system (1.16) where the films were homogeneous and uniform. Above this value the films were non-continuous and below this value (very close to the solvent's boiling point) the films contained cracks (Figure 5.5) [12, 17]. The cracks probably resulted from the higher thickness and the higher amount of material that is deposited at lower temperatures. At higher temperatures, due to thermophoretic forces, the amount of droplets (and subsequently the amount of material) that is deposited is lower [1,

12, 17]. Another explanation for the origin of cracks at lower temperatures is the excess of solvent in the residing droplets (wet droplets) and its fast evaporation which leads to stresses inside the forming film [5, 12, 36]. Others [13, 14, 36], supported that the cracks stem from the precursor's decomposition when the solvent is completely evaporated. Therefore it is suggested [12, 13] that the deposition temperature should be such in order to permit the presence of some solvent inside the film during decomposition, to alleviate the different stresses that can be developed during precursor's decomposition and to wet the surface.

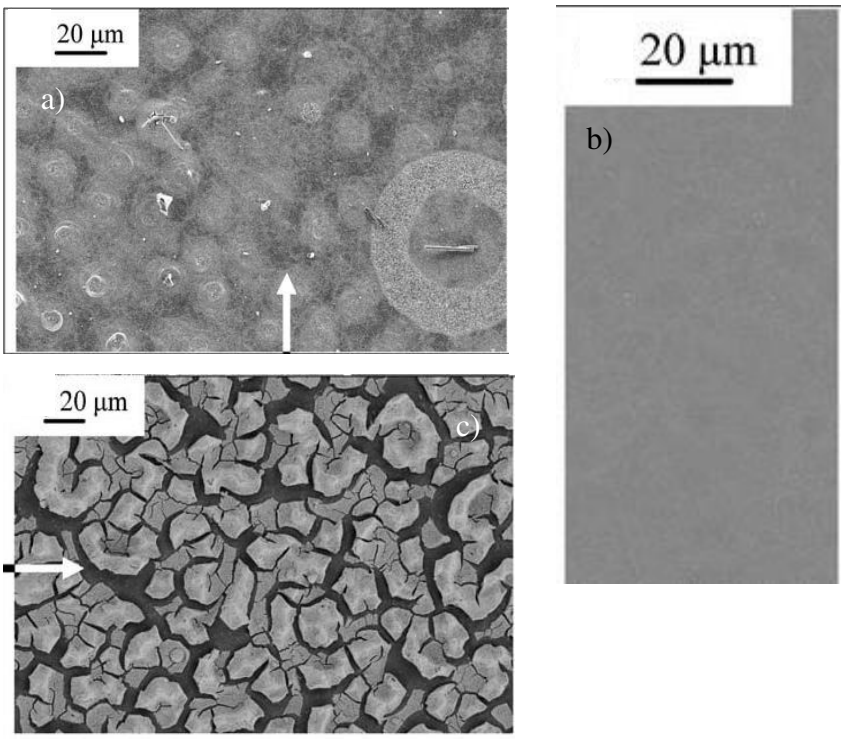

Figure 5.5 [12]: SEM images from films prepared with $T_{depositon}/T_{solvent}$ boiling point ratio of a) 1.31 and $T_{depositon}$: 320°C b) 1.16 and $T_{depositon}$: 195°C and c) 1.02 and $T_{depositon}$: 195°C (The ethanol's portion was varied in order to adjust the boiling point)

Wang et al. [8] studied the influence of the temperature on the droplets size and on the droplets concentration with the use of a laser diffraction technique. They found that as the temperature increased, the droplets size decreased and the droplets concentration increased. The latter increases the solvent vapor concentration during droplets transportation and subsequently it decreases the solvent evaporation rate [1, 24]. This phenomenon leads to a slower precipitation and potentially to films with better quality [24]. Moreover, due to the high number of droplets, coagulation was also observed at high temperatures [8].

5.2.2 Effect of surface tension

The surface tension affects the droplets size which defines the particles size in powdery products [3, 8] and the spreading process of the droplets on the substrate [36]. Moreover, it was reported that the initial droplets size influences the spraying advancement of the

droplets (first published by W. Siefert [42]) in a similar way as the substrate's temperature in Figure 5.4 (see also Figure 5.6).

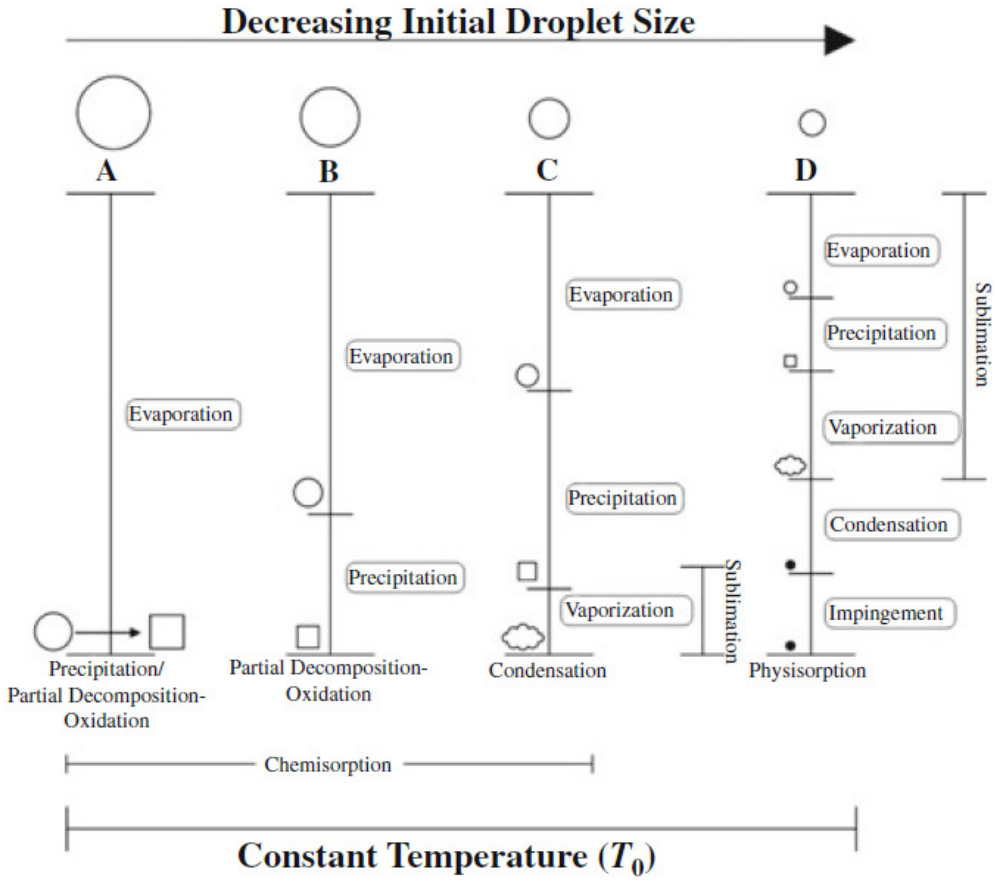

Figure 5.6: Spray pyrolysis mechanism as a function of initial droplets size and constant temperature

Generally, smaller droplets wet the surface and spread more efficiently rather than bigger ones, due to their lower surface tension [36]. Droplets size is associated with the surface tension according to the Lang's equation (*Equation 5-1*) and a more empirical one (*Equation 5-2*):

$$d_d = 0.34\,(\frac{8\pi\gamma}{\rho f^2})^{1/3} \qquad \textit{Equation 5-1}$$

$$d_d = constant\; f^{-0.66} Q^{0.207} \gamma^{0.11} \rho^{-0.274} \eta^{0.166} (\frac{power}{area})^{-0.4} \qquad \textit{Equation 5-2}$$

where γ is the surface tension, ρ the density of the liquid, f the frequency of the ultrasonic transducer, Q the liquid flow rate and η the viscosity of the liquid. However, these equations are very rough approximations and they fail to estimate the real droplets size [39]. The surface tension can be tuned by modifying the composition of the solvent [8], the concentration of the precursor [8], or by adding additives such as surfactants [36]. These parameters will be discussed more deeply in the following paragraphs.

5.2.3 Effect of additives

Additives are frequently used in the coating techniques such as in dip-coating [43], in electrodeposition [44], but also in different spraying methods [5, 21, 24, 36]. They function as wetting agents, agglomeration inhibitors [25] and they improve the spreading behavior of the solution by reducing its surface tension [5, 21, 24, 26, 36, 44]. This results in the production of uniform and crack-free films with lower roughness compared to the films without any additives [5, 21]. In spray pyrolysis methods, the presence of the polymers reduces droplets size [21, 26], increases the solvent boiling point which delays the spreading process [36] and it enables a higher maximum permitted temperature for the occurrence of a continuous film (see paragraph 5.2.1). PEG is one of the most common wetting agents that have been thoroughly used in the literature [21, 24, 26, 44], but others have been studied as well, such as more non-ionic surfactants (PVA (poly-(vinyl alcohol) [36], P123 (poly(ethylene oxide)$_{20}$-poly(propylene oxide)$_{70}$-poly(ethylene oxide)$_{20}$) [29, 30]), cationic (HTAB (Hexadecyl-trimethylammonium bromide) [24, 25], and DTAB dodecyltrimethylammonium bromide [19, 29] and anionic surfactants (SDS (sodium dodecyl sulfate) [29]. As it was discussed in the previous chapters, throughout this phD, Brij-56 has been used as a porogen and as a wetting agent.

5.2.4 Effect of the solvent

Apart from the different additives, **solvent** composition can determine the surface tension as well. It was found for instance, that by adding ethanol to an aqueous solution, droplets with smaller droplet's size are obtained, due to the decrease of the solution's surface tension (Figure 5.7) [8, 17]. Furthermore, the solvent's boiling point determines the maximum permitted temperature for the formation of a continuous film as it was discussed in the previous paragraph. Different solvents have been studied in the spraying processes including water [21, 26], ethanol [17], diethylene glycol monobutyl ether [5, 12, 36], 1-methoxy-2-propanol [5] etc.

5.2.5 Effect of the precursor

Precursor nature and **concentration** are two more parameters that should be considered. Chlorides [5, 13], nitrates [5, 13], perchlorates [13], ammonium [31] or metal-organic salts (acetylacetone, acetates etc.) [5, 13, 41] are some of the salts that have been tested in the spraying solutions. In some cases, stabilizing agents (such as acetic acid and acetyl acetone) are added in order to prevent the metal precursor's precipitation [15, 22, 24, 25]. For example, wet films have been obtained with nickel bromide and nickel chloride precursors, due to the stable hygroscopic intermediates that are formed upon thermal decomposition [13]. Muecke et al. [13] have pointed out that some precursors (such as acetates and nitrates), during their decomposition are producing gaseous products which lead into different deposit morphologies from irregularly shaped residues to voids that occur from trapped bubbles.

Importantly, the precursors should be highly soluble in the chosen solvent and the concentration should be high enough (and subsequently the deposition rate) in order to

produce continuous and smooth films and to create possibly smaller droplet (surface tension decrease with the increase of the concentration) [5, 8, 12]. However, too high precursor concentrations lead to large mechanical stresses due to the precursor decomposition and subsequently to an increased number of defects and cracks [36]. Muecke et al. [13] observed that as the concentration of the their nickel based precursor approached its saturation concentration, ring-like features were transformed into disc-like features (Figure 5.9). The ring (disk)-like structures are commonly observed in spray pyrolysis methods [13, 36]. Generally, as the droplet strikes the substrate, it spreads and the spreading extent is determined by the size of the droplet, the surface tension and the viscosity of the solution. When the substrate is heated, the solute inside the droplets migrates towards the boarders of the droplet where the evaporation rate is higher and it starts to precipitate (ring-like structures). As the evaporation of the solvent is progressing, more and more material is migrating towards the surface and the thickness of the ring is increasing. Close to the saturation concentration (or at high temperatures) precipitation occurs throughout the droplet and not just on its surface and therefore the ring-like structures are transformed into disc-like features (Figure 5.7) [13, 36].

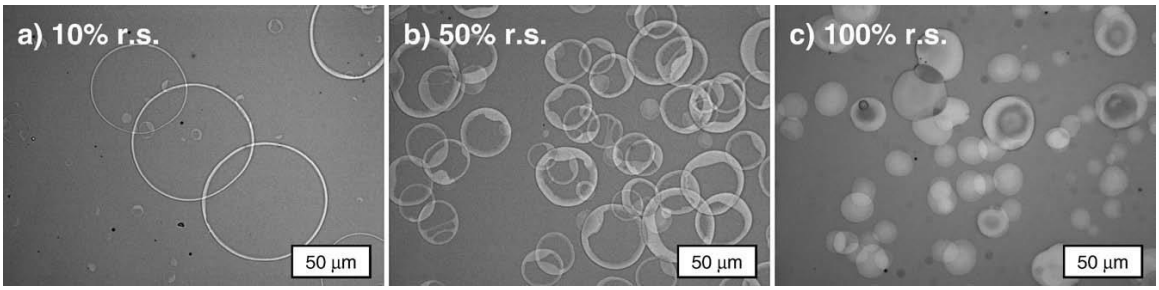

Figure 5.7 [13]: Light microscope images of a nickel acetate precursor with different relative saturations (r.s)

In order to obtain smooth and continuous films rather than randomly distributed splats, Beckel et al. [12] proposed a model which was emphasizing on the packing of precipitated particles (Figure 5.8). More specifically, they suggested that as the solid is formed or deposited on the substrate, it is dragged to the edges of the droplets or it is moved on the surface either because of capillary forces or because of the impact of new deposited droplets. This movement is occurring until the particles collide with each other. Therefore when the concentration of the precursor is low (or when the precursor is highly soluble in the solvent), the newly formed precipitates will travel un-obstructed and accumulate in one place. On the other hand, when many precipitating centers exist on the surface at the same time, the solid particles are locked in their places and the emerging film is smoother.

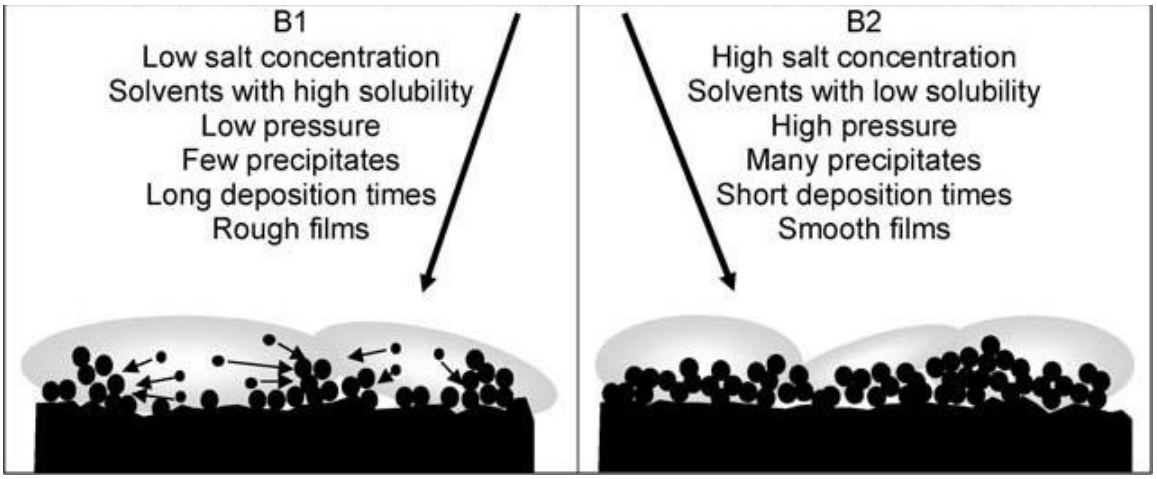

Figure 5.8 [12]: Proposed model for the precipitation of a film at different experimental conditions

5.2.6 Nozzle-to-substrate distance

By altering the nozzle-to-substrate distance it is possible to modify the evaporation rate and the film's growth process in the same trend as the substrate's temperature in Figure 5.4 and in Figure 5.9 [1, 41].

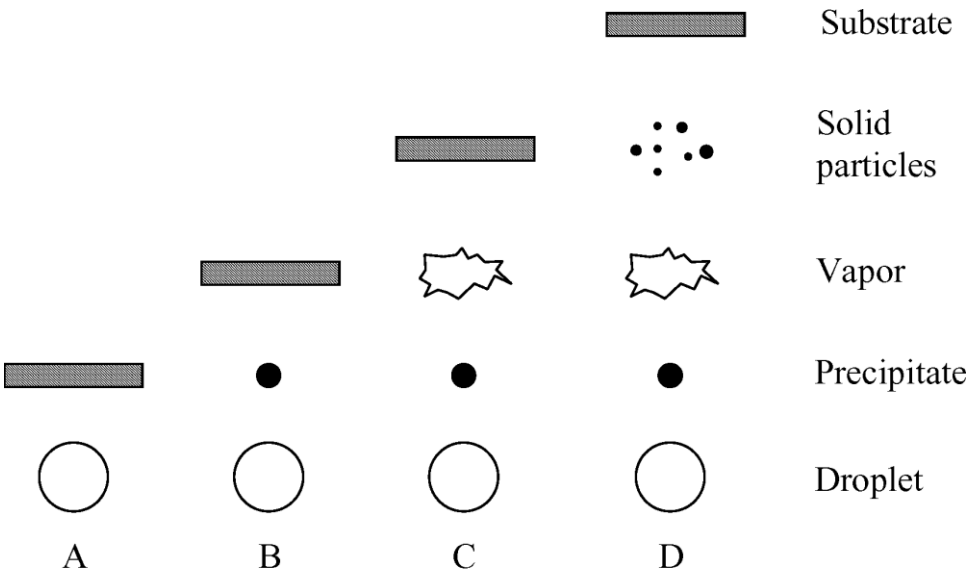

Figure 5.9 [1]: Deposition process by varying nozzle-to-substrate distance

According to U.P. Muecke et al. [17], by decreasing the working distance the deposition rate is increased along with the deposition of smaller droplets due to their increased droplet velocity.

5.3 Porous films prepared with spraying deposition methods

Porous films have been attempted and prepared with a great number of techniques as it was discussed in the introduction, including spraying pyrolysis.

In spraying methods, porosity has been obtained either intentionally (by using additives as templates [24, 25, 29, 30]) or randomly, for example during the evaporation of gaseous products from the metal precursor (e.g ammonium) [22].
L.M Bertus et al. [24] prepared homogeneous porous films with a combination of two polymers (HTAB and PEG). According to their model, PEG was located around the HTAB-inorganic assemblies rendering them more stable during annealing.

Porous films have also been obtained in the work of Li et al. [29, 30] using P123 as a templating agent in WO_3 films. Pore's size was estimated between 8-20 nm and the increased surface area significantly improved the electrochromic efficiency of the films (~50 cm^2/C for films with BET area of 18 m^2/g, compared to 28 cm^2/C for films with BET area of 8 m^2/g). The TEM micrographs in Figure 5.10 depict a porous (image a), crystalline (image b) film, however the images are not illustrative of porosity obtained through templating but rather from the random distances of the different crystallites.

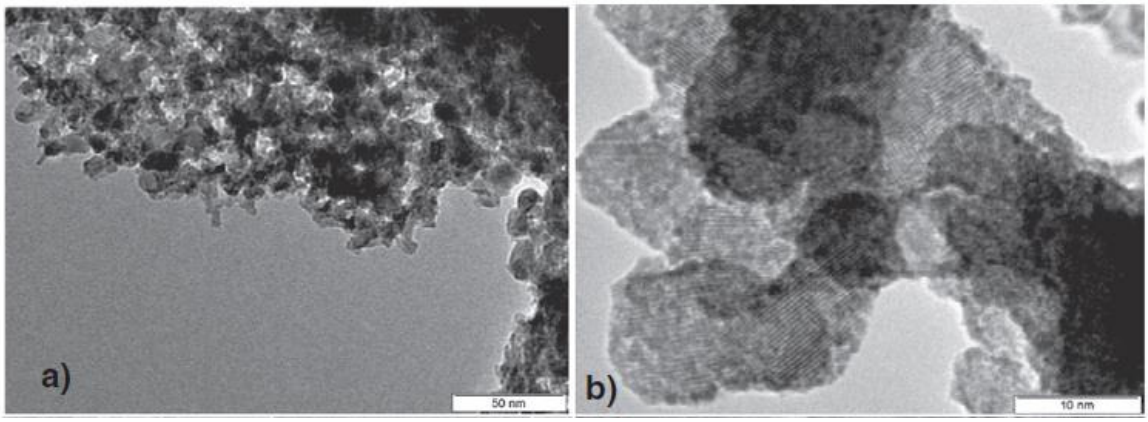

Figure 5.10 [29]: Low and high magnification TEM micrographs of a WO_3 film deposited at ambient conditions and calcined at 350°C

5.4 Experimental part

Brij-56 (Brij-C10, average Mn: 683, Sigma Aldrich) and APTA (W-H_2O_2-acetic acid) were used as a templating agent and tungsten precursor, respectively. The synthesis of APTA has been described in Chapter 2 and it was based on the work of Sharma et al. [45]. The only difference in this experiment was that after the removal of the excessive H_2O_2 by reflux, the precursor remained stabilized in its aqueous solvent rather than precipitating as a solid by rotary evaporator. In that way, the need of ethanol as a re-dispersing agent was avoided and the spraying process was conducted under aqueous conditions.

For the spraying solution, 0.6g Brij-56 (0.02M) were dissolved in 10mL of milliQ H_2O at 70°C for 10 minutes. After cooling down to RT, 10mL of APTA were added (W/EO molar ratio = ~0.5) and the final solution was stirred at RT for 1h before spraying. This solution was stable for many weeks. As a reference, a solution without template was also prepared. In the absence of the surfactant the precursor precipitated within a few days (see Table 5.2).

It should be noted, that even though the aforementioned templating solution was stable for several weeks, it was becoming unstable as soon as the concentration of APTA was *decreased* to its half. This phenomenon can be attributed to different factors such as a) the pH change which can lead to the isoelectric point or to a pH where insoluble tungsten species are predominant and b) the inevitable increase of H_2O/W ratio which might shift the equilibrium towards the insoluble tungstic acid's ($WO_3.xH_2O$) formation. According to Table 5.2 the first assumption is ruled out because pH doesn't considerably change by diluting the solution. The second case appears to be the most likely and this is further verified by the formation of a *stable* solution 1.5 times more diluted, with a moderate H_2O/W value (see Table 5.2).

Table 5.2: Stability of different APTA solutions

Solution	pH	H_2O/W molar ratio	W/EO	Stability	Viscosity (cp)*
Liquid Precursor (no dilution)	0.5	----	----	Stable for months if stored in the fridge	----
Precursor solution diluted by a factor of 2 (reference solution)	1.0	200	----	Stable for some days	1.4
Standard solution (described in the text)	1.1	200	0.5	Stable for some weeks	1.8
Standard solution diluted by a factor of 2	1.5	400	0.5	Unstable (precipitates within 30 min)	----
Standard solution with half amount of precursor	1.5	400	0.2	Unstable (precipitates within 30 min)	----
Standard solution diluted by factor of 1.5	1.3	264	0.5	Stable	----

* Viscosity values were measured with a falling sphere viscometer and they were calculated according to the equation: $\mu = K(p_f - p).t$ where μ is viscosity in cp, K is viscometer's constant equal to 3.3, p_f is the density of the ball equal to 2.53 g/mL, p the density of the liquid measured in the lab and t the time (min) for the ball to travel inside the tube. The values presented in the table are the mean values of three different measurements.

5.4.1 Spraying parameters

The ultrasonic spraying device from Sono-Tek which has been used in this PhD is shown in Figure 5.2. The AccuMist nozzle connected to this device is depicted in Figure 5.11 and it produces a highly focused fine mist of small droplets driven apically onto the surface with the assistance of a low pressured air. During spraying, the nozzle was moving in the XY plane (the nozzle-to-substrate distance was constant) with a specific geometry (S-type arc in our case) and a specific speed. In order to have a full coverage, the second layer was always beginning from a shifted Y position in order to cover all the empty spaces of the S shaped movement.

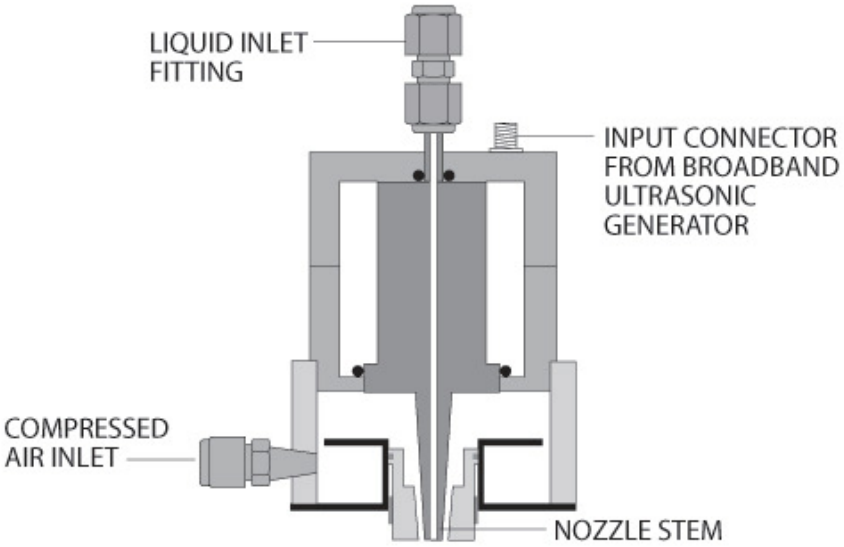

Figure 5.11: The geometry of an AccuMist nozzle

The standard spraying conditions which were used in this PhD are presented in Table 5.3. Before spraying, the substrates were placed in the center of the hotplate for 5 min in order to reach the working temperature. All the temperature values that are mentioned in this chapter are displayed as indicated on the heat monitor of the USP device and they correspond to the hotplate temperature (and not to the substrate surface). However, a deeper study with the use of a thermographic camera revealed that there was a spatial temperature variation (around 50% of deviation between the edges and the center) along the hotplate and a discrepancy between the intended and the maximum obtained temperature (Figure 5.12). This effect resulted in slightly lower actual temperatures than the indicated values.

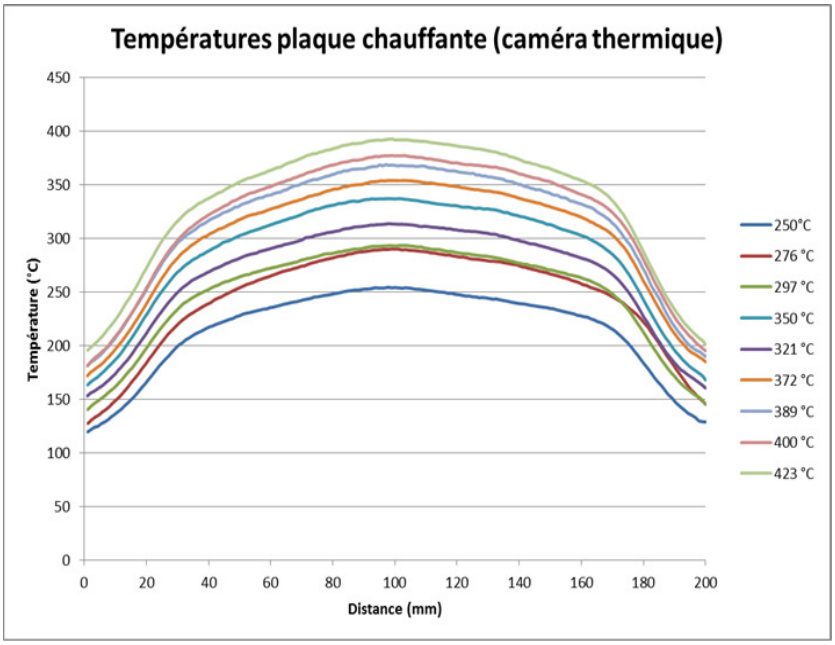

Figure 5.12: Plots of the actual temperature in function of the position on the hotplate. In the legend, the intended value is depicted

Table 5.3: Standard spraying conditions

Power (W)	f (kHz)	Flow rate (mL/min)	Working distance (cm)	Pattern/Spacing (mm)	Spraying speed (mm/s)	No. layers	Stabilization time (min) after spraying
3	120	0.25	5.8	S type/4	40	2	5

The spraying solution was deposited onto SnO_2:F coated glass (glass/FTO) substrates (Dyesol, 15Ω/sq, 2 cm x 2 cm x 2,2 mm). In some cases (e.g. for infrared spectroscopy purpose) the films were deposited on silicon wafers. Before use, all the substrates were cleaned by consecutive immersion in milliQ water (5 min), acetone (15 min) and ethanol (15 min) under sonication. It should be mentioned that due to the different temperature profile close to the silicon surface, the deposition behavior was different compared to the glass/FTO. For example, due to the higher thermal conductivity and the lower thickness of the silicon wafers, more layers were needed in order to cover adequately the substrates. This was more noticeable as the temperature increased.

In order to find the optimum number of layers for this system, films with 2, 4 and 6 layers were prepared. The films with two layers were the most suitable, since the films with 4 and 6 layers were too thick, hazy and peeling off during the electrochemical measurements.

Different parameters were studied in order to determine the role of each on films porosity, homogeneity, morphology and eventually on their electrochromic properties. These parameters will be discussed in the following paragraphs.

The films were characterized by XRD (X-Ray Diffraction), TEM (Transmission Electron microscopy), SEM (Scanning Electron Microscop), FT-IR (Fourier Transformation Infrared Spectroscopy) and profilometry.

X-ray diffraction was performed on a Bruker D8 diffractometer (CuKalpha radiation) in grazing incidence configuration with an incident angle of 0.5°, a 2-theta range from 10° to 70°, a step size of 0.02° and a scan speed of 1 s/step. All the films that have been studied are amorphous (data not shown).

TEM micrographs were acquired at an acceleration voltage of 200kV in bright field (BF) and dark field (DF) modes (Tecnai, G2, Twin, FEI). Films were scratched from the substrates, sonicated in ethanol and then deposited on a carbon-coated grid.

The morphology and the relative amount of W in the films was studied by SEM microscope (FEG- ESEM XL30, 15kV, FEI and EDS spectrometer, Bruker). The relative amount of W in the films was extracted from their X-ray emission spectrum. More specifically, the intensity of W Lα peak was recorded and compared to a pure W standard to calculate the so-called “k-ratio” of tungsten atom in the films. We used this k-ratio value to normalize the quantitative data in electrochemical experiments and to designate with relative values in which way the amount of tungsten was varied with the different spraying conditions.

IR spectra were recorded in transmission mode from films deposited on silicon wafers using a Bruker Equinox 55 FTIR instrument. The reference was a bare silicon wafer.

The thicknesses were determined by mechanical profilometry (Dektak 150, VEECO) on the FTO/glass substrates.

Similarly with the dip-coated films (chapter 3), we attempted to study the films via ellipsometry. However, due to the more pronounced haze factor of these films the analysis was rendered incoherent and therefore no ellipsometric results will be discussed in this chapter.

The electrochemical measurements were conducted in the glovebox as described in Chapter 3.

The UV spectra were acquired ex-situ on a Perkin Elmer lambda 14P (300-1000nm). A constant voltage (2.225 V or 4.255 V vs. Li/Li^+ for the coloration and bleaching process) was applied for 4 min each and the UV spectrum was acquired (glovebox).

Some films were also subjected to in-situ chronoamperometric UV-Vis measurements. For this purpose the aforementioned UV-Vis device was connected to a PAR EG&G potensiostat (model 273 A). The three-electrode configuration cell was comprised by an $Ag/AgNO_3$ (0.01 M) as a reference microelectrode, a platinum wire as the counter electrode and the WO_3 deposited on a glass/FTO as the working electrode. For the chronoamperometric measurements -1.54 V was applied for 4 min during the coloration process while 0.7 V were applied for 4 min during the bleaching process. The transmittance was measured at a wavelength of 550 nm where the sensitivity of human eye during the photopic state is maximized [46].

5.5 Results and discussion

5.5.1 Effect of substrate's temperature on templated films

In order to study the influence of the substrate's temperature, the working temperature was varied between 100 and 390°C and the films were stabilized for 5 min after deposition to decompose the precursor and eliminate the surfactant. The films that were deposited at 100°C were further post-treated in a separate oven (with a ramp of 1°C/min) at 350°C for 2h under air in order to permit the full thermal conversion of the W precursor into WO_3.

Appearance, amount of deposited material and thickness of the films

Generally, all the films exhibit a hazy appearance (Figure 5.13) which becomes more noticeable as the temperature increases. This phenomenon is attributed either to the non-uniform packing of the droplets, to the presence of cracks and/or to the formation of gaseous products imprints on the surface of the films. The opaque appearance of the as-deposited films is a restraining factor for their good quality and their potential industrial application. One of the most challenging prerequisites for a successful electrochromic study is to obtain flawless electrochromic layers which would color and bleach in a uniform way.

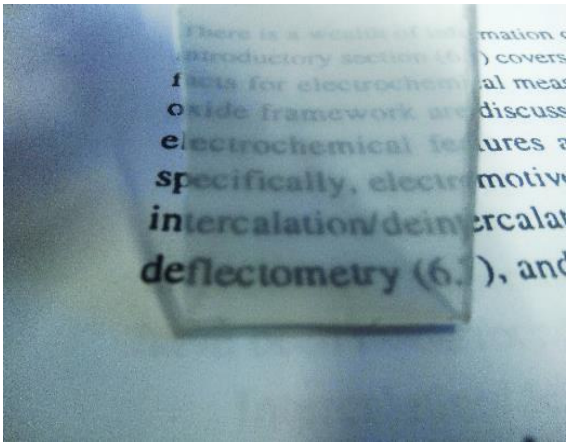

Figure 5.13: Image of a film deposited at 190°C

Furthermore, the deposition at 190ºC yielded somewhat brownish films, indicating the presence of combusted organic residues which led to an undesired absorption in the visible range. In order to remove the surfactant, the films underwent UV ozonolysis for 15 and 30 min without any noticeable changes in the coloration of the films.

On the other hand, the films that were deposited at 290ºC and 390ºC were highly transparent as a result of their lower material content. For example, at 390ºC, six layers were needed (rather than two) in order to render the study of the films feasible. According to the literature and as it was discussed in paragraph 5.2.1, the decrease of W oxide deposition with temperature is an expected fact, due to the thermophoretic forces which drag the smaller droplets away and/or to the Leiderfrost effect (vapor cushions which inhibit the deposition of the droplets). The calculation of the k-ratio from the EDX measurements at each deposition temperature, corroborate with this statement (Figure 5.14)

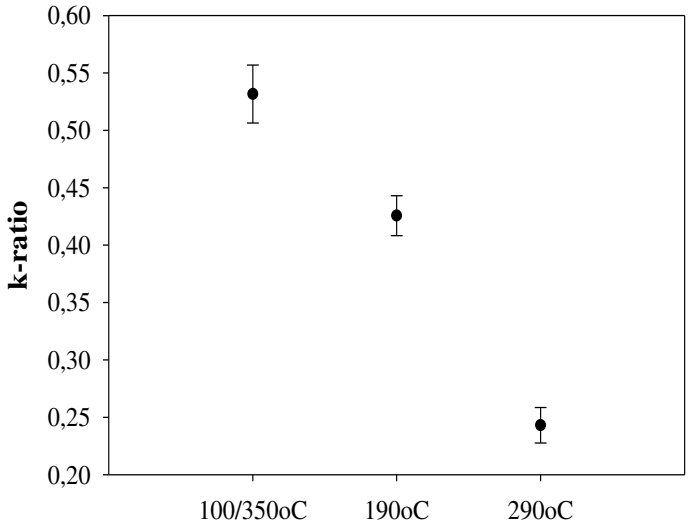

Figure 5.14: Mean values of the k-ratio (with their standard deviations) calculated from EDX measurements. The values are relative to a W reference

Microstructure and thickness of the films

From the SEM micrographs in Figure 5.15, it is straightforward that the deposition temperature largely impacts the morphology or the coating development of the films.

Figure 5.15 a and b show that the 100ºC (post-treated) films were smooth, continuous and they were composed of well superimposed droplets. The deposit adequately covered the substrate, however, these films presented several cracks. As it was reported in paragraph 5.2.1, there are many factors which might lead to a substantial cracking, such as the evaporation of a considerable amount of water which remains inside the films at this deposition temperature (see also the discussion on the infrared spectra in the next paragraphs), the extensive post-treatment at a relatively high temperature (350ºC), the fast annealing ramp, or the massive decomposition of the precursor during the annealing step. In order to prevent the formation of cracks, a more progressive stabilization treatment was attempted before calcining at 350ºC (deposition at 100ºC and then stabilization at 150ºC for 15 min on a separate hotplate) however the cracks emerged again (data not shown).

Similarly, a continuous layer with cracks was obtained when the deposition temperature increased to 190ºC (Figure 5.15 c, d). Additionaly, at this temperature, round prints are observed which probably stem from gaseous decomposition products.

The films' continuity was disrupted once the hotplate reached 290ºC and instead, the precursor was deposited as discrete droplets (Figure 5.18 e and f). In this case, the boiling of the solvent was predominant and therefore the top of the droplets was covered by bubble remainings.

On the other hand, no film was formed at higher temperatures (Figure 5.15 g and h) and the precursor solution was rather precipitating in a powdery form, sparsely distributed on the substrate.

Conclusively, in this work the maximum ***studied*** temperature which resulted in a continuous layer was 190ºC. In paragraph 5.2.3 it was stated that additives could increase the maximum deposited temperature for the occurrence of a continuous film either by improving solution wettability or by increasing solvent boiling point. In this work two trials have been attempted in order to increase the maximum possible temperature: a) by increasing the amount of the surfactant to double and b) by adding 2g of diethylene glycol with a boiling point of 245ºC in the standard solution while maintaining the concentration of the precursor and surfactant constant [17]. Unfortunately attempt a) not only did not increase the maximum temperature but a considerable amount of surfactant remained inside the films judging from their intense brown color. No improvement was observed in the attempt b) as well (data not shown).

Due to their rough and non-uniform surfaces, the study of the films via profilometry was rendered inconclusive (data not shown).The profilograms showed that, the thickness of the films that was deposited at 100ºC and then post-treated at 350ºC was roughly estimated at 200 nm. No information could be drawn from the profilogram of the films deposited at 190ºC (data not shown).

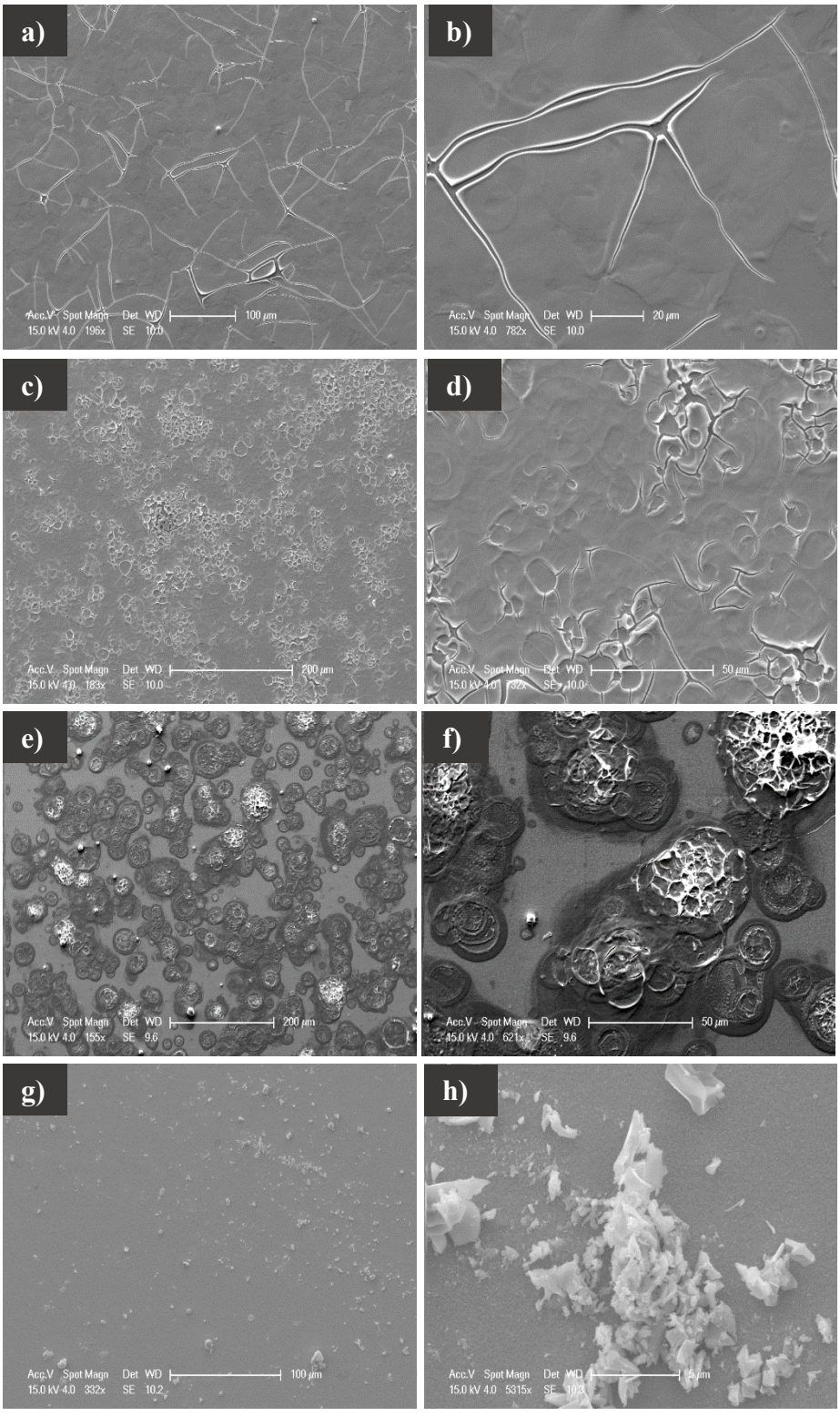

Figure 5.15: SEM micrographs of films deposited at different temperatures a), b) 100°C and post-treated at 350°C for 2h, c), d) 190°C, e), f) 290°C and g), h) 390°C. The temperature corresponds to the temperature of the hotplate and not to the substrate surface. The films were stabilized for 5 minutes after the deposition

Crystallinity of the films

All the films that were studied in this chapter were amorphous. The dark field micrographs for the films deposited at 100ºC (and then post-treated at 350ºC), 190ºC and 290ºC in Figure 5.16 corroborate with this result.

Some random nanocrystals appeared in the film that was post-treated at 350ºC (see red square in Figure 5.16) designating the onset of crystallization under these conditions. However, at this stage, the crystals were so few that their impact on the films' properties (structural and electrochemical) was negligible.

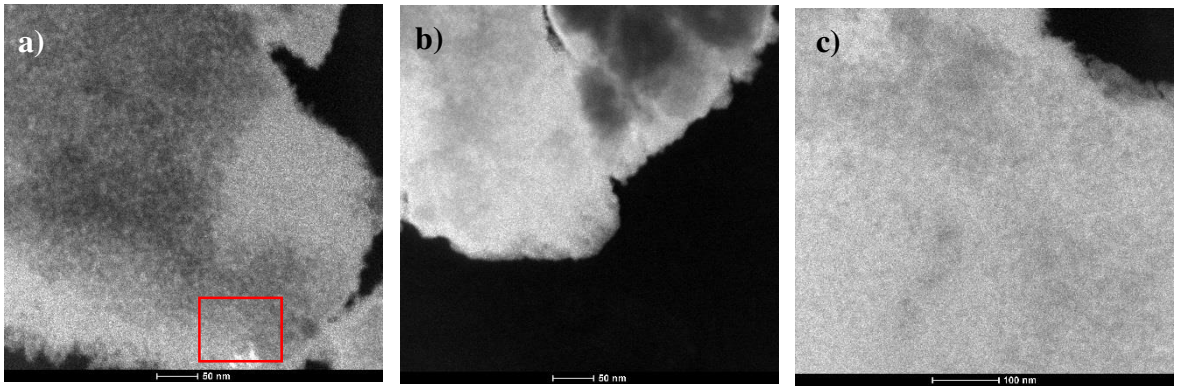

Figure 5.16: Dark field micrographs of films deposited at different temperatures: a) 100ºC then post-treated at 350ºC for 2h b) 190ºC c) 290ºC

Structural characterization by infrared spectroscopy

The films have also been studied by infrared spectroscopy. As shown in the infrared spectra in Figure 5.17 a and in Table 5.4, at 100ºC the precursor is not decomposed yet and the surfactant is still present inside the films. For this reason, all the films that were deposited at 100ºC were further treated at 350ºC for 2 hours. The post-annealing treatment led to the condensation and the formation of a slightly hydrated WO_3 network (the peak attributed to the stretching vibration of hydroxyls at 3124 cm^{-1} was considerably smaller compared to the as-deposited film) and to the elimination of the surfactant (Figure 5.17 b). It is noteworthy that the infrared spectrum of the calcined porous film obtained from the dip-coating technique (Figure 3.7) exhibited more distinct O-H and structural O-H bands and therefore it is considered to be more hydrated than the USP film. This effect infers that the dip-coated films presumably possess higher specific surface area.

At 190ºC (Figure 5.17 c), only some traces of the precursor remain inside the film (see Table 5.4) and the surfactant is completely eliminated. The latter contradicts the brownish color of the films, which manifests that they are not completely devoid of surfactant under these experimental conditions.

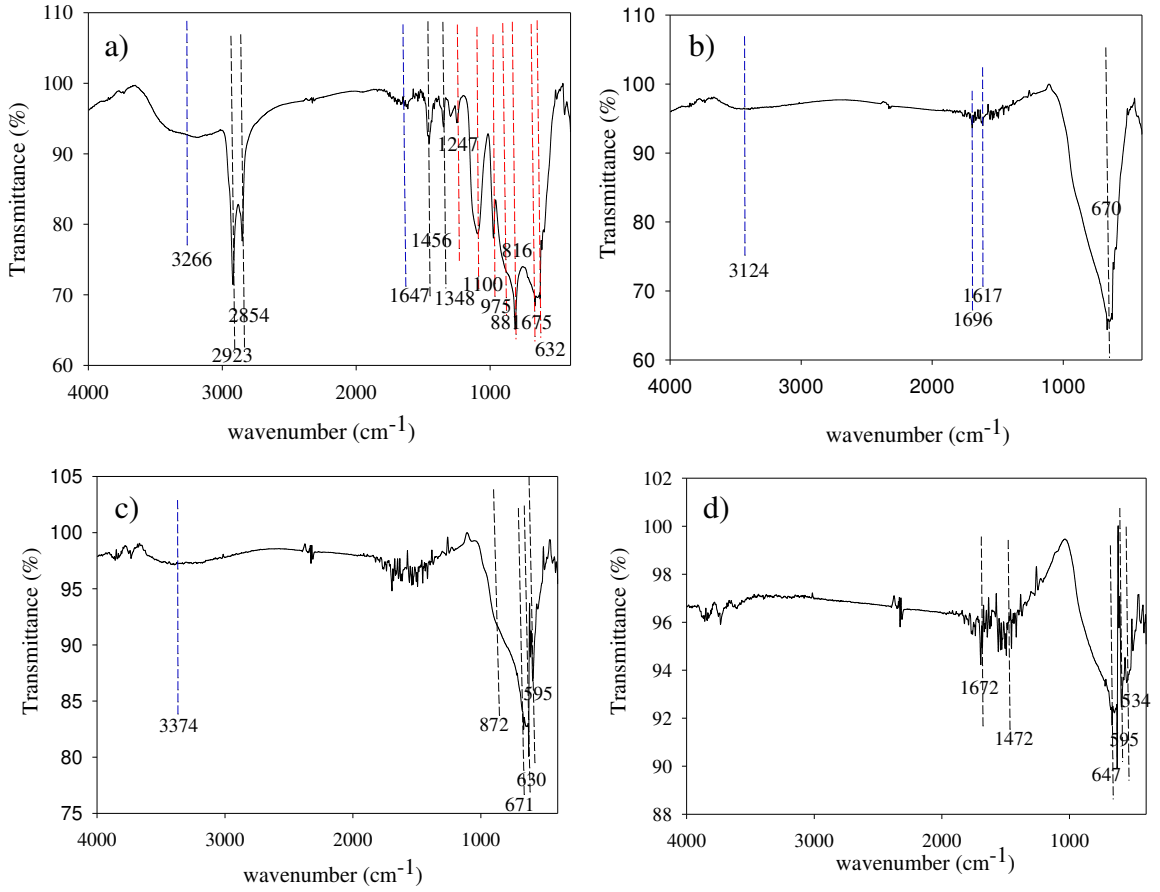

Figure 5.17: Infrared spectra of films deposited at different temperature: a) 100°C, the black lines designate peaks attributed to the surfactant, the red lines to the precursor and the blue lines to the presence of water b) 100°C and then post-treated at 350°C for 2h c) 190°C and d) 390°C

We attribute this discrepancy to the nature of the substrate (silicon wafers were used to perform the study on the infrared spectrometry instead of glass/FTO which were typically used for any other type of measurement) and their different thermal conductivity and thickness. Moreover, the presence of different –OH bonds (wide peak at 3374 cm^{-1}) and the splitting of the main W-O peak into smaller ones (671, 630 and 595 cm^{-1}) signified the incomplete condensation of the material (amorphous nature) under these experimental conditions and presumably the presence of porosity (hydrophilic surface and W-O clusters located on the surface).

Similar IR spectrum was acquired from the film that was deposited at 390°C (Figure 5.17 d). Even at this temperature, tungsten oxide appears to be hydrated (the peaks at 1672 and 1472 cm^{-1} attributed to structural water are still present) but with less surface –OH groups (lack of the peak at ~3000 cm^{-1}). Moreover, as in the case of the film that was deposited at 190°C, the W-O band is split into smaller ones (647, 595, 534 cm^{-1}) due to its hydrated nature.

Table 5.4: Infrared peaks and their assignments for the films deposited at different temperatures

	Film deposited at 100°C	Film deposited at 100°C and calcined at 350°C	Film deposited at 190°C	Film deposited at 390°C	Peak origin[1]	Ref.
ν (cm^{-1})	3266	3124	3374		ν(OH)	[47, 48]
	2923				C-H	[49]
	2854				C-H	[49]
	1647		1693,1620	1672	δ(HOH) (structural)	[47]
			1563, 1541		$\nu_{asym}(COO)_{bi}$ (free acetate) bidentate chelating	[45]
	1456		1499	1472	ν_{OH}, δ_{OH} (OH bonded with either water molecules or to surface oxygen atoms, W-O	[45, 48]
			1460 1417		$\nu_{sym}(COO)_{bi}$ (bidentate chelating) free acetate or $\delta(CH_3)$	[45]
	1348				$-CH_2-$	[49]
	1247				$\nu_{sym}(COO)_{mono}$	[45]
	1100				ν(W-O-C)	[45, 49]
	975				ν(W=O) (terminal modes of surface grains)	[48]
	881		872		ν(O-O) and $W-O-W_{intra}$	[45]
	816				$\nu(W-O-W)_{intra}$ of W_3O_{13} edge sharing units	[50]
	675	670	671		ν_{asym}(O-W-O), (C-H), (COO), δ(O-C=O)	[45]
	632		630	647	ν_{asym}(W-O-W)	[45, 50]
			595	595	Not found elsewhere, presumably some long W-O band	
				534	Coupling of the oxide lattice in $WO_3.n\ H_2O$	[48]

Porosity of the films

TEM micrographs in Figure 5.18 shows that all the aforementioned films (except the ones that were deposited at 390ºC which were not studied by TEM) contain pores. Unlike the porosity which was obtained by the dip-coating technique, in USP, the pores do not exhibit a grid-like architecture nor a long-range periodicity.

For example, in the films that were deposited at 100ºC (and then post-treated at 350ºC) the pores adopt a disordered worm-like structure. Even though a more quantitative discussion from the TEM micrographs was not possible, the pores size was somewhat stable as the temperature increased and the pores were not considerably shrank during dehydration and network's condensation.

It should be mentioned that the micrographs of the uncalcined films deposited at 100ºC give inconsistent observations, probably due to the incomplete polymerization of the precursor at this temperature (Figure 5.17 a). Typical compact particles (with even some porosity in some cases) were observed in Figure 5.19 a, however in most cases, the matter splattered the grid without possessing any coherence (Figure 5.19 b). This is probably occurring due to the dissolution of the precursor in ethanol which is the dispersing mean for the preparation of the grid. This hypothesis is further supported by the micrograph in Figure 5.19 c which was acquired from a film deposited at an even lower temperature. This film gave similar features, corroborating with the fact that at low temperatures where the precursor is still present, no coherent network is formed and therefore their study by TEM is not possible.

In order to investigate porosity at lower temperatures, some films were deposited at 100ºC and then stabilized at 150ºC for 15 min on a separate hotplate[1]. Under this thermal treatment, the extent of networking permitted the observation of some coherent surfactant-templated particles (Figure 5.20 a). However, due to the presence of surfactant and effectively the moderate contrast, porosity at this stage is not well distinct, in contrast to the calcined ones (Figure 5.20 b). After calcining the films at 350ºC for 2h well-apparent porous films were observed, similar with previously described post-treated films (see images a and b in Figure 5.18).

[1] 150ºC is the designated value from the hotplate. However, the actual temperature should be lower.

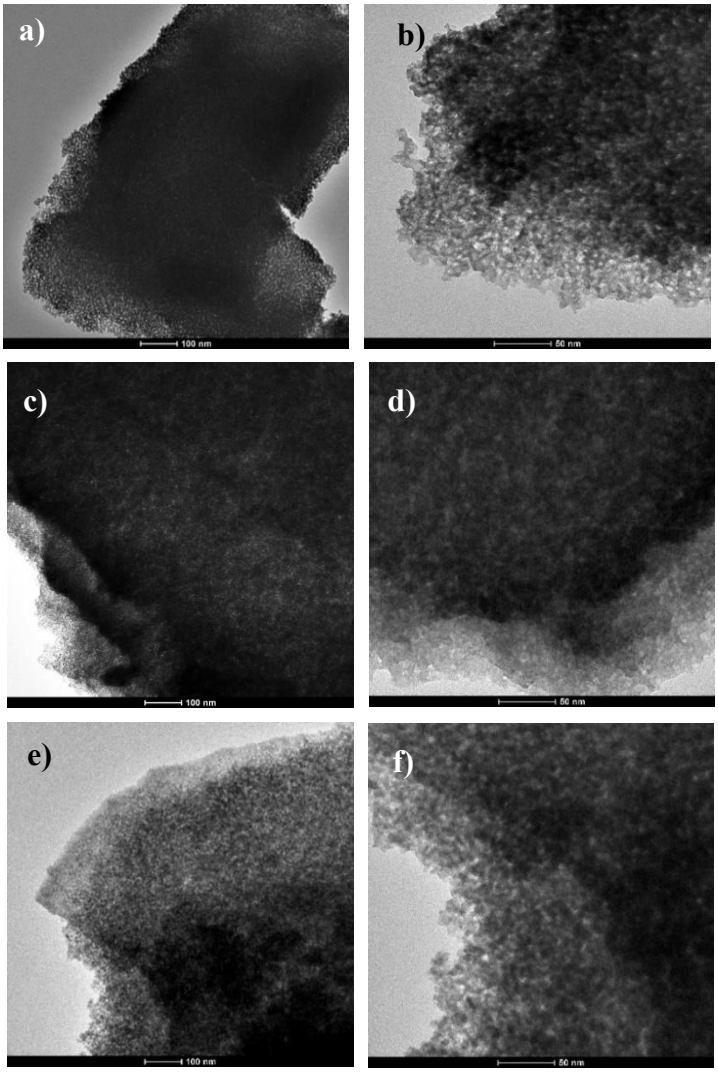

Figure 5.18: TEM micrographs of films deposited at different temperatures: a), b) 100°C and then post-treated at 350°C for 2h c), d) 190°C e), f) 290°C

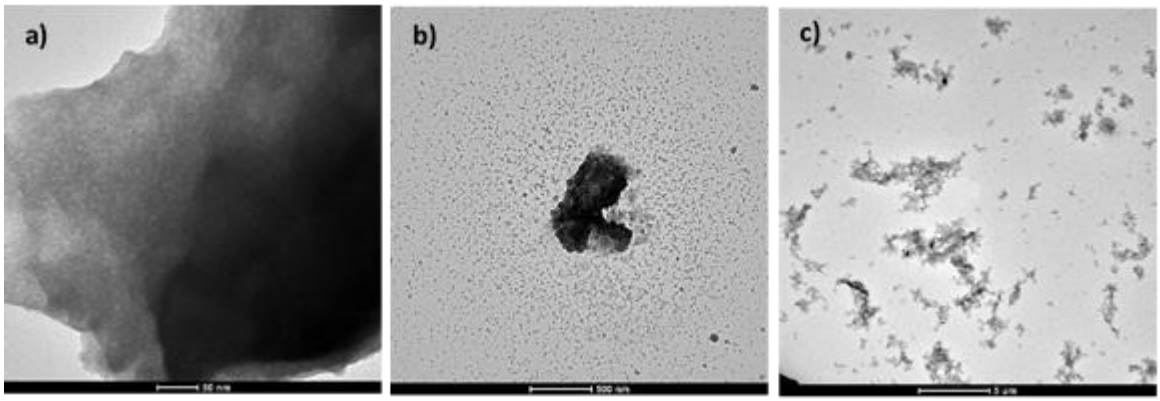

Figure 5.19: TEM micrographs of films that were deposited at a), b) 100°C and c) lower temperature (normally the temperature was set at 60°C, but at this temperature the accuracy of the temperature monitor is very low)

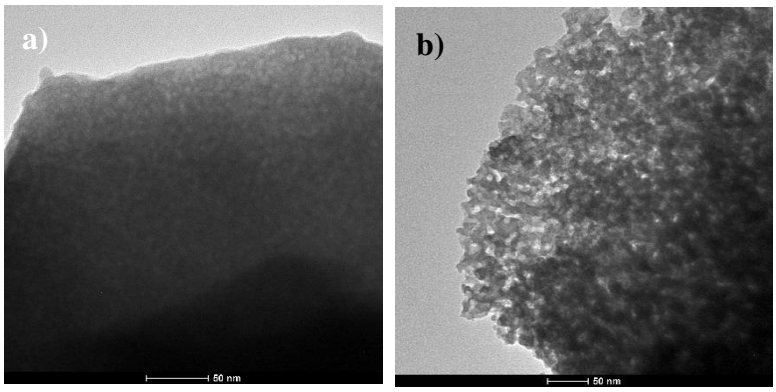

Figure 5.20: TEM micrographs of films deposited at a) 100°C and then stabilized at 150°C for 15 min and b) same as a) but further post-treated at 350°C for 2h

Table 5.5: Electrochemical/Electrochromic properties for the films deposited at different temperatures

Sample	Charge capacity ($mC.cm^{-2}$)*	Normalised charge capacity ($mC.cm^{-2}$)**	R%	$T_{550initial}$%	$T_{550\ col}$%	ΔT_{550} %	η_{550} ($cm^{2}.C^{-1}$)
100°C/350°C,2h	19.6±1.2	18.9±0.7	95±9	85.5	27.7	~59	~40
190°C	21.7±1.3	27.1±2.3	82±10	52.9	21.8	~30	~16
190°C/ O_3, 15min	23.0	28.7	74	69.0	27.2	~32	~14
190°C/ O_3, 30min	25.1	31.2	79	65.5	25.2	~37	~15
290°C	7.1±1.0	16.3±1.2	77±16	86.0	80.6	---	---

* charge capacities were calculated from the 1st cycle of chronoamperometric measurements
** standard deviations for the normalized values and the reversibilities were calculated according to the formula $\frac{Dz}{z} = \sqrt{(\frac{Da}{a})^2 + (\frac{Db}{b})^2 + (\frac{Dc}{c})^2}$ for an equation $z \pm Dz = \frac{(a \pm Da).(b \pm Db)}{c \pm Dc}$
*** The coloration efficiency was calculated from the actual values and not the normalized ones

5.5.2 Electrochemical/Electrochromic properties of the porous films

The electrochromic properties of the films that were deposited at 100°C (post-treated), 190°C and 290°C were studied by chronoamperometry, cyclic voltammetry and ex-situ chronoamperometry/UV-Visible spectrophotometry. The most efficient films were further subjected to coupled UV-Visible/chronoamperometric measurements.

As it is evident from the UV-visible spectra in Figure 5.21 and in the Table 5.5 the most efficient properties in respect to the initial transparency, reversibility, optical contrast and coloration efficiency stemmed from the films that were deposited at 100° and then post-treated at 350°C. It is noteworthy that the optical properties (optical contrast and coloration efficiency) were superior for these films in the whole wavelength range (Figure 5.21 f). Even though the films exhibit their maximum performance in wavelengths over 650 nm, 550 nm was selected as a reference in this study due to the maximum human eye sensitivity at this wavelength [51].

The films that were deposited at 190°C exhibit a slightly better coloration (as a result of the slightly higher charge capacity) but the initial transparency (and subsequently the optical contrast and coloration efficiency) is noticeably less. Subjecting the films to a post ozonolysis treatment for 15 or 30 minutes resulted in the improvement of the initial transparency. However the optical contrast and the coloration efficiency were barely improved. Eventually, all the electrochemical/optical properties were tremendously declined as the deposition temperature of the films increased up to 290°C. At this temperature, the coloration was barely visible anymore (Figure 5.21 e). This result was consistent with the structural characterization of the films described in the previous paragraph and their bad coverage as the temperature increased (Figure 5.15).

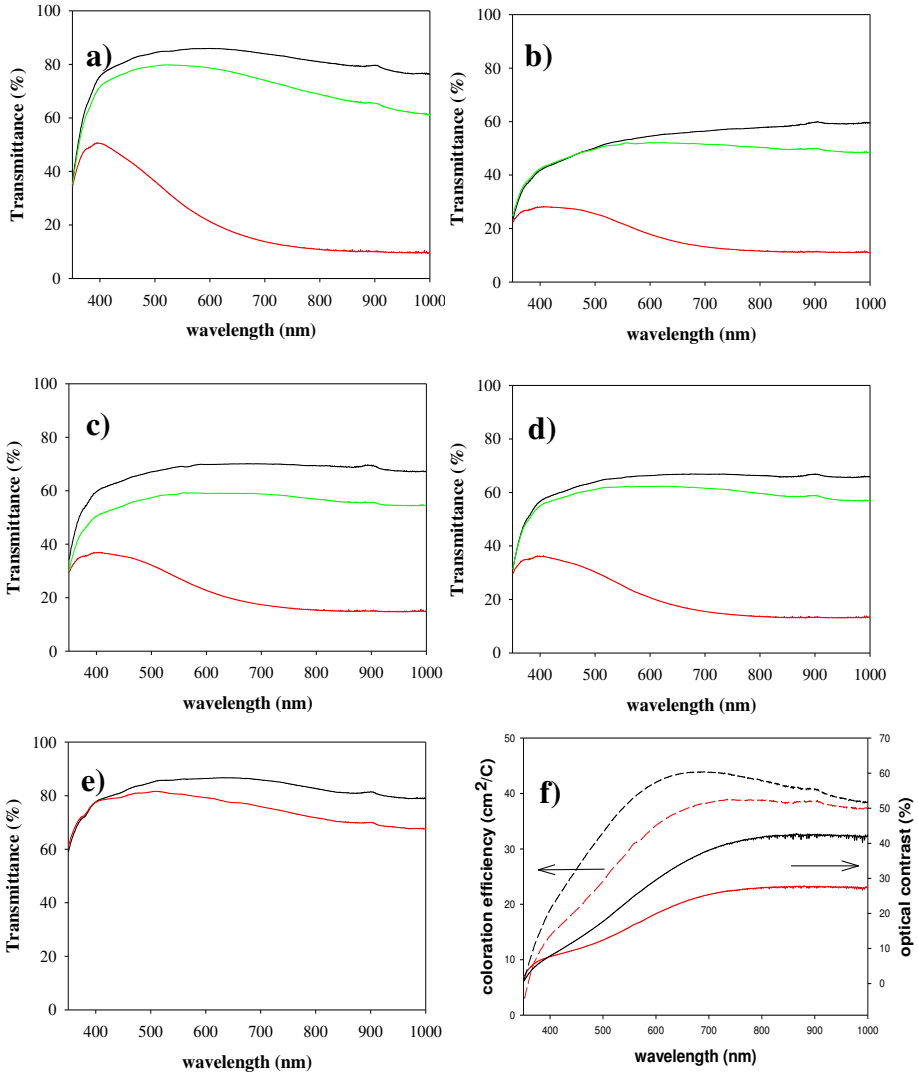

Figure 5.21: UV-visible spectra of the films calcined at different temperatures: a) 100°C/350°C, 2h b) 190°C c) 190°C and then treated with O_3 for 15 mins d) 190°C and then treated with O_3 for 30 mins e) 290°C. The black spectra illustrate the initial transmittances, the red spectra the transmittance of the films at their colored state and the green at their bleached state f) plots of optical contrast and coloration efficiency in function of wavelength. The black plots corresponds to the films deposited at 100°C and the red plots to the films deposited at 190°C

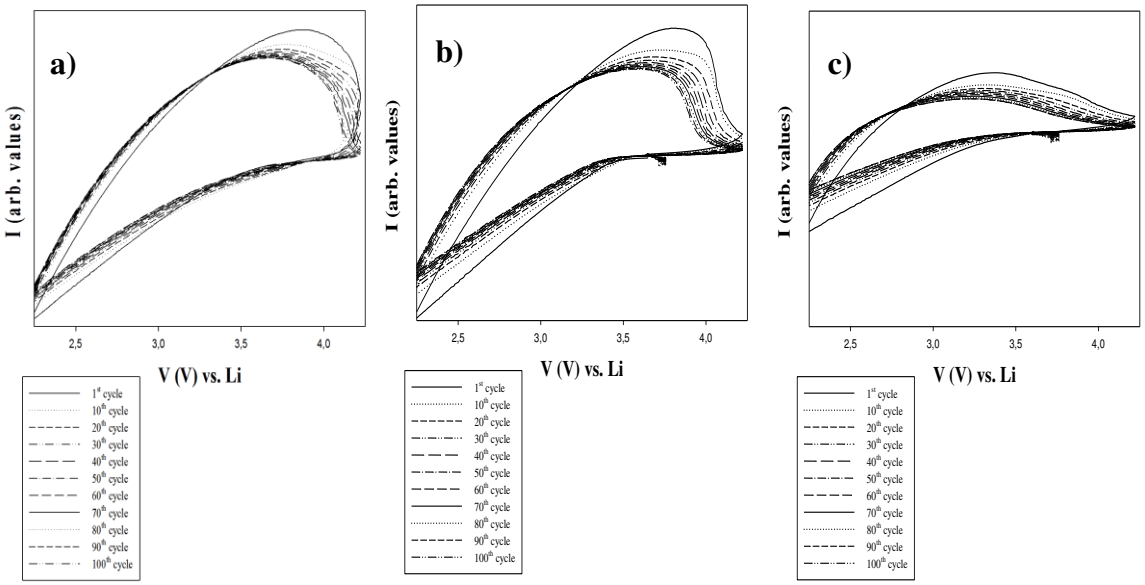

Figure 5.22: Cyclic voltammograms of films deposited at a) 100°C and then post-treated b) 190°C and c) 290°C

The cyclic voltammograms in Figure 5.22 revealed that the films possessed sustainability limitations. More specifically, in all the films there was a gradual degradation observed in the first 100 cycles with more distinct modifications in the first few cycles. This decay can be attributed to the porous and hydrated surface of the films. Moreover, as the deposition temperature increased, the peak potential for the oxidation process was shifting towards less oxidative potentials suggesting that the limiting step for the oxidation rate was related to the amount of W, which decreases as the temperature increases (see Figure 5.14).

Switching kinetics of the films

In Table 5.6, the switching kinetics of the films deposited at 100°C (post-treated), 190°C, 290°C during the 1st and 20th cycle are presented. From the table, it is apparent that the switching kinetics exhibited relatively high standard deviations and the times varied widely from one sample to another, but also over the course of cycling. For example, the switching kinetics of the films were gradually improved as the cycling was evolving (the cycles in between are not shown here). This is most probably due to structural modifications which occur upon lithium insertion and de-insertion which apparently accelerate the electrochemical process. Another explanation for the improved kinetics during cycling is the gradual degradation of the films and the reduced charge capacity in the following cycles (kinetics are associated with the concentration of lithium cations which are inserted). Nevertheless, this vague study revealed that generally all the films exhibited relatively slow coloration and bleaching kinetics compared to reported values in the literature. For example, coloration/bleaching times as fast as 10/6 s have been documented in the literature for templated films which were prepared with the ultrasonic spray deposition [29].

It should be mentioned that by subjecting the films to in-situ electrochemical/UV-Vis measurements the switching kinetics were tremendously improved (Figure 5.23). Based on

the transmittance plots in Figure 5.23, the calculated coloration and bleaching times were 24 s and 6 s respectively for the films that were deposited at 100°C and then post-treated at 350°C and 24 s and 24 s for the films that were deposited at 190°C. This enormous improvement in the coupled measurements for both films is due to the presence of water in the electrolyte and the environmental humidity which are present during the in-situ measurements (see chapter 3) and participate to the electrochemical reaction. In the absence of water and humidity however, it is expected that the coloration/bleaching kinetics calculated from the transmittance and not from the current density are slower. This assumption is based on the work of D-J Kim and S-I Pyun [52] who discussed the involvement of three different sites for cations (protons intercalation in their case): 1) reversibly active sites 2) shallow trap sites (which participate in the coloration process) and 3) deep trap sites (which also participate in the coloration process but they cannot be extracted). Therefore, when the current is the parameter under study, the kinetics of all the inserted electrons (and cations) are taken into consideration. On the other hand, in transmittance measurements only the absorbing centers are accounted for, which are trapped in localized positions in the material and therefore they decelerate the electrochemical process. Nevertheless, in our case the coupled measurements took place in ambient atmosphere while the electrochemical measurements were conducted in an Ar filled glovebox and therefore the two measurements cannot be compared.

Table 5.6: Switching kinetics for the films deposited at different temperatures

Sample*	t_c (s) (1st cycle)	t_c (s) (20th cycle)	t_b (s) (1st cycle)	t_b (s)(20th cycle)
100°C/350°C,2h	224±4**	199±23	130±55	60±7
190°C	272	205±41	73±6	50±8
290°C	102±20	65±13	22±8	19±5

*Two of the four measurements that were performed obtained t_c>240s. Since we did not possess the exact values, these measurements were not included in the calculation of the standard deviations. Therefore, the latter is much higher than reported

**all the switching times were defined as the time needed for the maximum current to reach the 10% of its value

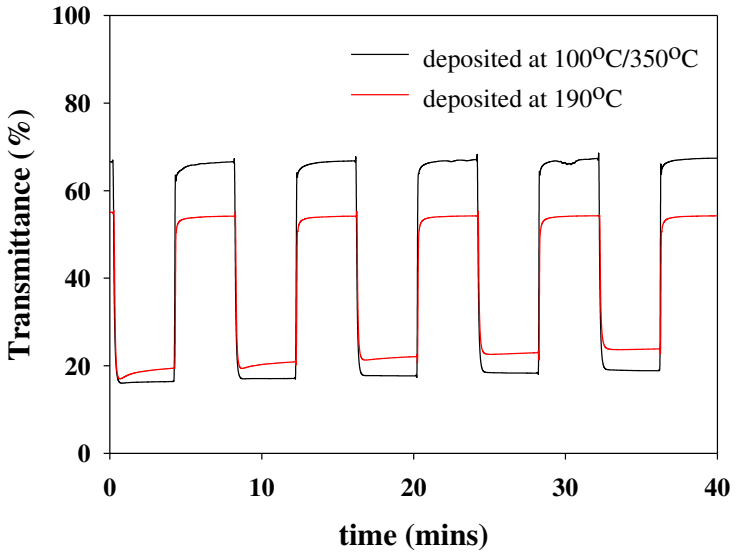

Figure 5.23: In-situ chronoamperometric UV-Vis spectra for the porous films deposited at 100°C (and then stabilized at 350°C for 2h) and at 190°C

5.5.3 Effect of the surfactant

As it was discussed in paragraph 5.2.3, surfactants are very popular additives in the films science. They improve solution wettability on the substrate (and thus its spreading properties) and they act as templating agents for the introduction of porosity when it is desired. Additionally, in the USP process, surfactants reduce droplets size, which eventually determines films deposition. In this work, an oligomer (Brij-56, $C_{16}H_{33}(EO)_{10}$) was used as a templating agent. Until now, all the films that have been described in this chapter, were formed in the presence of Brij-56. In the following paragraphs, a structural and electrochemical characterization of films without surfactant will be presented and through this discussion the role of the latter will be highlighted. In some cases, for the sake of comparison, the studies of the templated films which have already been discussed in the previous paragraphs will be displayed again. For this discussion, two types of films have been prepared at two different temperatures: 1) 100°C and then post-treated at 350°C for 2h and 2) 190°C.

Microstructure, appearance, thickness and amount of W oxide in the films without surfactant

From the SEM micrographs in Figure 5.24 it is straightforward that surfactants substantially influence the deposition of the droplets and eventually the films coating. The films deposited at 100°C and then post-treated at 350°C for 2h possess a rough surface which consists of disordered ring-like features. Subsequently, two regions can be distinguished inside the films: matter-rich regions (the perimeter of the rings) which contain cracks and matter-free regions (bare regions) in between and in the center of the rings. The films that have been obtained at the same thermal treatment in the presence of a surfactant (Figure 5.15 a and b), contain cracks as well, however they exhibit a smooth, homogeneous and a continuous morphology.

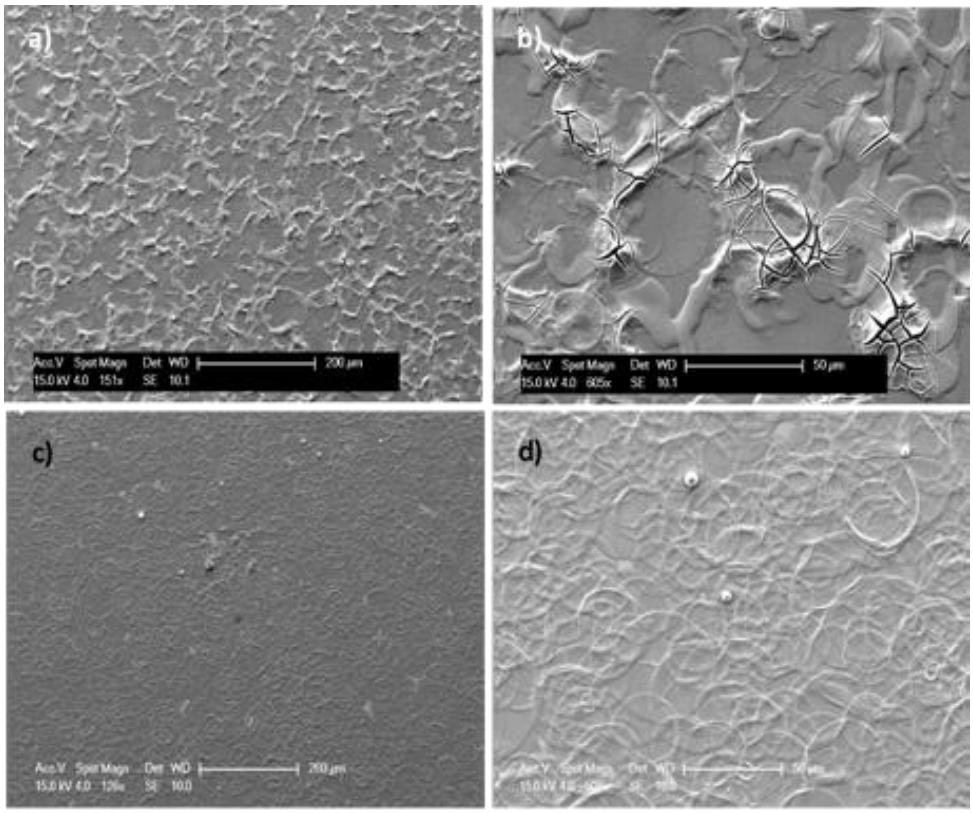

Figure 5.24: SEM micrographs of films deposited without surfactant at: a), b) 100°C and then post-treated at 350°C and c), d) 190°C

Similarly, at 190°C (Figure 5.24 c, d) and in the absence of a surfactant, individual well-shaped superimposed ring-like features are apparent and the films are not continuous. As it was discussed in paragraph 5.2.5 the ring-like features are typically observed in the spraying processes under certain conditions (low precursor concentration, low deposition temperatures) and they are associated with the non-uniform evaporation rate inside the droplet and/or the movement of the material on the substrate due to capillary forces. On the other hand the corresponding templated films (Figure 5.15 c, d) are continuous with crater-like imprints of gaseous products.

In essence, the presence of a surfactant during the spraying process enables the formation of smooth and continuous films rather that individually superimposed drained droplets.

Because of the latter, profilometry mesaurements did not lead to any valuable information for the non-templated films. Instead, profilograms with large fluctuations and lack of the characteristic ‘’step’’, emerged from this investigation (data not shown).

Moreover, because of the inhomogeneous microstructure presented in Figure 5.24, the films without surfactant appear to be somewhat hazier compared to the templated ones.

The non-templated films have been also subjected into EDX measurements in order to calculate the k-ratio and the results are presented in Figure 5.25. Due to the lack of surfactant, the amount of W oxide that is deposited is somewhat higher compared to the templated films which were sprayed under identical experimental conditions.

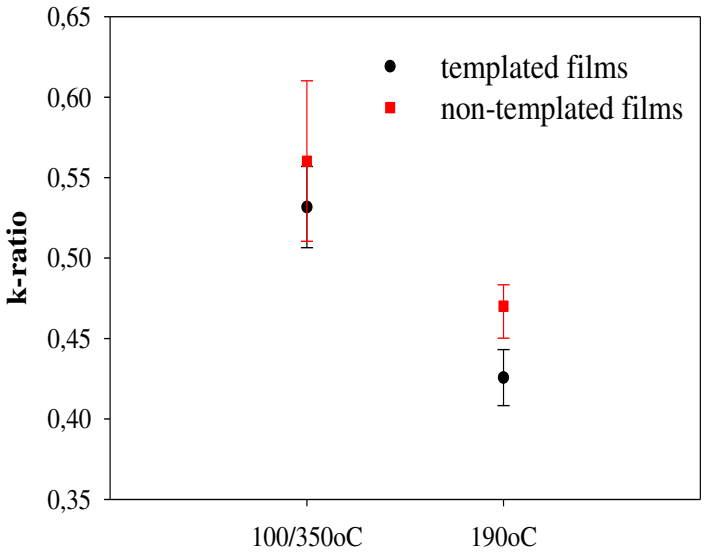

Figure 5.25: Mean values of the k-ratio (with their standard deviations) calculated from EDX measurements for the non-templated films (red squares). In black circles, the relative k-ratios for the templated films are illustrated for comparative purposes

Crystallinity of the films

Based on the discussion in chapter 3 for the dip-coated films, in the absence of a templating agent, crystallization initiates at lower temperatures.

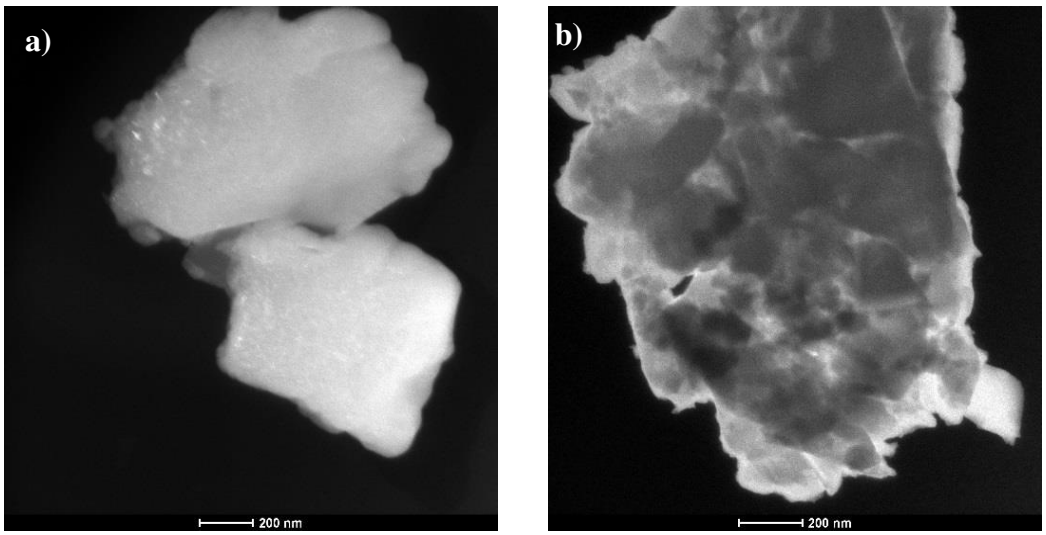

Figure 5.26: Dark-field micrographs of non-templated films deposited at a) 100°C and then post-treated at 350°C for 2h b) 190°C

Surprisingly, the sprayed non-templated films which were deposited at 100°C and then post- treated at 350°C for 2h, are amorphous according to X-Ray Diffraction. Dark-field micrographs (Figure 5.26 a) revealed the occurrence of some random crystallites which are not determining for the films properties. The reasons for this delay in sprayed films is not clear but it might be associated with the ‘’particular’’ microstructure of the films. As it was previously discussed, discrete ring-like features are comprising the non-templated films

which constrain materials networking and presumably the formation of crystal nuclei. Likewise, the films deposited at 190ºC are completely amorphous (Figure 5.26 b).

Structural characterization by infrared spectroscopy

Figure 5.27 and Table 5.7 present the infrared bands of the non-templated films. Both films possess somewhat less hydrophilic surface compared to the templated ones (Figure 5.17), as inferred by the absence of surface hydroxyl groups at ~3000 cm^{-1}.

The non-templated films deposited at 100ºC and then post-treated at 350ºC for 2h, are almost unhydrous. A single well-shaped peak at 658 cm^{-1} characterizes these films, which is attributed to the stretching vibration of W-O-W bonds. The shoulder at 938 cm^{-1} corresponding to the W=O groups confirms the amorphous nature of this material, however the relatively narrow W-O-W peak implies that a big part of it is already well structured.

On the other hand, at 190ºC almost no material is deposited on silicon wafers with 2 spraying passages in contrast to the templated films. This is due to the absence of the surfactant which acts as a wetting agent and improves the solution's wettability on different substrates (see paragraph 5.2.3) and/or presumably to the lighter weight of the droplets which are drawn away by the exertion of the thermophoretic forces. At this temperature, the main peak at around 600 cm^{-1} is split (668, 653, 595 cm^{-1}) and most likely the W-O-W network is in a very preliminary stage.

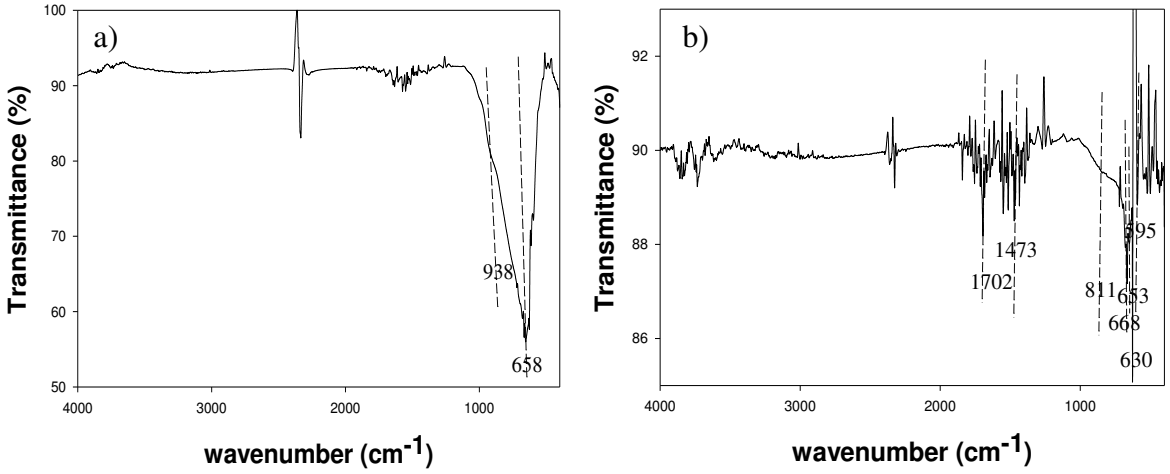

Figure 5.27: IR spectra of the non-templated films deposited at a) 100ºC and then post-treated at 350ºC for 2h and b) 190ºC

Table 5.7: Infrared peaks and their assignments for the non-templated films. As a comparison the corresponding templated films are presented as well

	Film deposited at 100°C and calcined at 350°C (templated)	Film deposited at 100°C and calcined at 350°C (non-templated)	Film deposited at 190°C (templated)	Film deposited at 190°C (non-templated)	Peak origin[1]	Ref.
ν (cm^{-1})	3124		3374		ν(OH)	[47, 48]
			1693,1620	1702	δ(HOH) (structural)	[47]
			1563, 1541		$\nu_{asym}(COO)_{bi}$ (free acetate) bidentate chelating	[45]
			1499	1472	ν_{OH}, δ_{OH} (OH bonded with either water molecules or to surface oxygen atoms, W-O	[45, 48]
			1460 1417		$\nu_{sym}(COO)_{bi}$ (bidentate chelating) free acetate or $\delta(CH_3)$	[45]
		938			ν(W=O) (terminal modes of surface grains)	[48]
			872		ν(O-O) and $W\text{-}O\text{-}W_{intra}$	[45]
				811	$\nu(W\text{-}O\text{-}W)_{intra}$ of W_3O_{13} edge sharing units	[50]
	670		671	668	$\nu_{asym}(O\text{-}W\text{-}O)$, (C-H), (COO), δ(O-C=O)	[45]
		650	630	653, 630	$\nu_{asym}(W\text{-}O\text{-}W)$	[45, 50]
			595		Not found elsewhere, presumably some long W-O band	

Porosity of the films without surfactant

The non-templated films are expected to be devoid of porosity or to possess lower specific surface area. This is implicitly inferred by the IR spectra in Figure 5.27 and the absence of peaks attributed to interacting water molecules. The compact structure of the non-templated films is corroborated with the TEM micrographs (Figure 5.28 a, c). However, in some other regions (Figure 5.28 b, d) the nano-morphology becomes more structured giving the notion of porosity. For the moment, no explanation could be given for this unexpected phenomenon. Contamination of the pumping tube or the nozzle was one of the possible explanations but the extra precautions that have been taken (excessive rinsing with water and ethanol) did not lead to any different results.

Unfortunately, the presence of porosity in the non-templated films could not be further verified with ellipsometric measurements due to their hazy appearance. Nevertheless, in this manuscript it is presumed that the non-templated films possess lower specific surface area compared to the templated films. This assumption is enhanced by the substantially inferior electrochromic properties of the non-templated films compared to the templated ones as it will be shown in the next paragraph.

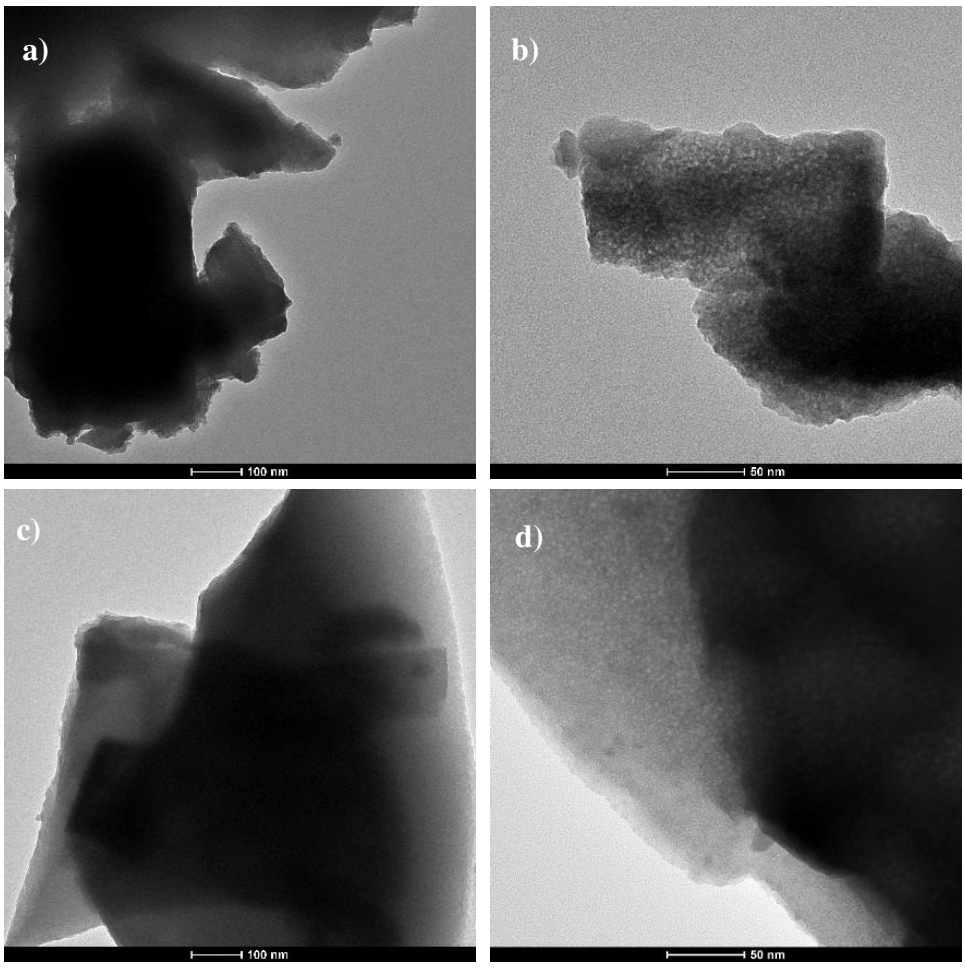

Figure 5.28: TEM micrographs of non-templated films deposited at a, b) 100°C and then post-treated at 350°C, 2h and c, d) 190°C

5.5.4 Electrochemical/Electrochromic properties of the dense films

In accordance with the problematic structural properties of the non-templated films presented in Figure 5.24 and their presumably lower surface area, Figure 5.29 and Table 5.8 state their limited electrochemical/optical properties. Both types of films exhibit weak coloration and subsequently low optical contrast and coloration efficiency. It should be pointed out that regardless the relatively high amount of W (see k-ratio in Figure 5.25) in the non-templated films, their charge capacities are significantly low. Apparently, the compact structure and/or the non-continuous morphology impede lithium cations from intercalating inside the films.

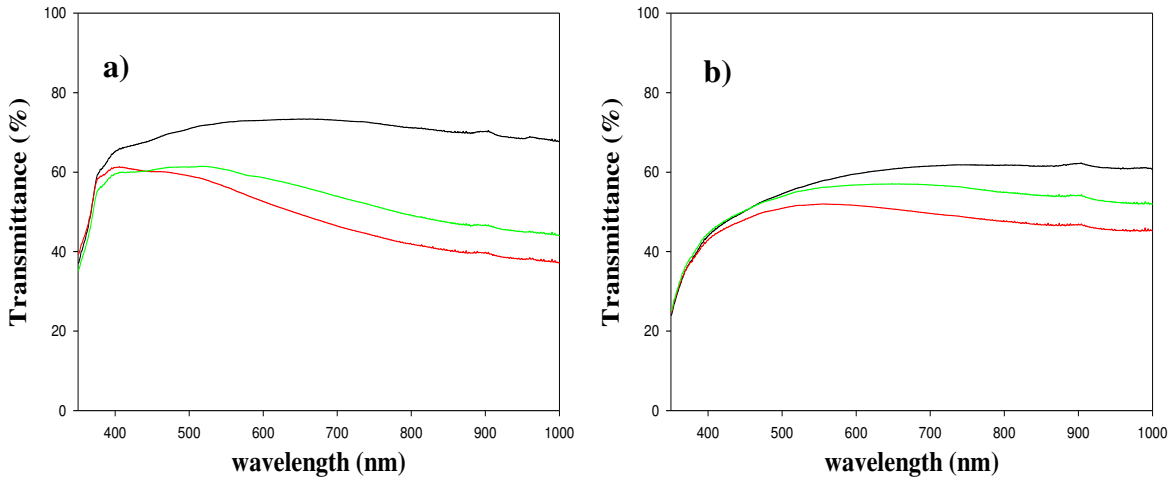

Figure 5.29: UV-visible spectra of the non-templated films deposited at a) 100°C and then post-treated at 350°C and b) 190°C. The black spectra illustrate the initial transmittances, the red spectra the transmittance of the films at their colored state and the green at their bleached state

Moreover, both films remain blue after the electrochemical measurements which signifies that the low amount of lithium cations which intercalates remains inside the films. This observation is in accordance with the discussion on the non-templated dip-coated films in chapter 3.

Table 5.8: Electrochemical/Electrochromic properties for the non-templated films

Sample	Charge capacity ($mC.cm^{-2}$)	R%	$T_{550initial}$%	$T_{550\ col}$%	ΔT_{550} %	η_{550} ($cm^{-2}.C^{-1}$)
100°C/350°C,2h	5.36±0.05	48±5	73	56	~4	~6
190°C	2.64±0.05	70±3	58	52	~7	~19

In accordance with the dip-coating study, faster switching kinetics are characterizing the non-templated films compared to their templated counterparts. As it was discussed before, this is probably associated to the substantial capacity difference and the amount of Li^+ which (de)intercalates in each case.

Table 5.9: Switching kinetics for the non-templated films

Sample	t_c (s) 1st cycle)	t_c (s) (20th cycle)	t_b (s) (1st cycle)	t_b (s) (20th cycle)
100°C/350°C,2h	170±24	78±11	19±4	16±2
190°C	60±19	35±4	14±1	12±1
100°C/350°C,2h (porous)	224±4	199±23	130±55	60±7
190°C (porous)	272	205±41	73±6	50±8

5.6 Conclusions

In this chapter, we studied the influence of the surfactant and the deposition temperature in the structural and electrochemical properties of USP-prepared tungsten oxide films.

For this reason, films were deposited at 100°C (and then post-treated at 350°C), 190°C, 290°C and 390°C in the presence of Brij-56.

As the deposition temperature increased, we observed that the amount of tungsten deposited on the films was noticeably decreased (based on k-ratio measurements). Owing to this phenomenon, the coverage of the substrates at high temperatures was rendered very difficult even when the number of layers was considerably increased. The thermophoretic forces which drag the smaller droplets away and/or the Leiderfrost effect (vapor cushions which inhibit the deposition of the droplets) are reported in the literature to be responsible for this effect.

SEM micrographs showed that continuous films are obtained only at the two lower deposition temperatures (100°C and 190°C). However, both types of films present several cracks. At 190°C extra round crater-like features are obtained which are probably stemming from the precursor decomposition and the subsequent formation of gaseous byproducts. Discrete droplets sparsely distributed on the substrate were emerged when the temperature was increased at 290°C while a powdery product precipitated at 390°C.

The most two interesting films (100°C/350°C and 190°C) look hazy with naked eye. This is probably attributed either to the non-uniform packing of the droplets, to the presence of cracks and/or to the formation of gaseous products' imprints on the surface of the films. The opaque appearance of films is a restraining factor for their good quality and their potential industrial application and further work should be carried out in order to solve this drawback.

The films were also studied by infrared spectroscopy. The spectra showed that the films that were deposited at 100°C still contain the precursor and the surfactant while only traces of the precursor are present in the film deposited at 190°C. At this temperature, most part of the precursor is converted into tungsten oxide and the surfactant is completely decomposed. At higher temperatures (post-treatment at 350°C and deposition at 390°C), tungsten oxide is the only component of the films.

Interestingly, TEM micrographs depicted that the films (except the ones deposited at 390°C which were not studied) contain well distinct pores. Therefore, in this study it is proofed that templating is a strategy that can be successfully combined with the spraying process.

It appears that the presence of the surfactants not only induces porosity in the films but it also improves the solution coating properties and its spreading on the substrate surface. SEM micrographs illustrated that in the absence of a surfactant, a continuous layer cannot be achieved with this precursor at any temperature but rather rough surfaces with disordered ring-like features are observed.

Based on TEM micrographs some porous entities similar to the templated films have been detected in the non-templated films under the TEM microscope. This might be attributed to instrumental contamination due to insufficient cleaning at the end of the experimental process. Nevertheless, based on IR spectra, the emerging tungsten oxide is considered to be mostly un-hydrous, which enhances the assumption that the non-templated films are pores-free. This is further corroborated with the fact that the electrochemical (and optical properties) of these films are substantially inferior compared to the templated films.

The templated films (100ºC/350ºC and 190ºC) exhibit high reversibility (95 and 82% respectively), optical contrast (59 and 30%) and coloration efficiencies (40 and 16%). The films that were deposited at 190ºC present slightly better coloration compared to the films that were deposited at 100ºC (and then post-treated at 350ºC) but due to the lower initial transparency all the optical quantities are much lower. Moreover, the cyclic voltammograms revealed that the porous films are lacking long-term stability. This limitation is attributed to the porous and hydrated nature of the films.

Finally, the films exhibit somewhat slow switching kinetics. For example, around 4 min are needed to color the film that was deposited at 100ºC (and post-treated at 350ºC) and around 3 min to bleach it.

Nevertheless, despite the number of drawbacks listed above for the produced films, it has been proven that ultrasonic spray pyrolysis is a powerful tool especially when successfully combined with the templating method. Cost-effectiveness, fast and continuous production rates, without requiring vacuum conditions have established the ultrasonic spray pyrolysis as a large-scale production line method for transparent layers. In this study, we further proved that when surfactants are incorporated in the experimental process, the solution spreading quality is substantially improved and continuous films at higher maximum deposition temperatures can emerge. The latter, can also be beneficial for large-scale applications since the whole process is completed in one step and no post-thermal treatment is required. Additionally, the successful induction of porosity through the templating process enhances the electrochromic performance and it ensues films with relatively high coloration efficiency, optical contrast and reversibility.

5.7 References for Chapter 5

[1] D. Perednis, L. Gauckler, Thin Film Deposition Using Spray Pyrolysis, J Electroceram, 14 (2005) 103-111.

[2] R.R. Chamberlin, J.S. Skarman, Chemical Spray Deposition Process for Inorganic Films, Journal of the Electrochemical Society, 113 (1966) 86-89.

[3] G.L. Messing, S.-C. Zhang, G.V. Jayanthi, Ceramic Powder Synthesis by Spray Pyrolysis, Journal of the American Ceramic Society, 76 (1993) 2707-2726.

[4] J.B. Mooney, S.B. Radding, Spray Pyrolysis Processing, Annual Review of Materials Science, 12 (1982) 81-101.

[5] D. Perednis, O. Wilhelm, S.E. Pratsinis, L.J. Gauckler, Morphology and deposition of thin yttria-stabilized zirconia films using spray pyrolysis, Thin Solid Films, 474 (2005) 84-95.

[6] A. Nakaruk, C.C. Sorrell, Conceptual model for spray pyrolysis mechanism: fabrication and annealing of titania thin films, J Coat Technol Res, 7 (2010) 665-676.

[7] Sonotek corporation, investor presentation, (February 2013).

[8] W.-N. Wang, A. Purwanto, I.W. Lenggoro, K. Okuyama, H. Chang, H.D. Jang, Investigation on the Correlations between Droplet and Particle Size Distribution in Ultrasonic Spray Pyrolysis, Industrial & Engineering Chemistry Research, 47 (2008) 1650-1659.

[9] C. Guild, S. Biswas, Y. Meng, T. Jafari, A.M. Gaffney, S.L. Suib, Perspectives of spray pyrolysis for facile synthesis of catalysts and thin films: An introduction and summary of recent directions, Catalysis Today, 238 (2014) 87-94.

[10] M.S. Tomar, F.J. Garcia, Spray pyrolysis in solar cells and gas sensors, Progress in Crystal Growth and Characterization, 4 (1981) 221-248.

[11] D. Perednis, L.J. Gauckler, Solid oxide fuel cells with electrolytes prepared via spray pyrolysis, Solid State Ionics, 166 (2004) 229-239.

[12] D. Beckel, A. Dubach, A.R. Studart, L.J. Gauckler, Spray pyrolysis of La0.6Sr0.4Co0.2Fe0.8O3-δ thin film cathodes, J Electroceram, 16 (2006) 221-228.

[13] U.P. Muecke, N. Luechinger, L. Schlagenhauf, L.J. Gauckler, Initial stages of deposition and film formation during spray pyrolysis — Nickel oxide, cerium gadolinium oxide and mixtures thereof, Thin Solid Films, 517 (2009) 1522-1529.

[14] J. Morales, L. Sánchez, F. Martín, J.R. Ramos-Barrado, M. Sánchez, Use of low-temperature nanostructured CuO thin films deposited by spray-pyrolysis in lithium cells, Thin Solid Films, 474 (2005) 133-140.

[15] R. Ayouchi, F. Martin, J.R. Ramos Barrado, M. Martos, J. Morales, L. Sánchez, Use of amorphous tin-oxide films obtained by spray pyrolysis as electrodes in lithium batteries, Journal of Power Sources, 87 (2000) 106-111.

[16] J.L.M. Rupp, A. Infortuna, L.J. Gauckler, Microstrain and self-limited grain growth in nanocrystalline ceria ceramics, Acta Materialia, 54 (2006) 1721-1730.

[17] U.P. Muecke, G.L. Messing, L.J. Gauckler, The Leidenfrost effect during spray pyrolysis of nickel oxide-gadolinia doped ceria composite thin films, Thin Solid Films, 517 (2009) 1515-1521.

[18] A. Furusaki, H. Konno, R. Furuichi, Perovskite-type lanthanum chromium-based oxide films prepared by ultrasonic spray pyrolysis, Journal of Materials Science, 30 (1995) 2829-2834.

[19] M. Duta, D. Perniu, A. Duta, Photocatalytic zinc oxide thin films obtained by surfactant assisted spray pyrolysis deposition, Applied Surface Science, 306 (2014) 80-88.

[20] H. Kamal, E.K. Elmaghraby, S.A. Ali, K. Abdel-Hady, The electrochromic behavior of nickel oxide films sprayed at different preparative conditions, Thin Solid Films, 483 (2005) 330-339.

[21] J. Denayer, G. Bister, P. Simonis, P. Colson, A. Maho, P. Aubry, B. Vertruyen, C. Henrist, V. Lardot, F. Cambier, R. Cloots, Surfactant-assisted ultrasonic spray pyrolysis of nickel oxide and lithium-doped nickel oxide thin films, toward electrochromic applications, Applied Surface Science, 321 (2014) 61-69.

[22] A. Enesca, A. Duta, Tailoring WO_3 thin layers using spray pyrolysis technique, Physica Status Solidi C: Current Topics in Solid State Physics, 5 (2008) 3499-3502.

[23] J. Arakaki, R. Reyes, M. Horn, W. Estrada, Electrochromism in NiOx and WOx obtained by spray pyrolysis, Solar Energy Materials and Solar Cells, 37 (1995) 33-41.

[24] L.M. Bertus, C. Faure, A. Danine, C. Labrugere, G. Campet, A. Rougier, A. Duta, Synthesis and characterization of WO3 thin films by surfactant assisted spray pyrolysis for electrochromic applications, Materials Chemistry and Physics, 140 (2013) 49-59.

[25] L.M. Bertus, A. Duta, Synthesis of WO3 thin films by surfactant mediated spray pyrolysis, Ceramics International, 38 (2012) 2873-2882.

[26] J. Denayer, P. Aubry, G. Bister, G. Spronck, P. Colson, B. Vertruyen, V. Lardot, F. Cambier, C. Henrist, R. Cloots, Improved coloration contrast and electrochromic efficiency of tungsten oxide films thanks to a surfactant-assisted ultrasonic spray pyrolysis process, Solar Energy Materials and Solar Cells, 130 (2014) 623-628.

[27] S.R. Bathe, P.S. Patil, Titanium doping effects in electrochromic pulsed spray pyrolysed WO_3 thin films, Solid State Ionics, 179 (2008) 314-323.

[28] S.R. Bathe, P.S. Patil, Electrochromic characteristics of fibrous reticulated WO_3 thin films prepared by pulsed spray pyrolysis technique, Solar Energy Materials and Solar Cells, 91 (2007) 1097-1101.

[29] C.-P. Li, F. Lin, R.M. Richards, C. Engtrakul, A.C. Dillon, R.C. Tenent, C.A. Wolden, Ultrasonic spray deposition of high performance WO_3 films using template-assisted sol–gel chemistry, Electrochemistry Communications, 25 (2012) 62-65.

[30] C.-P. Li, F. Lin, R.M. Richards, C. Engtrakul, R.C. Tenent, C.A. Wolden, The influence of sol–gel processing on the electrochromic properties of mesoporous WO_3 films produced by ultrasonic spray deposition, Solar Energy Materials and Solar Cells, 121 (2014) 163-170.

[31] P.S. Patil, P.R. Patil, E.A. Ennaoui, Characterization of ultrasonic spray pyrolyzed tungsten oxide thin films, Thin Solid Films, 370 (2000) 38-44.

[32] M. Regragui, M. Addou, A. Outzourhit, J.C. Bernéde, E. El Idrissi, E. Benseddik, A. Kachouane, Preparation and characterization of pyrolytic spray deposited electrochromic tungsten trioxide films, Thin Solid Films, 358 (2000) 40-45.

[33] V.R. Shinde, S.B. Mahadik, T.P. Gujar, C.D. Lokhande, Supercapacitive cobalt oxide (Co3O4) thin films by spray pyrolysis, Applied Surface Science, 252 (2006) 7487-7492.

[34] J.D. Desai, H.M. Pathan, S.-K. Min, K.-D. Jung, O.-S. Joo, Preparation and characterization of iron oxide thin films by spray pyrolysis using methanolic and ethanolic solutions, Applied Surface Science, 252 (2006) 2251-2258.

[35] J.M. Bian, X.M. Li, T.L. Chen, X.D. Gao, W.D. Yu, Preparation of high quality MgO thin films by ultrasonic spray pyrolysis, Applied Surface Science, 228 (2004) 297-301.

[36] R. Neagu, D. Perednis, A. Princivalle, E. Djurado, Initial Stages in Zirconia Coatings Using ESD, Chemistry of Materials, 17 (2005) 902-910.

[37] C. Chen, E.M. Kelder, P.J.J.M. van der Put, J. Schoonman, Morphology control of thin LiCoO2 films fabricated using the electrostatic spray deposition (ESD) technique, Journal of Materials Chemistry, 6 (1996) 765-771.

[38] D.T. Gillaspie, R.C. Tenent, A.C. Dillon, Metal-oxide films for electrochromic applications: present technology and future directions, Journal of Materials Chemistry, 20 (2010) 9585-9592.

[39] R. Rajan, A.B. Pandit, Correlations to predict droplet size in ultrasonic atomisation, Ultrasonics, 39 (2001) 235-255.

[40] <SONO TEK CORP - 8-K - 20130207 - EXHIBIT_99.pdf>.

[41] J.C. Viguié, J. Spitz, Chemical Vapor Deposition at Low Temperatures, Journal of the Electrochemical Society, 122 (1975) 585-588.

[42] W. Siefert, Properties of thin In_2O_3 and SnO_2 films prepared by corona spray pyrolysis, and a discussion of the spray pyrolysis process, Thin Solid Films, 120 (1984) 275-282.

[43] A. Cremonesi, Y. Djaoued, D. Bersani, P. Lottici, Micro-Raman spectroscopy on polyethylene-glycol assisted sol–gel meso and macroporous WO_3 thin films for electrochromic applications, Thin Solid Films, (2007).

[44] M. Deepa, M. Kar, D.P. Singh, A.K. Srivastava, S. Ahmad, Influence of polyethylene glycol template on microstructure and electrochromic properties of tungsten oxide, Solar Energy Materials and Solar Cells, 92 (2008) 170-178.

[45] N. Sharma, M. Deepa, P. Varshney, S.A. Agnihotry, FTIR and absorption edge studies on tungsten oxide based precursor materials synthesized by sol–gel technique, Journal of Non-Crystalline Solids, 306 (2002) 129-137.

[46] C.G. Granqvist, Transparent conductors as solar energy materials: A panoramic review, Solar Energy Materials and Solar Cells, 91 (2007) 1529-1598.

[47] M. Deepa, M. Kar, S.A. Agnihotry, Electrodeposited tungsten oxide films: annealing effects on structure and electrochromic performance, Thin Solid Films, 468 (2004) 32-42.

[48] V.D.-G. J. Diaz-Reyes, A. Perez-Benitez, J.A. Balderas-Lopez, Obtaining of film of tungsten trioxide (WO3) by resistive heating of a tungsten filament, <Superficies y Vacío 21 (2008) 12-17.

[49] W. Wang, Y. Pang, S.N.B. Hodgson, Preparation, characterisation and electrochromic property of mesostructured tungsten oxide films via a surfactant templated sol–gel process from tungstic acid, Journal of Sol-Gel Science and Technology, 54 (2010) 19-28.

[50] B. Orel, N. Grošelj, U.O. Krašovec, R. Ješe, A. Georg, IR Spectroscopic Investigations of Gasochromic and Electrochromic Sol-Gel—Derived Peroxotungstic Acid/Ormosil Composite and Crystalline WO_3 Films, Journal of Sol-Gel Science and Technology, 24 (2002) 5-22.

[51] H.M.A. Soliman, A.B. Kashyout, M.S. El Nouby, A.M. Abosehly, Effect of hydrogen peroxide and oxalic acid on electrochromic nanostructured tungsten oxide thin films, International Journal of Electrochemical Science, 7 (2012) 258-271.

[52] D.-J. Kim, S.-I. Pyun, Hydrogen transport through rf-magnetron sputtered amorphous WO3 film with three kinds of hydrogen injection sites, Solid State Ionics, 99 (1997) 185-192.

Chapter 6
Conclusions/Perspectives

6.1 Conclusions

In this dissertation we studied the synthesis of mesoporous tungsten oxide thin films via the soft-templating technique and we investigated the impact of porosity on their electrochemical/electrochromic properties.

Owing to their high surface area, porous films are able to enhance the materials performance by allowing a better penetration of the electrolyte in the bulk. Subsequently, higher cation flux and shorter diffusion paths can be obtained which can be translated into better switching kinetics, coloration efficiencies, optical contrast and reversibilities.

In this study, we selected to produce mesoporous tungsten oxide films via three techniques: ***dip-coating*** a conventional technique which is frequently employed for the formation of porous films. Next, we investigated the possibility of preparing porous templated films with the ***electrodeposition*** method. Finally we used ***spray pyrolysis***, a technique not so commonly combined with templating in order to primarily proof the combatibility of these two methods and then to study the electrochemical/optical properties of the emerging films.

In ***dip-coating***, a long range organized architecture is obtained with Brij-56 with pores sizes of about 2 nm and wall thicknesses of 3 nm. With a larger tri-block copolymer (F127), a worm-like architecture is obtained in the uncalcined film, however with further thermal annealing the porous structure is collapsed. This was attributed to the fact that F127 contains higher hydrophilic segments which interact more strongly with the inorganic network, rendering the material more vulnerable towards thermal treatment. Based on ellipsometric measurements, the calcined Brij-56 templated films contain 23% of porosity while F127 templated films contain 12% of porosity.

The main drawback of dip-coated films is the occurrence of cracks and the inconsistent thickness. Unfortunately, all the attempts which were realized to address this drawback did not lead to any improvement of the quality of the films.

Based on our electrochemical measurements in ambient and inert environment, we showed that the atmospheric water in the electrolyte and the abundance of water molecules and hydroxyls in the porous films, modify the electrochemical reaction. Probably protons are intercalating and de-intercalating along with the lithium cations and/or the abundant W-OH groups in the porous films release protons in exchange of lithium cations. The implication of water in the electrochemical processes, improved the switching kinetics, and the reversibility of the porous films in ambient atmosphere. On the contrary, when the experiments were conducted in a glovebox, porous films exhibited much slower kinetics compared to the dense films. This is probably due to the lack of excess water in the electrolyte, but also to the substantially higher charge capacity of the porous films which might create a barrier in the interface between the electrolyte and the film. Despite the much lower W content in porous films they intercalate almost 3 times more lithium cations than the compact films. This infers than the flat surface of the dense film does not permit the penetration of the cations in the interior of the films. Noteworthy, the dense films lose almost half of their capacity in the first cycle and they remain blue after the electrochemical measurements.

The dip-coated films have been also studied via Raman spectroscopy in ambient environment before, during intercalation and after lithium de-intercalation. It was found that lithium cations not only reside in the channels of the perovskite-like WO_3 but they interact with the surface of the films by disrupting the inorganic network. This is more distinct in the porous films, whose surface/bulk ratio is higher. This might explain the somewhat faster degradation of these films upon consecutive cycling. The irreversibility of the dense films was also noticeable in Raman spectra. More specifically, a new phase was detected which according to the literature was attributed to the formation of Li_xWO_3 nanocrystallites. This suggests that the intercalation of lithium cations can increase the degree of crystallinity of the films, but further investigations should be carried out in order to confirm this assumption.

Next, we investigated the possibility of producing mesoporous tungsten oxide films through ***electrodeposition.*** Two different surfactants have been tested for this purpose one non-ionic (Brij-56) and one anionic (PSS-Na). However, mesoporous films via this method appeared to be a challenging task and further investigations should be carried out in order to optimize all the experimental parameters. Low coverage, no strong evidences of porosity, lack of reproducibility and low electrochemical properties are some of the problems encountered in this chapter.

In the Brij-56 systems, the films exhibit a granular morphology despite of the content of the surfactant in the plating solution. There is some evidence of porosity based on TEM micrographs but no direct proof that templating is indeed taking place.

Similarly, in PSS-Na systems, some random evidences of templating have been found as well. However, the porosity occurs in a very low degree in the films and most part appears to be dense and compact.

In the last part of this dissertation, we synthesized templated porous films via the ultrasonic spray pyrolysis method. More specifically we investigated the role of deposition temperature and the surfactant on the structural and electrochromic properties of the films.

For example, we observed that as the deposition temperature increased, the amount of tungsten deposited on the films was noticeably decreased. Owing to this phenomenon, the coverage of the substrates at high temperatures was rendered very difficult even when the number of layers was considerably increased.

SEM micrographs showed that continuous films are obtained only at lower deposition temperatures (100^{o}C and 190^{o}C). At higher temperatures discrete droplets sparsely distributed on the substrate (290^{o}C) and powdery product (390^{o}C) were observed.

The most two interesting films (100^{o}C/350^{o}C and 190^{o}C) look hazy with naked eye. This is attributed either to the non-uniform packing of the droplets, to the presence of cracks and/or to the evolving of gaseous products from the surface of the films.

The infrared spectra of the USP-synthesized films showed that the films that were deposited at 190^{o}C are devoid of the surfactant and most part of the precursor is converted into tungsten oxide. At higher temperatures (post-treatment at 350^{o}C or deposition at 390^{o}C), tungsten oxide is the only component of the films.

Interestingly, TEM micrographs depicted that the films (except the ones deposited at 390^{o}C which were not studied) contain well distinct pores. Therefore, in this study it is proofed that templating is a strategy that can be successfully combined with the spraying process. It appears that the presence of the surfactant not only induces porosity in the films but it also improves the solution coating properties and its spreading on the substrate surface. SEM micrographs illustrated that in the absence of a surfactant, a continuous layer cannot be achieved with this precursor at any temperature but rather rough surfaces with shapeless features are observed.

The templated films (100^{o}C/350^{o}C and 190^{o}C) exhibit high reversibility (95 and 82% respectively), optical contrast (59 and 30%) and coloration efficiencies (40 and 16%). The films that were deposited at 190^{o}C present slightly better coloration compared to the films that were deposited at 100^{o}C (and then post-treated at 350^{o}C) but due to the lower initial transparency all the optical quantities are much lower. Moreover, the cyclic voltammograms revealed that the porous films are lacking long-term stability. This limitation is attributed to the porous and hydrated nature of the films.

Despite a number of drawbacks observed for the produced films (hazy appearance with cracks, short-term degradation), it has been proven that ultrasonic spray pyrolysis is a powerful tool especially when successfully combined with the templating method. Cost-effectiveness, fast and continuous production rates, without requiring vacuum conditions have established the ultrasonic spray pyrolysis as a large-scale production line method for transparent layers. In this study, we further proved that when surfactants are incorporated in the experimental process, the solution spreading quality is substantially improved and

continuous films at higher maximum deposition temperatures can emerge. The latter can also be beneficial for large-scale applications since the whole process is completed in one step and the post-thermal treatment may be avoided. Additionally, the successful induction of porosity through the templating process enhances the electrochromic performance and it ensues films with relatively high coloration efficiency, optical contrast and reversibility.

6.2 Perspectives

Throughout this study, we evidenced that porous materials present numerous privileges compared to their dense counterparts namely higher optical contrast, better reversibilities, higher coloration efficiencies, better solution coating properties in the presence of a surfactant etc. However, we believe that further studies should be realized in the future in order to optimize all the studied parameters and to further corroborate all the aforementioned statements. In the following lines, we are listing some suggestions that would be interesting for future research:

1) Based on our ellipsometric measurements, Brij-56 dip-coated films contain 23% of porosity which is a relatively low value. For example, percentages as high as 45 have been reported in P123/TiO_2 systems [1]. We believe that by further increasing the percentage of air, better electrochromic properties can emerge. This can be achieved for example by the use of bulkier surfactants (such as P123 and F127) with higher micellar volumes, by increasing the amount of surfactant (and presumably the density of pores inside the films) or by inducing hierarchical mesophases (bimodal pore size distribution) [2] while preserving the same amount of inorganic material. Some preliminary trials have been conducted to produce porous films with the use of F127 rather than Brij-56, however porosity collapsed due to insufficient control over the thermal treatment. Therefore, further studies should take place in order to design a more careful annealing profile for the elimination of F127 and the preservation of porosity.

2) It was reported that porous nanocrystalline tungsten oxide films with high surface area could also enhance the electrochromic performance [3]. One way to produce mesoporous tungsten oxide nanocrystallites with limited size is to use surfactants with higher decomposition temperatures such as poly(isobutylene)-block-poly(ethylene oxide) [4]. In that way, the surfactant ideally remains intact at high temperatures where crystallization occurs. At the same time the nanocrystallites growth is confined into the thin walls of the mesostructure.

3) In ultrasonic spray pyrolysis process the hazy appearance of the emerging films, significantly constrain their electrochromic performance. Therefore a need arises to produce porous films of high optical quality with this technique. In the work of J. Denayer et al. [5] USP tungsten oxide films with a PEG (polyethylene glycol) surfactant-assisted method was employed. This method produced non-porous films with remarkable electrochromic performance and a very low initial diffuse transmittance (1.8%) owing to the presence of PEG. Therefore, we suggest a study of Brij-56/PEG mixed solutions which

might generate porous films with good optical quality and improved electrochromic performances.

4) In this thesis, we proved based on electrochemical measurements in ambient and inert atmosphere that the presence of ambient humidity modifies the experimental outcome. We suggested that protons are intercalating along with the lithium cations inside the material. However, we didn't specify the exact intercalating species. For example, in the recent study of F. Razzaghi et al. [6], species such as Li^+, $Li^+.H_2O$, H_2O and ClO_4^- were found to intercalate in the material. Their work was based on the coupled time resolved characterization methods (fast QCM/electrochemical impedance spectroscopy). Therefore, a similar study on our films would be interesting to determine how and which intercalating species are participating in the electrochemical process.

5) In this dissertation, the electrochromic characterization was conducted ex-situ in order to color/bleach the films under inert conditions (Ar-filled glovebox) to avoid any contact with the ambient humidity. However, it would be interesting to investigate the dynamic transmittance while switching the applied potential. For this reason, in some publications (e.g. in reference [7]) a diode laser in conjunction with a light detector inserted in a glovebox have been used.

6) Finally, a thorough study and determination of the parameters which influence the USP process, such as the droplets size, the surface tension and their dependence on the proportion and the nature of the surfactant would be valuable in order to have a more elucidated view on the spraying process.

6.3 References for Chapter 6

[1] J. Dewalque, Templated TiO2 mesoporous films used as highly efficient photoelectrode in Dye-Sensitized Solar Cells, chapter 4, PhD dissertation, (2013).

[2] P. Innocenzi, L. Malfatti, G.J.A.A. Soler-Illia, Hierarchical Mesoporous Films: From Self-Assembly to Porosity with Different Length Scales, Chemistry of Materials, 23 (2011) 2501-2509.

[3] J. Kim, G.K. Ong, Y. Wang, G. LeBlanc, T.E. Williams, T.M. Mattox, B.A. Helms, D.J. Milliron, Nanocomposite Architecture for Rapid, Spectrally-Selective Electrochromic Modulation of Solar Transmittance, Nano letters, 15 (2015) 5574-5579.

[4] C. Henrist, C. Toussaint, J. de Vroede, D. Chatzikyriakou, J. Dewalque, P. Colson, A. Maho, R. Cloots, Surfactant-assisted ultrasonic spray pyrolysis of hematite mesoporous thin films, Microporous and Mesoporous Materials, 221 (2016) 182-186.

[5] J. Denayer, P. Aubry, G. Bister, G. Spronck, P. Colson, B. Vertruyen, V. Lardot, F. Cambier, C. Henrist, R. Cloots, Improved coloration contrast and electrochromic efficiency of tungsten oxide films thanks to a surfactant-assisted ultrasonic spray pyrolysis process, Solar Energy Materials and Solar Cells, 130 (2014) 623-628.

[6] F. Razzaghi, C. Debiemme-Chouvy, F. Pillier, H. Perrot, O. Sel, Ion intercalation dynamics of electrosynthesized mesoporous WO3 thin films studied by multi-scale coupled electrogravimetric methods, Physical Chemistry Chemical Physics, 17 (2015) 14773-14787.

[7] C.-P. Li, C.A. Wolden, A.C. Dillon, R.C. Tenent, Electrochromic films produced by ultrasonic spray deposition of tungsten oxide nanoparticles, Solar Energy Materials and Solar Cells, (2011).